

QUANTUM EFFECTS IN BIOLOGICAL SYSTEMS

LEE KAI SHENG

SCHOOL OF PHYSICAL AND MATHEMATICAL SCIENCES

QUANTUM EFFECTS IN BIOLOGICAL SYSTEMS

LEE KAI SHENG

SCHOOL OF PHYSICAL AND MATHEMATICAL SCIENCES

A thesis submitted to the Nanyang Technological University in partial fulfilment of the requirement for the degree of Doctor of Philosophy

Statement of Originality

I hereby certify that the work embodied in this thesis is the result of original research done by me except where otherwise stated in this thesis. The thesis work has not been submitted for a degree or professional qualification to any other university or institution. I declare that this thesis is written by myself and is free of plagiarism and of sufficient grammatical clarity to be examined. I confirm that the investigations were conducted in accord with the ethics policies and integrity standards of Nanyang Technological University and that the research data are presented honestly and without prejudice.

TU NTU I

U NTU NTI

...5/9/2022

Date

......LEE KAI SHENG
[Input Name Here]

^{*}please sign on the water mark area.

Supervisor Declaration Statement

I have reviewed the content and presentation style of this thesis and declare it of sufficient grammatical clarity to be examined. To the best of my knowledge, the thesis is free of plagiarism and the research and writing are those of the candidate's except as acknowledged in the Author Attribution Statement. I confirm that the investigations were conducted in accord with the ethics policies and integrity standards of Nanyang Technological University and that the research data are presented honestly and without prejudice.

.....5/9/2022...... Date

TU NTU NTU NTU NTU NTU NTI

TU NONTUNTUNTUNTUNTUNTUNTUNTUNTU

.......RAINER DUMKE.......
[Input Supervisor Name Here]

*please sign on the water mark area.

Authorship Attribution Statement

Please select one of the following; *delete as appropriate:

*(A) This thesis **does not** contain any materials from papers published in peer reviewed journals or from papers accepted at conferences in which I am listed as an author.

*(B) This thesis contains material from2 paper(s) published in the following peerreviewed journal(s) / from papers accepted at conferences in which I am listed as an author.

Chapter 4 is published as Lee, K.S., Dumke, R. & Paterek, T. Numerical tests of magnetoreception models assisted with behavioral experiments on American cockroaches. *Sci Rep* **11**, 12221 (2021). DOI: 10.1038/s41598-021-91815-x

The contributions of the co-authors are as follows:

- Prof. Paterek and Prof. Dumke provided the initial project direction and helped in revisions in the manuscript drafts.
- I prepared the manuscript drafts and performed the laboratory experiments, simulations and analysis.

Chapter 7 from the pre-print Lee, K. S. et al. Entanglement between superconducting qubits and a tardigrade. *arXiv*:2112.07978v2 (2021)

The contributions of the co-authors are as follows:

- Prof. Møbjerg provided the tardigrades and methodology in the handling of the animals, as well as editing of the manuscript drafts.
- Prof. Vedral, Prof. Paterek and Prof. Dumke helped in discussions and formulation of the models used, as well as revisions to the manuscript.
- I handled the animals, prepared the manuscript drafts and performed the calculations, simulations and analysis of the data.

- Dr. Hufnagel, Dr. Yap, Dr. Budoyo, Mr. Nguyen performed the operations necessary to maintain the qubits and fridge functional.
- Mr. Tan and Mr. Park controlled the interface to the fridge in order to perform the qubit gates and readouts.

TU NTU I

NTU NTU

TU NTU I

... 5/9/2022...... DateLEE KAI SHENG ...
[Input Name Here]

^{*}please sign on the water mark area.

Abstract

Quantum mechanics is at its hearts the study of nature at the fundamental level of atoms and subatomic particles. Made up of these same atoms and subatomic particles, biological systems are also expected to follow quantum mechanics to some extent. Given the quantum mechanical origin of the interaction between magnetism and matter, magnetic field effects within biological systems are natural candidates for the search of bio-relevant quantum processes.

In this thesis, we explore theoretically and experimentally magnetic and electric fields acting on biological systems of varying complexity. We begin with attempts to use Pulsed-ElectroMagnetic Fields (PEMFs) on cells and simple organisms. In particular, mitochondrial activity, cell proliferation and calcium entry are measured and show no clear correlation with used PEMFs. In a separate experiment, we demonstrate a magnetic sensitivity in *Periplaneta americana*, the American cockroach, and using numerical methods, show that this sense is most likely based on the radical pair mechanism. Finally, we describe yet another experiment that shows entanglement in a qubit-qubit-tardigrade system, with the tardigrade still alive by the end of the experiment. This is one of the most direct demonstrations of interfacing quantum and biological systems to date, and is a proof-of-concept for future experiments to use the tardigrade as a model organism in probing the limits of the quantum to classical transitions.

Acknowledgements

I would like to very gratefully thank my supervisors A/Prof. Rainer Dumke and A/Prof. Tomasz Paterek for all their guidance, support and input over the years. I truly appreciate the constructive discussions over the many projects throughout my PhD programme.

I thank A/Prof. Alfredo Obregon for welcoming me to work with his team in the BICEPS lab at NUS, as well as the amazing team members themselves Dr. Tai, Dr. Soong, Jasmine Yap, Charmaine Ng, Jocelyn Yin, Craig Wong, Joyce Foo who have guided me in the biological lab work that was completely new to me.

I thank Prof. Vlatko Vedral for the discussions and ideas to improve and strengthen the theoretical models used in our papers, and Prof Nadja Mobjerg for the supply of indestructible tardigrades and help in methodology for keeping them healthy.

I wish to express gratitude for Prof. Laskowski for hospitality at the University of Gdansk.

I thank the wonderful colleagues and friends Dr. Miller, Dr. Lake, Dr. Zhao, Ray Ganardi, Liu Zheng, Lamia Varawala, Ankit Kumar in my previous research group who have graced me with their lovely company over the few years on this journey. Special thanks to Ray for being an amiable flat mate.

I thank even more colleagues and friends Dr. Hufnagel, Dr. Oon, Dr. Budoyo, Dr. Gan, Dr. Yap, Paul Tan, Kun Hee, Long, for accepting me into my current research group and offering much needed guidance into the world of experimental physics.

Finally, I wish to thank my brother, my mother and my father for supporting me over the years. Additionally, special thanks to a special someone who has been constantly making my days ever so slightly better, and ultimate partner in crime, Zeann.

Contents

1	Intr	roduct	ion	1
	1.1	Magnetic field interactions with biological systems		
		1.1.1	Magnetoreception	2
		1.1.2	Other effects	3
	1.2	Direct	observation of quantum effects in biological systems	3
	1.3	Struct	cure of Thesis	3
I	NД	agnot	ic Field Effects in Cells	4
1	1 V1	agnet	ic Field Effects in Cens	4
2	Effe	ects of	Pulsed Electro-Magnetic Fields	5
	2.1	Pulsed	d Electro-Magnetic Fields	5
		2.1.1	Physical realisation of PEMF signals	6
		2.1.2	PEMF test conditions	8
	2.2	Caeno	orhabditis elegans	10
		2.2.1	Worm Culture	10
		2.2.2	Treatment	11
		2.2.3	MitoSOX Dye	11
		2.2.4	Results	11
		2.2.5	Discussion	14
	2.3	Cell P	Proliferation experiments	14
		2.3.1	C2C12 mouse myoblast cell line	15
		2.3.2	Manual cell count	17
		2.3.3	Fluorescence spectroscopy	18

		2.3.4	Light/Dark Experiments	20
	2.4	C2C12	2 cell-derived vesicles	20
		2.4.1	Experiment overview	21
		2.4.2	Preparation of Calcium Green-loaded CDVs	22
		2.4.3	SEM imaging of CDVs	22
		2.4.4	Magnetic field effects on calcium entry	22
	2.5	Concl	usion	26
II	N	Iagne	toreception	28
3	Mos	st Con	nmon Models of Magnetoreception	29
	3.1	Ferror	nagnetic-based models	30
		3.1.1	Size considerations	30
	3.2	Radic	al Pair model	34
		3.2.1	Toy Model	35
	3.3	Chara	cteristics of magnetoreception	38
	3.4	Summ	ary	38
4	Beh	aviora	d Experiments on Periplaneta americana	39
	4.1	Peripl	laneta Americana	39
		4.1.1	Habitat	40
		4.1.2	Magnetic field conditions	40
		4.1.3	Experimental Procedures	42
	4.2	Result	Ss	42
		4.2.1	Discussion	42
		4.2.2	Ferromagnetic-based models	45
		4.2.3	Fitting to the Radical pair models	49
		4.2.4	Summary	55

II	Ι Ι	Entan	glement in Living Systems	58		
5	Qua	antum	Harmonic Oscillators	59		
	5.1	Theor	etical Background	59		
		5.1.1	Spin	59		
		5.1.2	Quantum systems	59		
		5.1.3	Multi-particle systems	60		
		5.1.4	Quantum Harmonic Oscillator	60		
		5.1.5	Fock states	61		
		5.1.6	Zero-point Energy	62		
6	Cav	Cavity Quantum Electrodynamics				
	6.1	Rabi 1	model	63		
		6.1.1	Jaynes-Cummings Model	67		
		6.1.2	Dicke Model	68		
		6.1.3	Tavis-Cummings model	68		
	6.2	Summ	nary	70		
7	Entanglement in a qubit-qubit-tardigrade system					
	7.1	Trans	mon Qubit	71		
	7.2	Tardig	grades	73		
	7.3	Experimental Overview				
	7.4	Freque	ency Readout Experiment	74		
		7.4.1	Dielectric shift	76		
		7.4.2	Transmon qubit subspace	76		
		7.4.3	Tardigrade as a collection of harmonic oscillators	78		
		7.4.4	Qubit-Tardigrade system	78		
	7.5	Prepa	ration of Bell state	81		
		7.5.1	Entanglement quantifiers	82		
	7.6	Bysta	nder model	84		
		7.6.1	Electric field coupling	86		

CONTENTS

	7.7	Revival	86
	7.8	Summary	88
8	Con	nclusions and Outlook	89
	8.1	I: Magnetic Field Effects in Cells	89
	8.2	II: Magnetoreception	90
	8.3	III: Entanglement in Living Systems	90
	8.4	Outlook	91
Α	Indi	ividual cockroach activity time	93

Chapter 1

Introduction

3 1.1 Magnetic field interactions with biological systems

- 4 The Earth's magnetic field has existed for at least 3.5 billion years, the result of an electrically conducting
- fluid core [1]. Most of life has evolved in the presence of the Earth's field and it is unsurprising that organisms
- 6 have developed adaptations taking advantage of it. On the timescales of human civilisation, the prevalence
- of magnetic fields (beyond the Earth's geomagnetic field) is a relatively modern phenomenon stemming from
- the commercialisation of electricity. Due to the limitation on manipulation of magnetic fields, not much is
- 9 known on the effects of magnetic fields on animals or humans.

Based on the laws of electromagnetism, there are two ways for systems to interact with magnetic fields. The first and most straightforward way is by having a magnetic moment that can directly interact with 11 magnetic fields, much like the needle in a compass. Classically, such a magnetic moment is only present in permanent magnets like ferromagnetic or ferrimagnetic materials such as magnetite (Fe₃O₄), which though 13 discovered in several species of animals, are not often present in most biological systems. The second way is through Maxwell's laws, where varying magnetic fields can induce electromotive forces, or static magnetic 15 fields can deflect ionic currents even in non-magnetic materials. However, this mode of interaction tends to be quite rare. The notion of cellular transmembrane potentials has been well-established and studied, 17 regulating processes from the cell-cycle to even muscle contractions [2]. The issue arises from the fact that the small surface areas of cells would necessitate static magnetic fields as large as 10^{-4} T or gradients of 19 10⁹ T/m to produce any appreciable effect [3]. One of the few animals observed to use inductive effects are elasmobranchs like sharks and rays, requiring the use of large and highly specialised organs, the ampullae of Lorenzini connected to long canals filled with highly conductive collagen jelly, to detect magnetic fields [4]. By swimming through the geomagnetic field, the electromotive forces induced across the canals are detected 23 by the highly sensitive ampullae.

One should then not expect any magnetic field interactions in systems with the absence of magnetite or highly specialised organs like the ampullae of Lorenzini. However, a different form of interaction has been proposed to exist [5] that is quantum in nature. This is the radical pair mechanism that couples a spin-dependent chemical reaction dynamic to a magnetic field. The radical pair mechanism, from its namesake, involves a coherent generation of a pair of radicals by the cleaving of a covalent bond from a larger molecule. In the simplest scenario, the radical pair system can be reduced to a singlet-triplet system from the electron pair of the cleaved bond. Distinct sequences of chemical reactions then proceed depending on whether the electron pair is in the singlet or triplet state, eventually culminating in a perceivable difference in chemical yield that can be transduced into a signal as the basis for a magnetic sense. An external magnetic field can then play a role in modulating the chemical yields by altering the population dynamics of the singlet-triplet system. Quantum coherence is necessary for the electron pair to remain in this singlet-triplet subspace and

- have also been observed to play a role in photosynthesis [6–8]. Arguably, the nature of the radical pair mechanism, being a magnetically sensitive chemical reaction, suggests that magnetic fields can play a larger role in biological processes than previously assumed.
- 39 We now introduce some important utilisations of magnetic fields in living systems.

40 1.1.1 Magnetoreception

One of the more ubiquitous utilisations of the geomagnetic field is for directional and navigational purposes. 41 For instance, magnetotactic bacteria are observed to passively align with magnetic field lines, a phenomena 42 coined as magnetotaxis [9]. This is achieved via chains of magnetic crystals encased in membranes rigidly 43 connected to the bacteria so that the magnetic torque can directly steer the whole organism. For larger 44 animals, an added layer of complexity in translating the magnetic torque to biologically useful neuronal signals is required. A plethora of species across the animal phyla, from insects like planthoppers [10] to 46 honeybees [11–13], fish like yellowfin tuna [14] and sockeye salmon [15], mammals like bats [16, 17] and 47 migratory birds like homing pigeons [18], have been observed to exhibit the ability of magnetoreception. 48 A fuller compilation of known species can be found in [19]. A major significance of magnetic sensing in animals is the ability to perceive the relatively weak Earth field of approximately 0.05 mT. Interestingly, 50 the European robin's magnetic sense is sensitive to static fields as low as 4 μ T [20]. This is remarkably 51 small, translating to a 4.6×10^{-28} J Zeeman shift in Earth field, and 7 orders of magnitude smaller than 52 room temperature thermal energy, k_BT of 3.77×10^{-21} J. Additionally, sensitivity to time-varying fields 53 with amplitudes in the range 1-10 nT were also displayed in European robins [21], garden warblers [22] 54 and American cockroaches [23]. Current high-sensitivity magnetic sensors like Superconducting QUantum 55 Interference Devices (SQUID) and Spin Exchange Relaxation Free (SERF) devices are restricted by their bulky design, required by heavy refrigeration, or in the latter case, operate only at near-zero fields. Biological 57 sensors, however, appear to operate at room temperature and are essentially limited by organism size (and most likely head or eyes), presenting highly compact systems depending on species, which once understood 59 would lead to robust man-made sensors.

With regards to avian magnetoreception, three interesting characteristics have been observed across several studies over different species and different magnetic conditions [24]. The first is that homing pigeons [25], 62 and several migrant species [26] have been found to utilise an inclination compass, which is expected to 63 be a general trait of avian magnetoreception [27]. The second characteristic is the presence of a functional 64 window, together with some room for adaptability. If the local magnetic field drifts too far from what the 65 bird is normally accustomed to, around the value of 47 μ T typical of the Earth's field, they can become disoriented. However, housing them in new fields over a duration was observed to allow the birds to adapt 67 to the new fields [20, 28]. Lastly, the third characteristic is the light dependency of the avian magnetic compass. Several experiments under narrow band light showed disorientation (see [24] for fuller compilation 69 of wavelengths). 70

Arguably, the third characteristic - light dependency, is somewhat the smoking gun for the radical pair 71 mechanism, with photo-excitation being a necessary step to initiate the entire process. It is not immediately 72 clear how light dependency could play a role in ferromagnetic or induction based models. Many animals 73 display quirks in their magnetic compasses when exposed to light of different wavelengths. Domestic chickens 74 (Gallus gallus) showed magnetic orientation behaviour under blue light (465 nm), but not red (645 nm) [29]. 75 European robins would orientate when exposed to narrowband 560.6 nm light, became completely disoriented under 567.5 nm and oriented themselves in a different direction under 617 nm [30]. Iberian green frog 77 (Pelophylax perezi) tadpoles also show a 90° shift in orientation direction when exposed to long wavelengths (> 500 nm), as compared to white light [31]. These light dependent characteristics of magnetic compasses 79 most likely utilise organs based on the radical pair process and therefore would be manifestations of quantum effects in biological systems.

82 1.1.2 Other effects

100

101

102

103

104

106

107

108

110

111

112

Beyond magnetoreception, more recent scientific discourse has been focused on magnetic effects on the cellular level. To date, some of the observed in-vitro effects of magnetic field exposure include influencing 84 the formation of cartillage [32], slowing growths of certain human cancer cells [33], and morphological changes in human neuronal cells [22]. More detailed compilations on biological effects on cells can be found in [34,35] for static magnetic fields, spatially variant magnetic fields [3], and pulsed electro-magnetic fields (PEMFs) 87 Given that biological matter has magnetic permeability similar to water, and presents almost no screening effects, magnetic therapy potentially presents a highly penetrative yet non-invasive procedures. 89 The underlying mechanisms by which such magnetic fields can influence cellular activity are still poorly understood and debated, though notable explanations suggest that magnetic fields regulate Reactive Oxygen 91 Species (ROS) levels, interestingly also involving the radical pair mechanism [37], again hinting at the quantum nature of this interaction, or calcium entry via unspecified action on Transient Receptor Potential 93 Canonical-1 (TRPC1) channels [38].

Ultimately, the large number of seemingly unrelated effects linked to magnetic fields suggest some, as of yet unknown, fundamental biological processes or that magnetic fields are far more involved in biology than previously thought. To harness the therapeutic potential or mitigate health risks associated with magnetic fields, it is important to understand and model the physical processes behind the observed effects.

₉₉ 1.2 Direct observation of quantum effects in biological systems

Perhaps the most direct way to observe quantum effects in biological systems is to perform experiments to directly blend the two fields. This, however, is beset with an irreconcilable incompatibility between biological and quantum experiments tend to be performed in, "hot and wet" and "cold and controlled" respectively. For example, proximity to food, water or air is pivotal to complex life, yet extremely detrimental to quantum coherence with more channels for decoherence. Conversely, fairly low temperatures are required in order for thermal noise to be less prominent. Typically, these translates to about 2 mK in dilution refrigerators, far colder than the 300 K that most complex life thrives in. Remarkably, there exists an organism - the tardigrade, that can survive in both the extreme conditions outlined by transitioning into a reversible ametabolic "tun" state. In the thesis, we will describe an experiment that exploits the resilience of the tardigrade to perform quantum experiments with the tardigrade subsystem. The tardigrade was then even observed to return to its active state after the entirety of the experiment. This can be seen as a proof of concept for future experiments to utilise tardigrades as model organisms in investigating the interface between the quantum and biological fields.

1.3 Structure of Thesis

In the present thesis, we divide our discussions into three main parts (I-III), based on the chronological 114 order of the projects, beginning with "I - Magnetic field effects in cells", a broad spectrum of experiments 115 looking into in-vitro biomagnetic effects on cell and worm cultures. These experiments attempt to explore the 116 emerging field of PEMF therapy, where exposures to specific magnetic fields have been reported to produce 117 a wide range of potentially beneficial effects on cell growth and recovery, particularly in cartilage [32, 39-44] 118 and bone recovery [45-47]. In "II - Magnetoreception", we look into the phenomenon of magnetoreception 119 and its most probable underlying mechanisms of ferromagnetic or radical pair based senses. This is followed up by a behavioural study on the magnetic sensitivity of American cockroaches. Finally, in "III - Entangling 121 Living Systems", we discuss what is arguably the closest attempt to date at melding biological with quantum systems by entangling a tardigrade mode within a microscopic animal, with superconducting qubits.

Part I

125

Magnetic Field Effects in Cells

In the recent decade, a wide variety of magnetic effects are observed in many
biological systems, but no clear mechanism has been found to explain them. In
this chapter, we describe experiments looking for clear signs of magnetic effects
in various biological systems. Although we were ultimately unable to obtain
any distinct signals, the documentation here will still be worthwhile for future
investigations to understand the phenomena.

\mathbf{c}_{12} Chapter 2

Effects of Pulsed Electro-Magnetic Fields

The impact of electric field stimuli in biological processes has been long studied and well accepted. This is especially true for the physiology of living creatures where the main interface between cells involves neurons and electrical impulses. Up till recently, magnetic fields could be largely ignored due to the scarcity of magnetic sources beyond the ambient geomagnetic field. This has changed in the current digital age where daily appliances like cellphones emit constant barrages of electromagnetic waves. What makes it especially concerning is that unlike electric fields, magnetic fields are not as easy to shield from.

Recent studies have started to reveal a seemingly wide variety of magnetic field effects like wound healing [48, 49] and even pain relief [50, 51]. At the same time, extremely low-frequency magnetic fields (50-60 Hz) have been classified by the International Agency for Research on Cancer (IARC) as possibly carcinogenic [52] based on their own epidemiological studies. In order to safely utilise magnetic fields as therapeutic alternatives and minimise potential risks, it is important to understand the mechanism by which they can impact biological tissue. In this chapter, we present experiments to look for clear signals of magnetic effects on biological systems so as to eventually develop a physical model to explain them.

In collaboration with the BICEPS group at iHealthtech NUS, experiments investigating the effects of Pulsed Electro-Magnetic Fields (PEMFs) on biological systems were conducted. Preliminary investigations hinted at therapeutic applications of PEMFs, with the studies eventually concluding effects on myogenesis (skeletal muscular tissue formation) [38, 53] and chondrogenesis (bone cartillage formation) [32, 44].

From a physical perspective, it is not immediately clear how biological systems, that are comprised of mostly water, can interact with magnetic fields. However, using the radical pair mechanism as an example, it is certainly possible to envision that magnetic fields do have an impact on living matter. In this chapter, we make an attempt at understanding how magnetic fields can influence biological processes by studying 3 different biological systems. These are, in decreasing complexity, (i) Caenorhabditis elegans, (ii) C2C12 mouse myoblast cells, and (iii) C2C12-derived cellular vesicles.

2.1 Pulsed Electro-Magnetic Fields

Historically, it is not known when the use of magnetic fields as a treatment first began. More modern series of studies date back to 1974 when magnetic fields were shown to accelerate fracture repair [45–47]. More recently, dating around the 2000s, studies on magnetotherapy have begun splintering into various subgroups

of the type of fields utilised such as static fields, PEMFs which usually refer to low-frequency fields, and higher frequency fields above the radiofrequency ranges [54]. Virtually all of these magnetic fields are realised in laboratories using variations of a Helmholtz coil, in which the magnetic field generated along the coil axis x is governed by the equation

$$B(x) = \frac{\mu_0 n I R^2}{2(R^2 + x^2)^{\frac{3}{2}}},$$
(2.1)

for a coil with n turns, radius R, and a current I flowing through it. The magnetic field generated by a coil scales linearly with the amount of current delivered to it. Here, μ_0 is the permeability of free space and the coil axis is defined with the center as the origin. As such, coils with time-varying fields experience much lower heating effects due to a lower average current as compared to a coil driven by static current with similar peak value.

The specific profile utilised by BICEPS is presented in Fig. 2.1. It consists of packets repeated at 15 Hz, with each packet consisting of digital signals alternating between a variable peak value (set to 1.5 mT unless otherwise stated) and 0 (field off). There are 20 alternations per packet. Previous experiments (some conducted in parallel with the experiments described here) using this profile have shown various effects like (i) promotion of chondrogenesis (cartilage formation) [32,44], (ii) myogenesis (skeletal muscular tissue formation) [38,53], as well as (iii) impairing cancer cell growth [55].

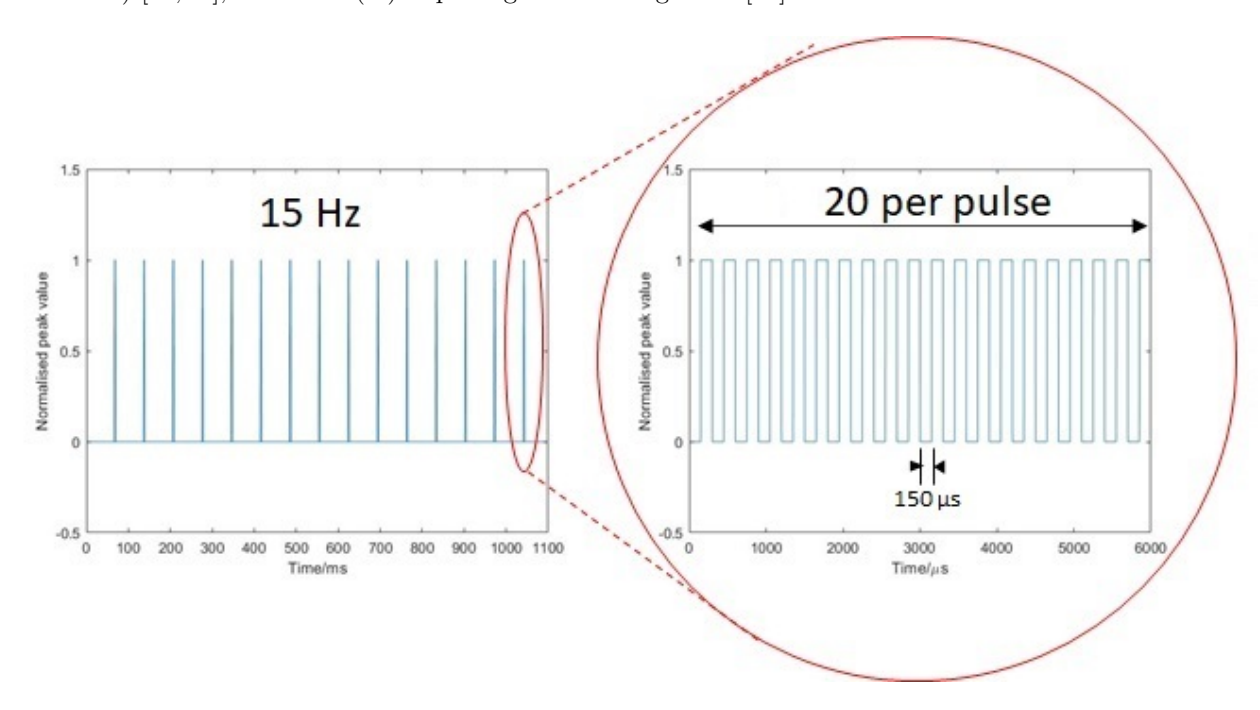


Fig. 2.1: Signal profile of PEMF used in the experiments examining its effects on biological systems. The signal consists of packets at 15 Hz, with each packet consisting of digital signals switching between "on" and "off" every 150 μ s.

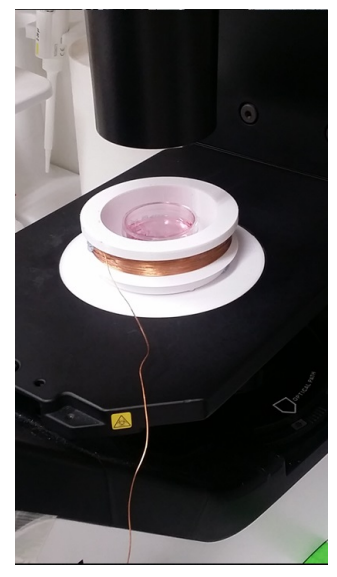
2.1.1 Physical realisation of PEMF signals

The PEMF signals were generated by modulating current through coils. We investigated three magnetic coil systems: a microscope mountable coil system (coil A), a prototype Mregen coil system for treatment (coil B) and a μ -metal shielded coil system (coil C), see Fig. 2.2 for photos of the systems. Coils B and C were the original devices used by the BICEPS group, while Coil A has been designed and built to accommodate different experimental variations. Before moving to the new design, let me briefly review the coils used

183 previously.

Coil B is a prototype "Mregen" coil system that allowed for an appendage to be placed in the cavity for clinical trials. Since it was designed for clinical trials, there was limited maneuverability in terms of experimental parameters. A circular coil was housed in a casing that prevented tampering, and the electronics system used to power the device could only be accessed by a single button that would switch on the coil for 10 minutes, producing the PEMF signal at a peak value of 1.5 mT.

Coil C is housed within a rectangular mu-metal case, effectively shielding the inside from all external magnetic fields. Unlike coil B, this coil system allowed for some customisability of the PEMF signal, with programmable peak field values (in steps of 0.5 mT), and exposure duration. However, the overall signal profile and frequencies were still fixed.



(a) Coil A, miniaturised microscope mountable coil.



(b) Coil B, prototype Mregen coil system; cavity large enough to rest appendage during PEMF exposure treatment.



(c) Coil C, μ -metal shielded coil system (cover removed).

Fig. 2.2: The three different coil systems used for application of PEMF treatments. All produce the same functional pulse sequence. Only coil C has a full mu-metal shielding.

Coil A Design

193

195

197

198

199

200

201

To facilitate investigations into the mechanistic nature of the PEMFs on biological systems, a separate coil system was designed, see Fig. 2.3. This served a few purposes. Firstly, to verify that the observed effects were from the PEMF fields alone, a separate device producing the exact signal should also produce the same experimental outcomes. Secondly, there were certain limitations in the coil systems B and C, like the bulk, size and fixed signals, that limited experimental designs. To circumvent the limitations, a smaller coil system with a fully customisable signal profile, was designed. This coil A was mountable onto a microscope, with the coils driven by an arbitrary function generator (Rigol DG 1022) connected to an amplifier (scandyna 300 watt SA-77011-USB).

A few advantages were afforded by the coil A system. Firstly, in terms of the PEMF signal, the function generator allows for arbitrary frequencies and waveforms to be applied. In turn, the smaller coil size (less number of turns and smaller surface area) possesses a lower inductance than the other two larger coils,

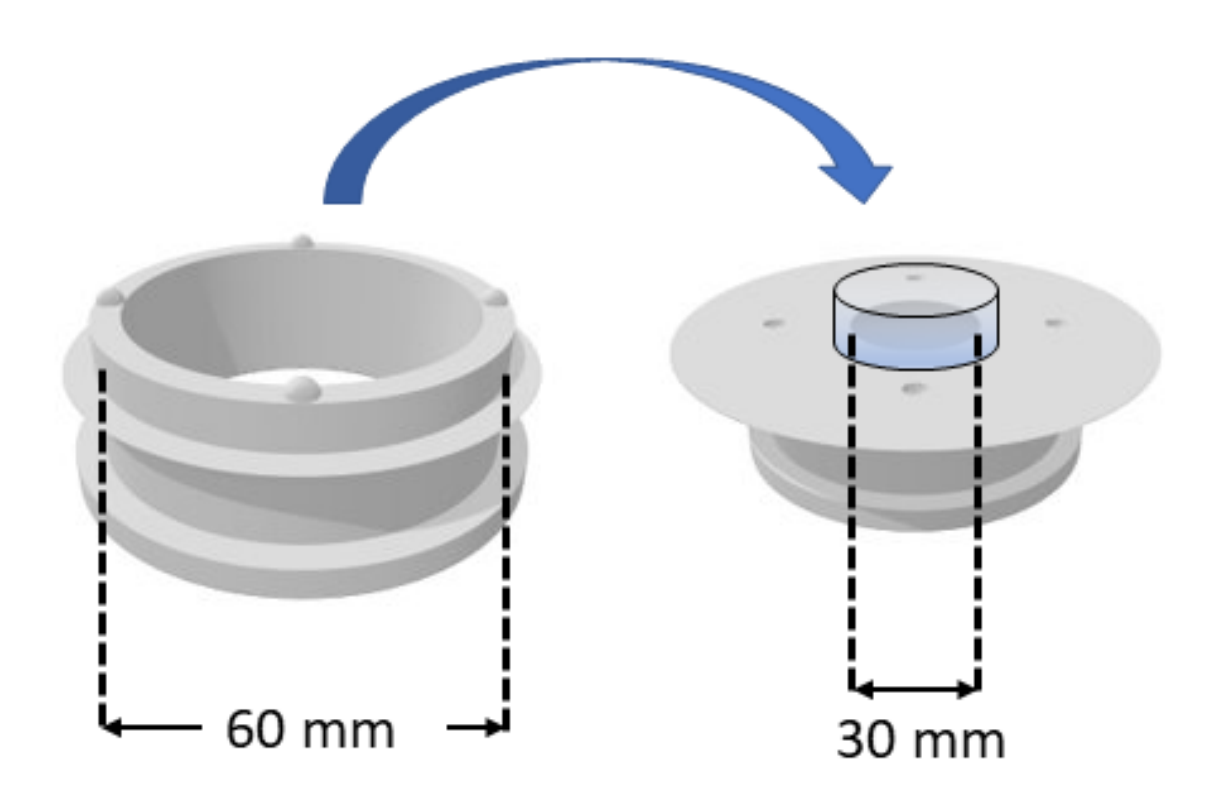


Fig. 2.3: Coil A mount design: detachable Helmholtz coil mount of diameter 60 mm. The top piece (left) fits into the base and is secured into the hemispherical grooves in the base piece (right). A flat stage with a 30 mm diameter hole is present in the center of the assembled coil to house samples. The hole allows for illumination from the underside.

reducing the need for powerful amplifiers. Inductance acts against changes in electric currents and manifests as distortions of the switching signal. A physical realisation of a single packet produced by the top half of coil A is shown in Fig. 2.4. As seen, due to coil inductance and limitations of amplifiers, the real signal does not have as sharp rise as intended, nor a flat peak, but resembles the ideal signal closely. Additionally, its smaller size also allows for the coil (see Fig. 2.2a) to be directly mountable onto a microscope, allowing for live-imaging.

2.1.2 PEMF test conditions

206

207

208

210

Even with a fixed PEMF signal, the number of experimental variations that can be performed is still quite large. In our investigations, the PEMF exposure duration was chosen to be ten minutes. This is motivated both by preliminary observations and practical limitations. Preliminary studies suggested that a ten minute exposure was optimal for mitosis, which is part of the cell cycle involving replication of chromosomes into separate nuclei, with increased exposure being detrimental. More importantly, extended durations meant that the heating effect from prolonged operation of the coils was more prevalent and could potentially confound experimental observations.

The polarity of the PEMF signal (not passing 0 mT) allows for the directionality of the signal to be another

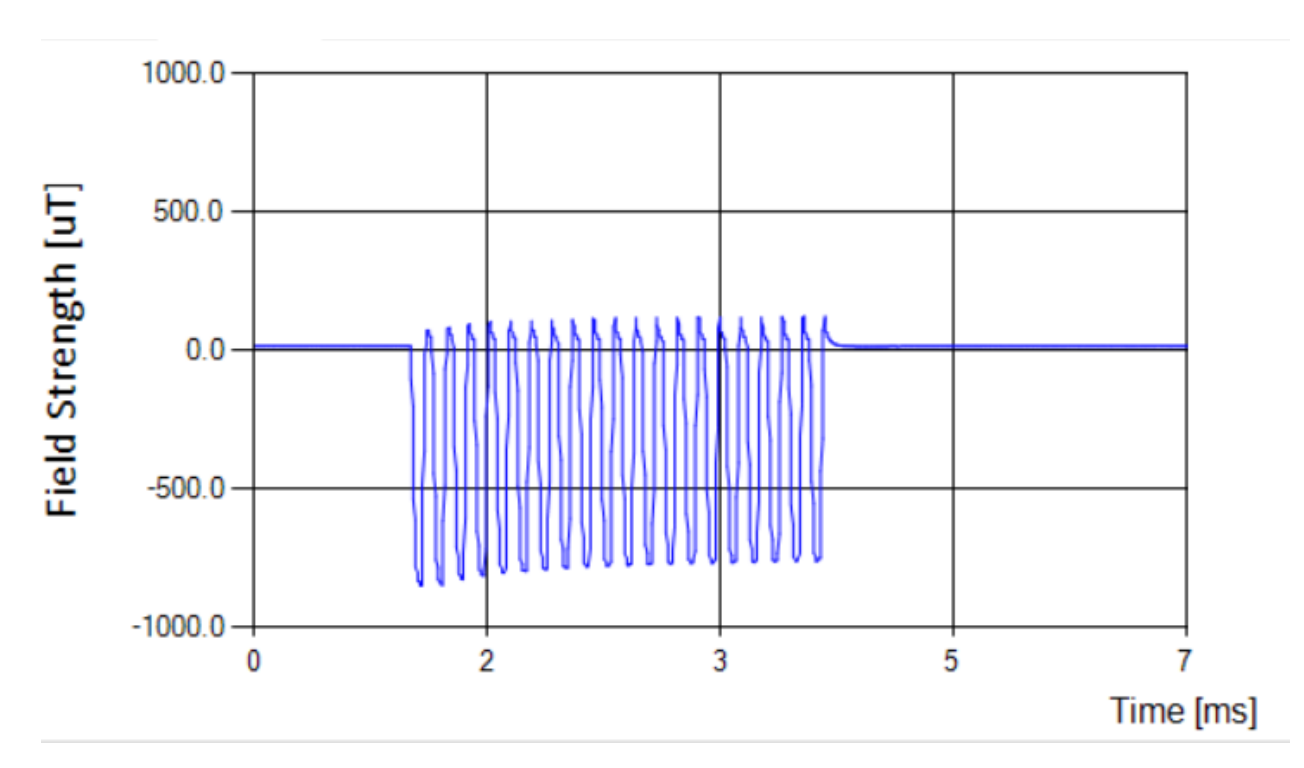


Fig. 2.4: Single packet of 20 square pulses produced by the top half of coil A. The signal is distorted to triangular waves due to the inductance and limitations of the amplifier. Yet, overall it closely follows the ideal signal.

parameter to be considered. We define the "down" directionality of the field to be the signals with negative peak values (aligned with gravity) and "up" for positive peaks (against gravity).

Another parameter is the field peak value. In distinction to coil C, the other two coil systems were not magnetically shielded. Thus, a large field intensity was preferred in order for the ambient geomagnetic field $(B_0 \gg 0.05 \text{ mT})$ to be negligible. A value of 1.5 mT was chosen to match the same fields used in the other ongoing experiments in parallel.

Due to the bulk of coil C, its directionality is fixed (down) while coils A and B can be altered. The field intensities were fully tunable in coil A, fixed at 1.5 mT in coil B and tunable in steps of 0.5 mT in coil C. Given the limitations of the various devices, a few permutations of experimental conditions were available for testing. It was decided to fix the PEMF signal to a peak value of 1.5 mT over 10 minutes across all devices. This was chosen as it was attainable across all devices and allowed comparisons to be made. Permutations of the directionality were occasionally performed subject to the availability of target biological system during the experiments, which tended to fluctuate over different batches of growth.

The biological systems that we will be investigating are, in order of complexity, the C. elegans worm, mouse muscle C2C12 myoblast cells and the subsequent extracellular vesicles derived from them. The chronological order of the experiments also proceeded as such, as unlike the biological complexity that reduces with the smaller systems, the experimental complexity inversely increases with system size. Briefly, we introduce these systems here, with more in-depth descriptions in the further sections. The C. elegans worm is a multicellular worm that is a model organism due to how well-understood it is, as well as sharing stark similarities with the human genome. A study on protein sequences in C. elegans showed that 83% of their proteins share common ancestry with humans [56]. The C2C12 mouse myoblast cells are an immortalised cell-line of mouse muscle cells. These are juxtapositions of human muscle cells before more rigorous in-vivo animal or human testing. Lastly, we have extracellular vesicles, a relatively new addition to the field of cellular biology. These are essentially fragments of the parent cells that they are derived from. They are not biologically 'active'

244 and can be thought off as snapshots of the cells during the creation process.

5 2.2 Caenorhabditis elegans

The first biological system investigated were Caenorhabditis elegans, shortened C. elegans or roundworms, 246 which are transparent nematodes, approximately 1 mm in length (see Fig. 2.5). They have been researched 247 extensively since 1973 by Sydney Brenner [57], who eventually won the Nobel Prize in Physiology or Medicine, 248 together with H. Robert Horvitz, and John Sulston in 2002 for their work in C. elegans. It is the first multicellular organism to have had its entire genome sequenced [58]. The complete connectome of these 250 worms have also been mapped out; all 302 neurons, including their connections and synapses are known [59]. 251 It is relatively simple to keep; being non-pathogenic and requiring only bacteria for food. All in all, the ease 252 of culture, small sizes and completely known physiology make them excellent model organisms for biomedical 253 research [60]. 254



Fig. 2.5: Adult C. elegans stained with Sudan black under a microscope. The black dye is lipophilic and adheres to fat cells. The larger granules seen here are eggs. Photo taken in collaboration with NUS BICEPS group.

As a side note, biogenic magnetite, Fe_3O_4 , has been found in C. elegans [61]. This, together with initial reports that neurons in C. elegans responded to magnetic fields [62] made worms especially interesting to study in the context of PEMFs. However, a follow-up study has been unable to replicate the results [63].

$_{258}$ 2.2.1 Worm Culture

The worms were cultured on large plates with agar and bacteria lawns for food. On this plate, they were allowed to grow and lay eggs unhindered. In order to prepare a homogenous (in terms of life cycle) batch of adult worms, an additional synchronisation process was required. Synchronisation was performed 3 days before the planned experimental day and involved the sterilisation of all worms except the eggs. Sterilisation was achieved by repeatedly washing down the worms with bleach, followed by spinning them in a centrifuge to collect the residual pellet. Being more resilient, only the worm eggs are left intact from this process. The pellet, which consisted of the worm eggs and cellular debris, was isolated then and grown on a new 3.5cm plate with agar and bacteria lawn for food over 3 days in an incubator (20 degrees Celsius).

267 2.2.2 Treatment

For the experiment, approximately 50 healthy worms were identified and transferred under a microscope, onto new 3.5 cm Petri dishes filled with agar and bacteria for food. The total number of 50 worm dishes prepared depended on the available yield of healthy worms on the day of experiment. Each dish was then allocated to a specific magnetic field exposure on a designated coil system. The samples were then exposed to the PEMF signals using the different coil systems (Fig. 2.2), each made to output the specific switching profile described in the earlier sections (Fig. 2.1) for a duration of 10 minutes. After PEMF exposure, the 50 worms were washed down with 100 μ l of M9 buffer solution into a single well on a 96-well flat bottom black plate.

$_{76}$ 2.2.3 MitoSOX Dye

Ongoing investigations conducted by BICEPS suggested that using PEMFs acts as an exercise mimetic. 277 This is suggested by monitoring the Reactive Oxygen Species (ROS). ROS are highly reactive molecules and 278 radicals containing oxygen. The main source of superoxide, O₂^{*}-, which is in turn the precursor of many other ROS [64], is the mitochondrial electron transport chain (ETC) during cell respiration [65]. Mitochondria 280 generate Adenosine triphosphate (ATP) by oxidising glucose, lipids or amino acids, effectively transferring electrons to the ETC. This process is not perfect, and sometimes the electrons react with O₂ to form the 282 radical O_2^* [66]. The latter is exacerbated if there is any mitochondrial dysfunction [67]. The superoxide 283 can then be catalysed to other ROS like H₂O₂ or OH* in the mitochondrial matrix or cytosol [68]. As such, 284 O₂^{*}− levels make for good indicators of mitochondrial activity. MitoSOX[™] Red Mitochondrial Superoxide 285 Indicator was used for measuring the superoxide levels in real time over 5 hours after PEMF treatments. 286 MitoSOX red is only oxidised by superoxides and not other ROS. 20 μ l of MitoSOX red reagent was added 287 into each well. A microplate reader (Cytation 5) was used to read the well plate every 2 minutes for an 288 excitation of 396 nm and emission at 579 nm at room temperature. The readout was the relative fluorescence, 289 in arbitrary units, at a sample rate of 2 minutes. 290

$_{291}$ 2.2.4 Results

There were three separate experiments conducted on three different dates, see Figs 2.6 - 2.8, to measure the impact on superoxide levels in C. elegans after PEMF exposures. The different treatments that were applied were the control (no fields applied), an up-test (PEMF with peak +1.5 mT) and down-test (PEMF with peak -1.5 mT). This is because previous experiments suggested possibility of different results for the field oriented up or down.

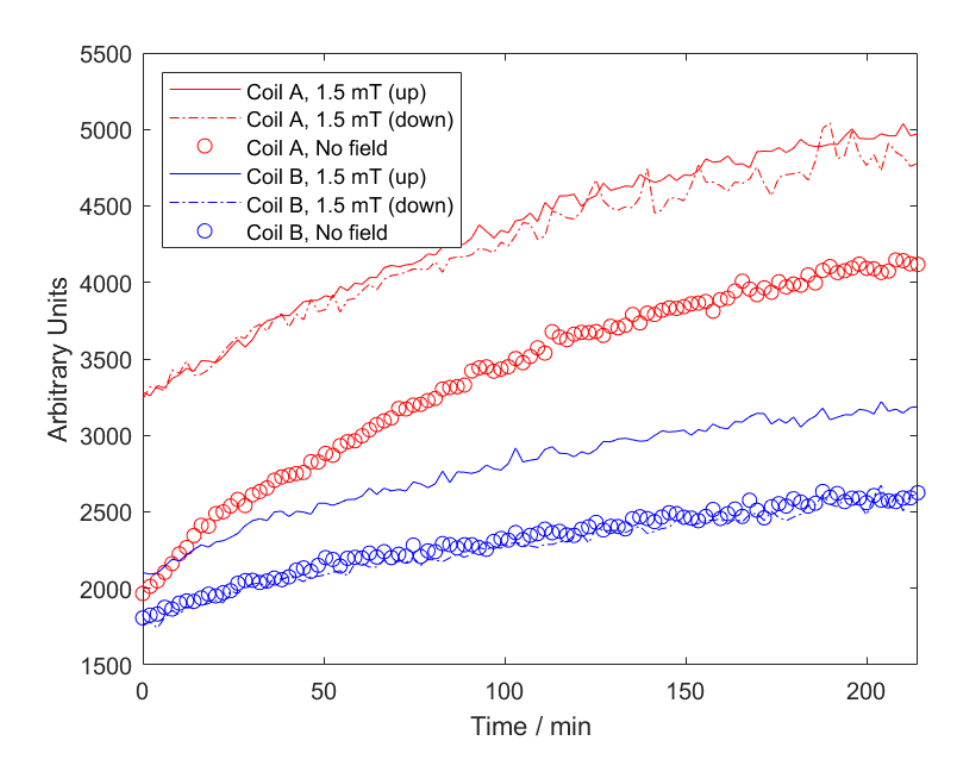


Fig. 2.6: MitoSOX fluorescence readout for C. elegans that have underwent different PEMF conditions: PEMF generated by coil A (red) and B (blue) with field lines directed upwards (solid), directed downwards (dashed) and no field (circles) over three different batches of worms measured on 11 June 2019. The second readout of Coil A, 1.5 mT (down) was voided due to experimental errors.

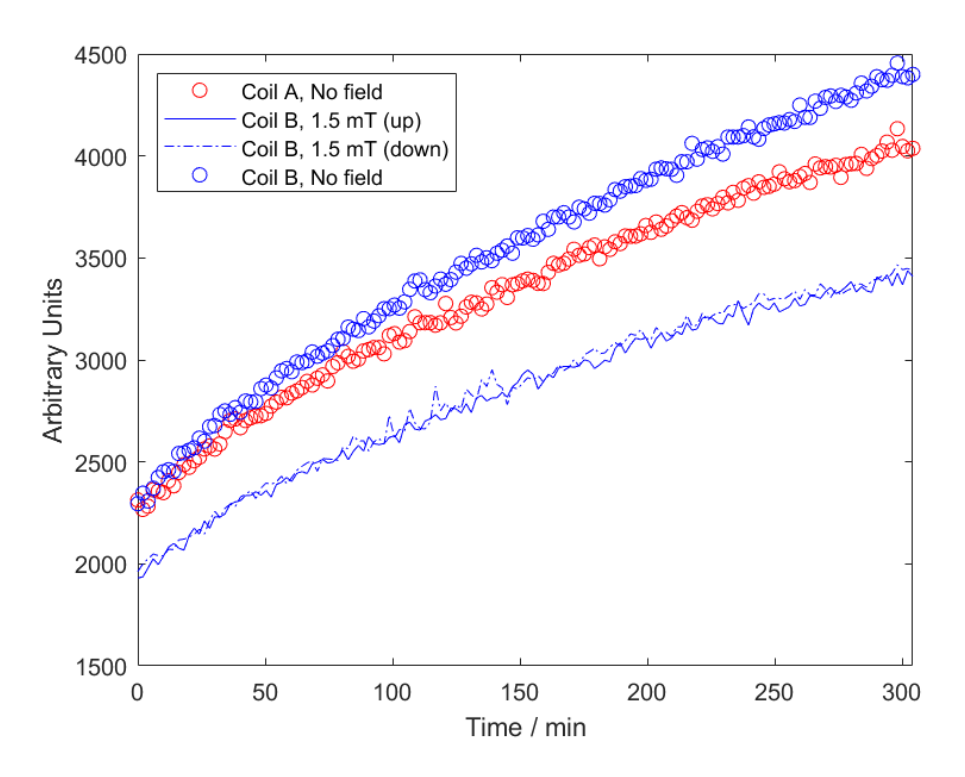


Fig. 2.7: MitoSOX reading on 28 June 2019.

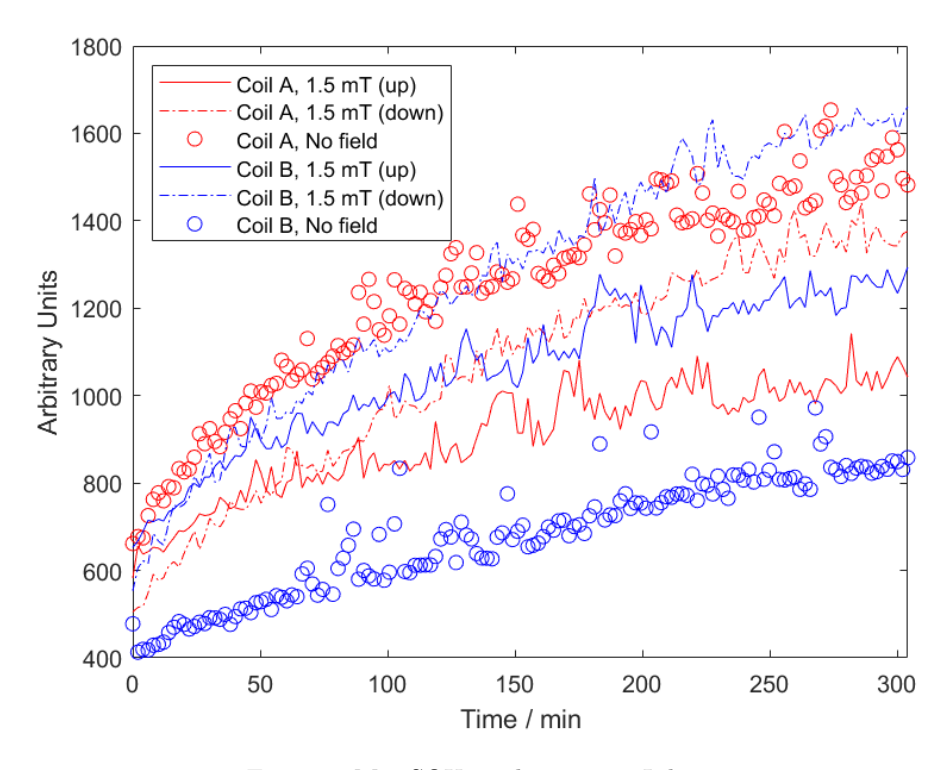


Fig. 2.8: MitoSOX reading on 16 July 2019.

2.2.5Discussion

311

322

323

324

325

326

327

328

329

331

333

334

335

There is a lack of consistency between different experimental runs, with a lot of noise on the third trial (see Fig. 2.8). This is likely due to the lower readout as compared to the other trials, which had readouts that 299 were almost an order of magnitude larger, resulting in a larger signal-to-noise ratio. Due to the anomalous 300 noise, we will exclude these results from comparison with the other two trials. Looking at the first and 301 second trials (Fig. 2.6 and 2.7), we see that the controls of the first trial give different readings. Further-302 more, on comparing between the trials, the 'up' and 'down' conditions in coil B do not show a consistent 303 trend, with the first trial showing different impacts but the second showing the same. Taken together, these 304 inconsistencies suggested that the samples were not uniform or identical across different experimental dates, 305 resulting in different experimental conditions. Evidently, the complexity of utilising a multicellular animal 306 like C. elegans means that synchronising their life cycles is not sufficient to generate homogeneous batches of samples. Other factors like individual worm size or health generated too much variance between samples 308 that complicated the MitoSOX readout. Furthermore, while superoxide levels are strong indicators of mitochondrial activity, the mitochondria itself is ubiquitous to many biological reactions. Thus, the readout 310 was likely confounded by multiple processes, obscuring any magnetic effect, if present. The application of PEMFs did not produce discernible effects on the superoxide levels in vivo C. elegans, and by extension 312 showing no effects on mitochondrial activity. 313

While there were still options to explore with regards to improving experimental protocols in order to improve 314 experimental accuracy and precision, these were beyond available resources and overheads accessible to the scope of our collaboration with BICEPS NUS. 316

Ultimately, the complexity of C. elegans N2 'wild type' introduces many sources of variability, e.g. mutations 317 in the bacterial diet, inter/trans-generational variations, population compositions, etc. [69]. These were 318 thought to be alleviated by moving to the more standardised C2C12 cells which are genetically identical to 319 each other. 320

2.3Cell Proliferation experiments 321

Instead of mitochondrial activity, another avenue of investigation was the effect of PEMF on cell proliferation, i.e the rate of increase in the number of cells. Briefly, we go through a general overview of the process of cell proliferation, loosely following Ref. [70], see Fig. 2.9. Cell division is a highly regulated process, with a mother cell splitting into two daughter cells, with its content split between the two. Adult cells normally reside in a stable resting phase (G0). With appropriate stimuli, cell division is initiated by entering the G1 phase. The G1 phase is a decision making step or checkpoint, with cells either progressing to the synthesis phase (S) or reverting back to G0 based on extracellular signals, e.g. sufficient nutrition or DNA integrity. Deregulation of G1 from mutations is frequently observed in cancer [71]. Replication of cell DNA occurs only in the S phase normally, after which the genetic material is doubled. On completion of the S phase, the cell again enters another regulatory phase (G2). G2 regulates the rate of progression into the next mitosis phase (M) by controlling activation of the proteins cyclin B/cdk1 that subsequently delay the entry into mitosis [72]. During mitosis, the nuclear contents condense into distinct chromosomes that are eventually pulled apart into equal sets by a careful series of movements. The net result of the cell cycle is that a single mother cell divides into two identical daughter cells.

PEMFs have been observed to impact cellular proliferation of mesenchymal stem cells [39–43], granting precedence into this line of experiments. It is worth mentioning, that unlike the experiments on C. elegans 337 monitoring the superoxide levels, cell proliferation is downstream of mitochondrial activity, in that it is initiated by multiple cellular processes and not the starting point. As such, investigating the effects of 339 PEMF on cell proliferation will be casting a wide net, which simultaneously checks multiple cellular process but not reveal specific processes behind any effects. 341

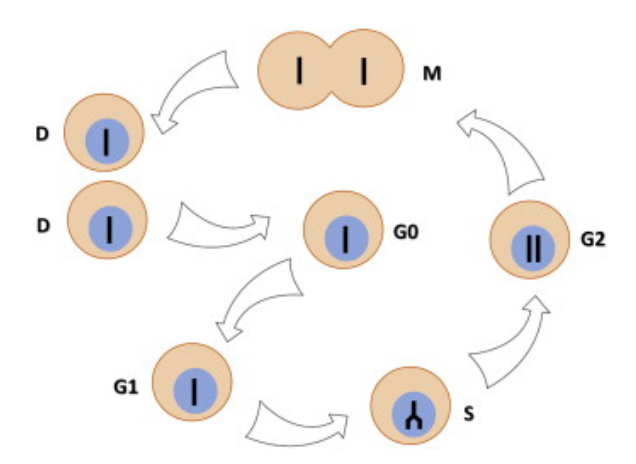


Fig. 2.9: Diagrammatic representation of the cell cycle. Adult cells are normally found in the resting phase (G0), upon which stimuli can bring it into the G1 phase, which is a regulatory phase. If the cell progresses past the G1 phase, by having sufficient nutrition or DNA integrity, then it proceeds to Synthesis (S) and doubles the genetic material, before arriving at another regulatory checkpoint stage (G2). Again, if the appropriate conditions are met, the mother (M) cell divides into daughter cells (D), that both reenter the resting phase. Figure taken from [70].

2.3.1 C2C12 mouse myoblast cell line

The experiments have been performed on the commonly used immortalised mouse myoblast cell line, C2C12. 343 The C2C12 cell line are subclones of myoblasts dating back to 1977 by Yaffe and Saxel [73]. Subcloning transfers only specific DNA sequences from the parent vectors to the new targets, as compared to having 345 full cells that are genetically identical in cloning. Myoblasts are myogenic progenitor cells, i.e. they have the 346 ability to differentiate and fuse into myotubes that eventually mature into myofibers [74]. Optical microscopy 347 images from [75] of C2C12 cells at various time points from the myoblast to myotubes are shown in Fig. 348 2.10. During myogenic differentiation, C2C12 cells organise into tubes and fuse into multinucleated cells. The 349 underlying regulation of myogenic differentiation is highly complex, involving multiple myogenic regulatory 350 factors: Myf5, Mrf4(Myf6), MyoD and Myogenin [76]. In practice, time specific cell culture protocols were 351 utilised to maintain consistency of C2C12 myoblast or myotubes for our experiments, namely by restricting 352 the cell culture confluency, i.e. ratio of the surface of the dish covered by cells. 353

354 Cell Culture

Specifically, the C2C12 mouse skeletal myoblasts used were American Type Culture Collection, LGC Stan-355 dards, Teddington, United Kingdom. These cells were passaged, that is to thaw and transfer cells from 356 the main frozen stock into smaller dishes for experiments, at 48 hr intervals to maintain confluency below 357 40%. Higher confluency levels were avoided as these samples tend to differentiate into myotubes rather than 358 proliferate to more myoblasts. The passage number of the cells used for experiments was kept between 7 to 9. 359 Suitable batches satisfying the confluency conditions were cultured in growth medium consisting of DMEM 360 (Thermo Fisher Scientific, Waltham, MA, USA), 10 % fetal bovine serum (FBS; Biowest, Nuailé,France) 361 and 2 mML-glutamine (Thermo Fisher Scientific) in a humidified incubator at 37°C and 5 % CO₂. 362

The cells were then left to proliferate, with occasional visual inspection under a microscope to look for defects. Typically, a batch of cells was used for experiments once a confluency of about 60-80 % was reached, which translates to about 2 or 3 days in the incubator.

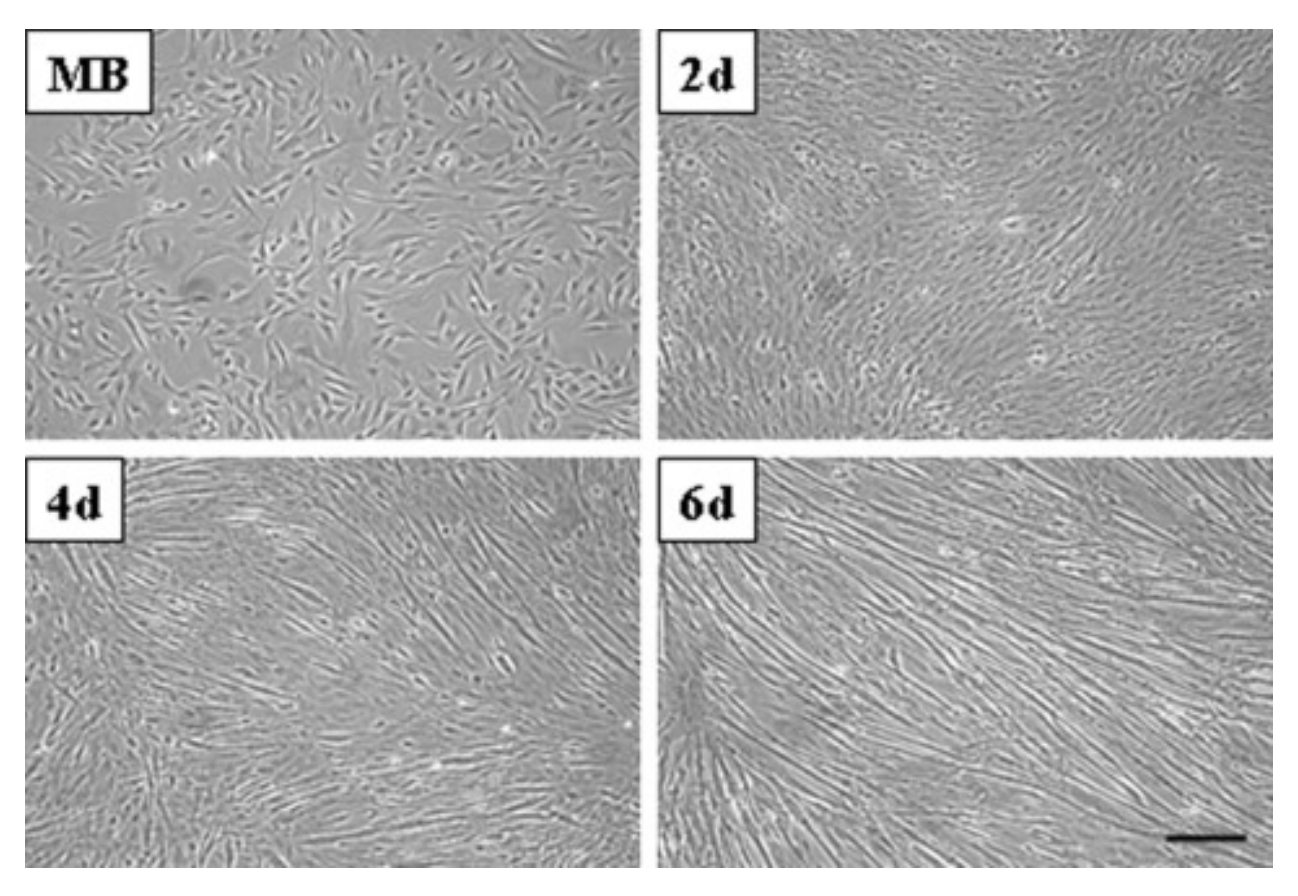


Fig. 2.10: Optical microscopy images of C2C12 cell morphology changes at various time points during myogenic differentiation. Here, the images are taken at the myoblast stage (MB) and at various timepoints, where the 'd' refers to the number of days elapsed from MB. Eventually, the myoblasts complete myogenic differentiation into myotubes by the sixth day. Image taken from [75].

Sample Preparations for cell proliferation experiments

Once the cells have reached the appropriate confluency, they were prepared for use in the experiments.

These cells would have formed a monolayer adhering to their containers and preparartion steps were needed to dislodge them gently into a suspension for handling in the experiments.

Growth media was first drained and the remaining cells washed with 5 ml of Dulbecco's Phosphate-Buffered Saline (DPBS) to rinse off any leftover media. 2 ml of TrypLE express was added to the cells and the T75 flask was incubated for another 5 minutes. This was to break down the cell linings enough to dislodge the cells that have adhered to the flask surface over the 3 day incubation. The TrypLE was neutralised after the incubation by adding 5 ml of media.

To improve consistency across different experimental runs, the resulting solution, now consisting of all the 375 detached cells in a 5 ml media suspension, is diluted with more media to reach a fixed concentration of 25000 376 cells per mililitre. To achieve the desired concentration, the suspension was collected in a 50 ml falcon tube and an aliquot of 10 μ l was removed, mixed with 10 μ l of trypan blue and placed into a hemocytometer. 378 Trypan blue is a staining dye that only interacts with damaged or dead cells, while a hemocytometer is a cell counting chamber consisting of a glass microscope slide with indentations that form a precise volume 380 chamber marked by grid lines. By observing the hemocytometer under a microscope, the cell concentration can be estimated by manually counting the number of unmarked, i.e. viable cells, within the grid lines. 382 The concentration of the remaining batch in the falcon tube can then be calculated from this sample. With 383 the concentration of cells determined, an appropriate volume from the falcon tube containing approximately 384 12500 cells is extracted and placed within small tubes. These tubes were then topped off with media to a 385 total volume of 0.5 ml, which translates to a final concentration of 25000 cells per ml of media. Due to the 386 varying yields on different experimental runs, the number of tubes available for the PEMF treatments were 387 not always the same.

Depending on the available number of tubes on the experimental runs, tubes were designated to a specific coil device (coils A, B and C) and exposure conditions (two directionalities: field oriented 'up' or 'down', and a control: device not powered). Each condition was allocated a minimum of 2 replicate tubes. The tubes were then placed one at a time into each device and exposed to PEMFs with some directionality, or no fields in the case of the controls, for 10 minutes. To avoid asynchronous effects from the 10 minute gap between each batch of samples, randomised permutations of the experimental order were performed.

When PEMF exposure was completed, the tubes were collected and placed into an incubator for 24 hours to proliferate. Two methods were then used to quantify cell proliferation. The first method involves manual cell counting by again using a hemocytometer as already described. The second method utilised spectroscopy of cells together with CyQUANT Direct Cell Proliferation assay to estimate the number of living cells. CyQUANT contains a dye that is cell permeable and binds to DNA in all cells. Another component of the assay is a non-permeable suppressor that masks fluorescence from dead or compromised cells. As such, the fluorescent signal, absorption at 508 nm and emission at 527 nm, will be proportional to the live cell count.

While both methods attempt to measure the same quantity, they are not interchangeable. The hemocytometer method is prone to human errors, either from the aliquoting or counting process. On the other hand, the fluorescence method removes the human errors, but is unable to provide absolute cell counts. Both methods were utilised to track C2C12 myoblast cell numbers after exposures to PEMFs over a total of 10 experiments: 3 using the manual counting and 7 with fluorescence spectroscopy.

¹⁰⁷ 2.3.2 Manual cell count

The exact sequence used to determine the concentration of cells in the media suspension was performed on an aliquot of each tube. From the cell concentration, the corresponding fold change with respect to the controls was calculated for the test conditions. For the manual count, only 3 test conditions were used.

These were two upward and downward orientations in coil A and the fixed downward orientation for coil C.

2.3.3 Fluorescence spectroscopy

Instead of leaving the cells in the tubes within the incubator, the cells were transferred and divided out into 4 wells of 100 μ l per tube on a 96-well plate before being left for the same period of 24 hour incubation. This translates to approximately 2500 cells per well.

CyQUANT direct cell proliferation assay was used for flourescence spectroscopy, which consisted of two 416 components: the CyQUANT direct nucleic acid stain and the CyQUANT direct background suppressor I. 417 To prepare the detection reagent, 5.85 ml of PBS, 24 μ l of CyQUANT Direct nucleic acid stain and 120 μ l 418 of CyQUANT direct background suppressor I were mixed in a tube. 100 μ l of this detection reagent was 419 then added into each well containing cells. The plate now containing the cells mixed with detection reagent 420 was then incubated for 60 minutes to allow the nucleic acid stain to permeate the cells. After this duration, 421 the plate was placed in a CYTATION 5 microplate reader for flourescence readout set with absorption at 422 508 nm and emission at 527 nm. 423

Results

The fold change using the method of manual counting after PEMF exposure in coil A and C are shown in Fig. 2.11 and method of flourescence spectroscopy in Fig. 2.12. These were collated over the course of 3 and 7 experimental runs respectively.

The overall trend using the hemocytometer appears to be an approximately 30 % increase in the cell numbers in 24 hours after the 10 minute exposure to PEMFs in coil C, as compared to no exposure. Coil A appears to have no impact on cell number, even though coil A oriented downward produces similar magnetic field conditions to coil C.

On top of this, the cell count using the CyQUANT assay showed a decrease in cell number with respect to the controls after exposures to PEMF in coils A and B, regardless of directional orientation, while exposures from coil C show no change.

In totality, there were two main observations. Firstly, the different coil systems appeared to produce different impacts on cell proliferation, even though the magnetic fields generated in the 3 systems are almost identical.

Secondly, the cell number counted via fluorescence is about 20 % decreased across all coil systems than when using the hemocytometer. We now describe our attempts to systematically resolve these issues, starting with the first.

440 Discussion

The difference in cell numbers depending on coil system became apparent within the first few initial trials and prompted further investigation into the source of the discrepancy, given that the magnetic fields generated in all 3 systems appear to be identical. However, the destructive nature of the counting methods greatly hindered the ability to narrow down issues. As measurements irreversibly altered the cell samples, they were only performed 24 hours after treatment. This meant that differences in the initial conditions could not be identified or corrected prior.

The main source of (human) error was thought to come from the pipetting step that could negatively impact the cells by introducing excessive shear forces, resulting in inaccurate volumes or inhomogeneous cell concentrations. Practice and standardisation of pipetting techniques (checking for bubbles, controlling plunger speed / pressure, etc.) were performed and every run used blind randomised permutations of the

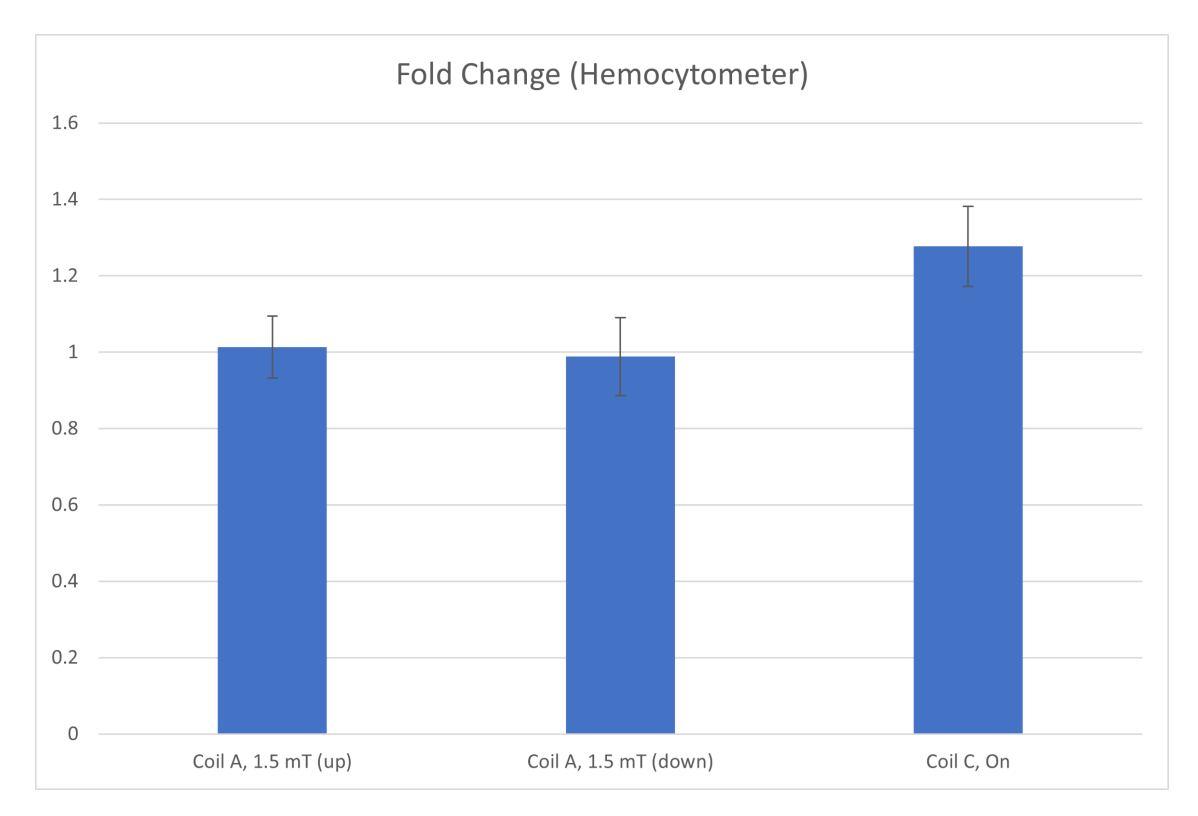


Fig. 2.11: Average fold change of cell number, with respect to the controls, obtained via manual counting method using a hemocytometer over 3 experiments. Error bars shown are the standard errors of the mean.

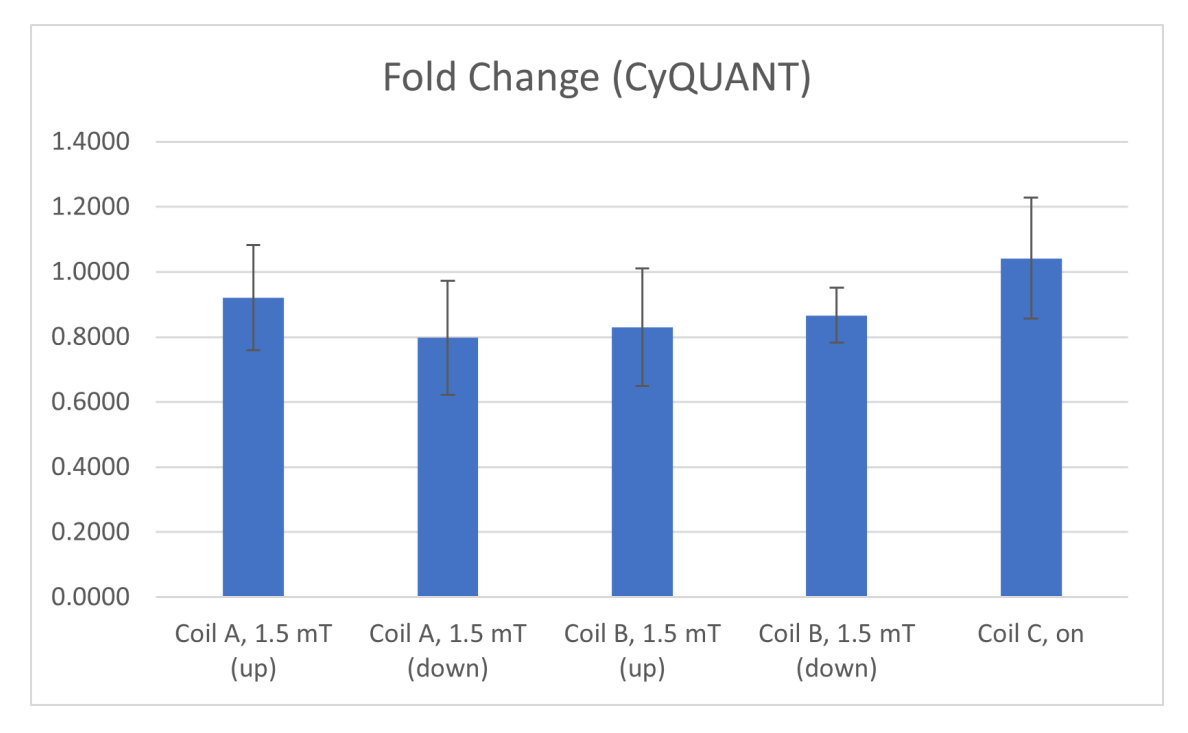


Fig. 2.12: Average fold change of cell number, with respect to the controls, obtained via fluorescent microplate reader (CyQUANT assay) over 7 experiments. Error bars shown are the standard errors of the mean.

sample preparations to average out variations. The latter had an added benefit of eliminating potential systematic bias.

Even with these additional precautions, the inconsistencies between the effect on proliferation from different coils were still prevalent. This prompted an investigation into whether the lighting conditions played a role in the cell proliferation. This functioned as both an investigation into lighting effects as well as to resolve the inconsistencies observed from cells placed in different coil systems.

⁴⁵⁷ 2.3.4 Light/Dark Experiments

The main distinguishing feature of coil C as compared to coils A and B was the magnetic shielding chassis. While the coils supplied the same magnetic field over all 3 devices, the baseline fields (no current in coils) for coils A and B are shifted by the Earth's magnetic field. Although this is thought to be insignificant, with the weak geomagnetic field of around 0.05mT accounting for only 3 % of the 1.5 mT peak values. Another difference caused by the magnetic shielding are the photic conditions experienced by the cells when placed into the chassis. The μ -metal casing blocks ambient light from the cells over the PEMF exposure duration. To study the effect of the combined impact of lighting and PEMF exposure on cell proliferation, 4 sets of experimental conditions were compared. These were PEMF exposure over 10 minutes oriented downwards, PEMF exposure also oriented downwards while covered to block ambient light sources, and the corresponding controls (no PEMFs).

468 Results

The fold change of the cell number after PEMF exposure in light and dark conditions as compared to their corresponding controls are shown in Fig. 2.13. While the cell numbers indicate a slightly larger fold change for the samples exposed in light condition, the error bars on the fold change overlap quite appreciably. Furthermore, the condition of using coil A with ambient light is identical to experiments already performed in both the manual count and fluorescence experiments, which suggests experimental variance. As such, these datasets lack sufficient evidence that lighting conditions play an important role in cell proliferation.

s 2.4 C2C12 cell-derived vesicles

We now attempt to resolve the second issue identified from the cell proliferation experiments. Depending on the method used for counting cells, manual counting using a hemocytometer or fluorescence by CyQUANT 477 assay, there was a discrepancy in the cell numbers but with similar overall trend that coil C conferred either an equivalent (using microplate reader) or increased (using hemocytometer) fold change on the cell proliferation, 479 and was thus most conducive to cell proliferation. A possible explanation would be that PEMF exposure alters the permeability of the cell membrane. Under ideal conditions, only compromised cells are stained by 481 trypan blue, so more selective membranes can inflate the healthy cell count using the hemocytometer. On 482 the other hand, only compromised cells admit the CyQUANT background suppressor so a more permeable 483 membrane can lower the fluorescence signal and in turn the inferred cell numbers. This hinted to some effect on cell permeability. At the time, concurrent experiments also suggested that the mechanism by 485 which PEMFs were interacting with the cellular systems involved Transient Receptor Potential Canonical-1 486 (TRPC1) proteins which are membrane-spanning subunit of store-operated Ca²⁺ channels. Store-Operated 487 Ca²⁺ Channels (SOCs) are plasma-membrane channels that open when levels of Ca²⁺ in the cellular "stores" (sarcoplasmic or endoplasmic reticulum) are low [77]. SOCs have also been linked to cell proliferation by 489 means of regulating calcium entry [78]. This separate study eventually culminated into published works 490 indicating that PEMF exposure could induce TRPC1-mediated calcium entry [38]. To complement these 491

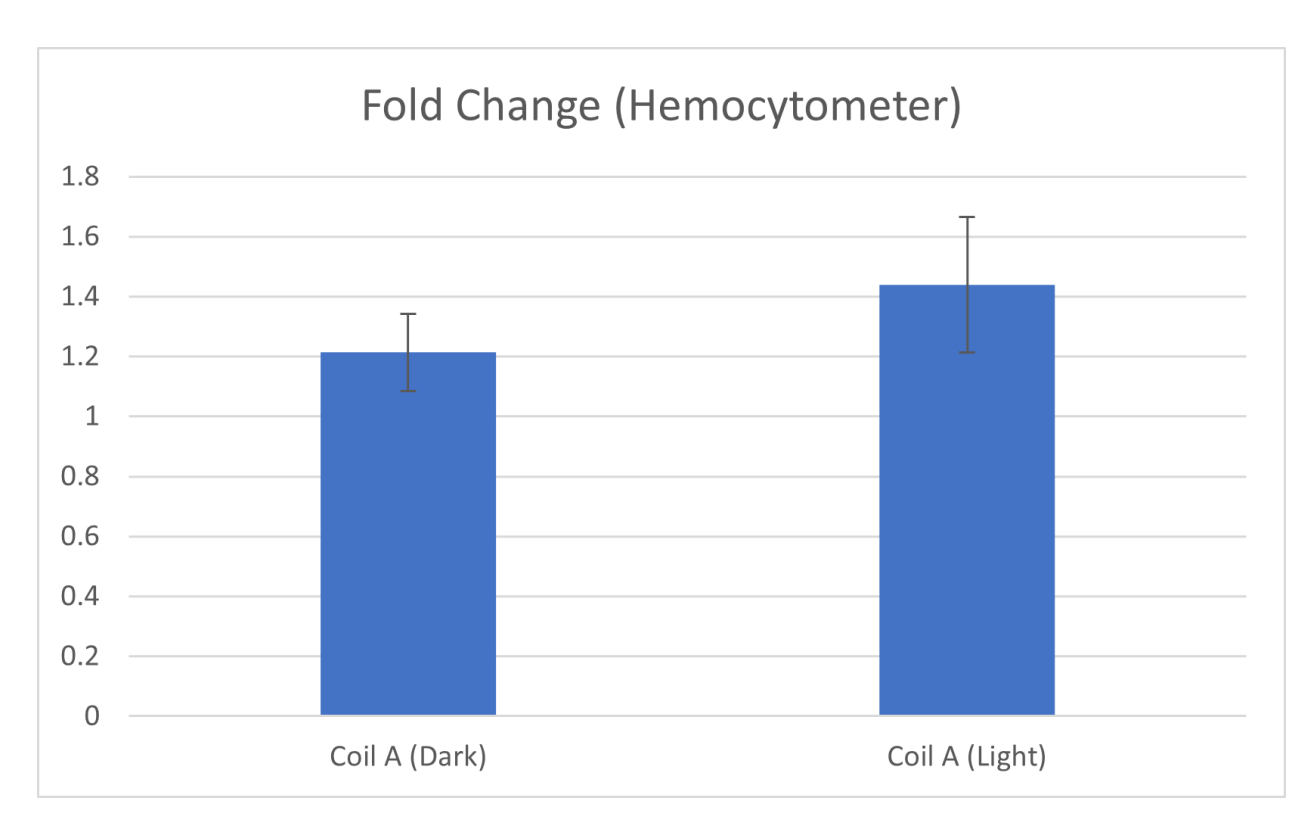


Fig. 2.13: Fold change of cell number using the manual counting method with a hemocytometer, over 4 experiments.

studies into PEMF effects on membrane action, experiments on extracellular vesicles derived from the same C2C12 cells were conducted.

Extracellular vesicles are small fragments of membranes shed physiologically and pathologically by cells [79]. They consist mostly of a lipid bilayer membrane, with remnants of surface and membrane proteins from its origin cell together with cargo from their mother cells [80]. An advantage of working with cell-derived vesicles (CDVs) is that, being essentially a tiny pocket of its mother cell encased in a membrane, they represent a snapshot of the parent cell's physiological state at the time of creation [81]. From a physical point of view, this also significantly reduces the experimental complexity and allows one to focus on the membrane without having to take into account concurrent biological processes when working with the full living cell.

2.4.1 Experiment overview

To test PEMF interaction on cell membrane permeability, calcium levels in C2C12 CDVs were monitored. The calcium levels were obtained by using a cell permeant fluorescent dye, Calcium Green which exhibits increased fluorescence when binding with Ca²⁺. A few intricacies had to be considered in the design of the experiment. Firstly, the protocol for generating CDVs was still not yet well optimised at the time of experimentation. The method eventually decided upon involved agitating the cell membrane into producing blebs and protrusions via a reagent Cytochalasin B. These extrusions, which will eventually constitute the vesicles, were then dislodged using the shear forces from an orbital shaker. In order to generate sufficient shearing force, adhesion of the cell structure is important. Both myoblast and myotubes were utilised to generate CDVs and were also found to produce different types of vesicles, see further elaboration in the following sections. Another consideration was controlling the sources of calcium ions in many of the biological reagents, e.g. growth media, to avoid bleaching the fluorescent dye prematurely. The final experiment outline was as follows: prepare CDVs loaded with Calcium Green from C2C12 myoblast/myotubes while minimising

any contact with calcium containing biological reagents, followed by concurrently introducing the CDVs into a calcium rich environment and exposing them to PEMFs. The treated CDVs were then placed into a fluorescence microplate reader to measure the rate of calcium entry into vesicle interior. We will now describe these steps in more detail.

2.4.2 Preparation of Calcium Green-loaded CDVs

The vesicles were derived from the same C2C12 mouse myoblast cell culture used in the cell proliferation experiments. The starting point is a flask with C2C12 cells. Depending on the experiment, these cells would 520 either be myoblasts or have differentiated into myotubes. Myotubes were obtained by allowing myoblast confluency to exceed 90 %. Growth media was removed and remaining cells were washed with 5 ml of 522 Phosphate-Buffered Saline (PBS), which is similar to the dPBS used in the cell proliferation experiments, except without calcium. Then 2 ml of TrypLE were added, followed by 3 ml of Roswell Park Memorial 524 Institute (RPMI) 1640 medium and Cytochalasin B mixture (200:1). Cytochalasin B is known to induce extrusion of vesicles from the cellular membrane [82]. The mixture was then checked under a microscrope for 526 blebbing, which manifests as tiny bubbles around the muscle cells. If blebbing was observed, the mixture was 527 then placed in an incubated shaker for 20 minutes. The resulting suspension was then transferred into falcon 528 tubes and spun down at 700 g for 5 minutes to separate the cell debris from the vesicles. The supernatant 529 was extracted and spun again at 14000 g for 30 minutes. The pellet is collected and resuspended in 5 ml of 530 RPMI solution and Calcium Green mixture and incubated for 30 minutes to allow the cell-permeable dye to 531 enter the CDVs. The suspension was then spun down again for 10 minutes and the pellets recollected and 532 resuspended in 5 ml of RPMI solution. The suspension is then spun one more time for 5 minutes and the 533 pellets are collected. The sequence of spinning and recollecting of the pellets were to minimise flourescent 534 noise from Calcium Green left in the suspension media. The final pellet is our CDVs loaded with Calcium 535 Green.

537 2.4.3 SEM imaging of CDVs

553

To characterise the CDVs, Scanning Electron Microscopy (SEM) was utilised to determine the distribution of vesicle sizes obtained from myotubes and myoblasts. The Calcium Green loaded CDV pellets needed 539 to be fixed and dehydrated for SEM. The pellets were fixed in 2.5% glutaraldehyde and left overnight in the fridge. The glutaral dehyde solution was then removed and the pellet rinsed with PBS. The buffer 541 solution was removed and the pellets were dehydrated in a 50 % ethanol solution for 15 minutes. This was repeated for ethanol concentrations in 10 % increments up to 100 %, after which the samples were ready for 543 microscopy. CDVs are easily identified as featureless ellipsoid particles as seen from the scanning electron microscope. Exemplary SEM images of myoblast and myotube CDVs are shown in Fig. 2.14, with myoblast 545 vesicles generally having larger diameters than those from myotubes. The sizes of all vesicles identified from 546 multiple SEM images were compiled into a histogram (Fig. 2.15). 547

Both myoblast and myotube vesicles show a bimodal size distribution, with myoblast modes being about 50-75 nm and 200-225 nm, while myotube modes being 30-40 nm and 70-80 nm. Bimodality suggests a mixture of different vesicle subtypes: exomeres (< 50 nm), exosomes (small 60-80 nm, large 90-120 nm) and microvesicles (100 - 1000 nm) [83]. This is attributed to the morphological differences between myoblasts and myotubes, with the latter possessing denser structures and stronger adhesion strengths.

2.4.4 Magnetic field effects on calcium entry

Calcium permeability can be inferred by placing the Calcium Green loaded CDVs into a calcium rich environment and monitoring the fluorescence of the dye. We have exposed the CDVs to two types of magnetic fields: (i) sinusoidal fields and (ii) PEMFs. The results are summarised below.

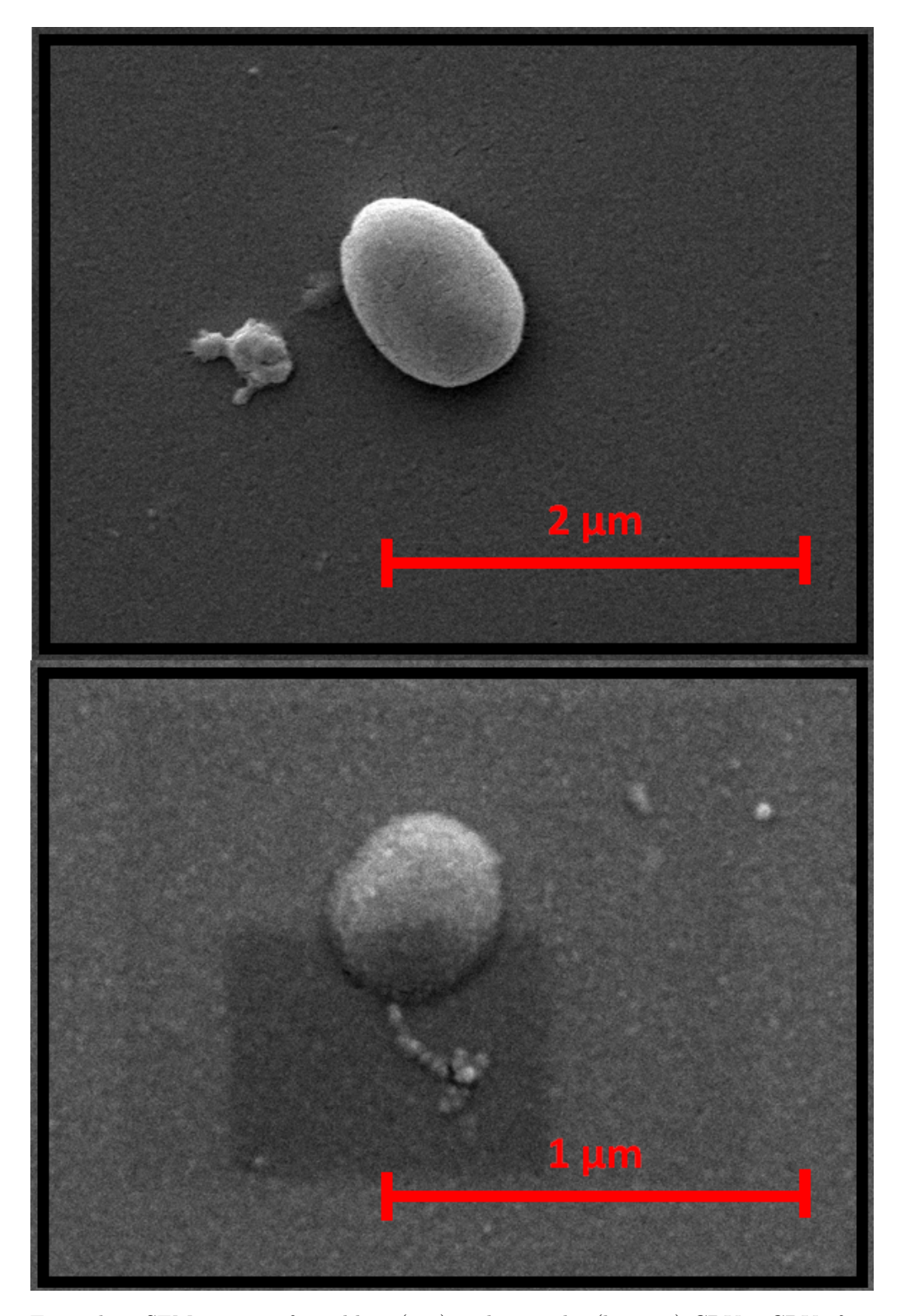


Fig. 2.14: Exemplary SEM images of myoblast (top) and myotube (bottom) CDVs. CDVs from myoblast are typically much larger in size than from myotube.

Exposure to sinusoidal magnetic fields

Using coil A, a wider range of magnetic fields could be applied. Given that the most prominent features of the PEMF signal used thus far were the 150 μ s switching pulses, we have applied a simple sine wave

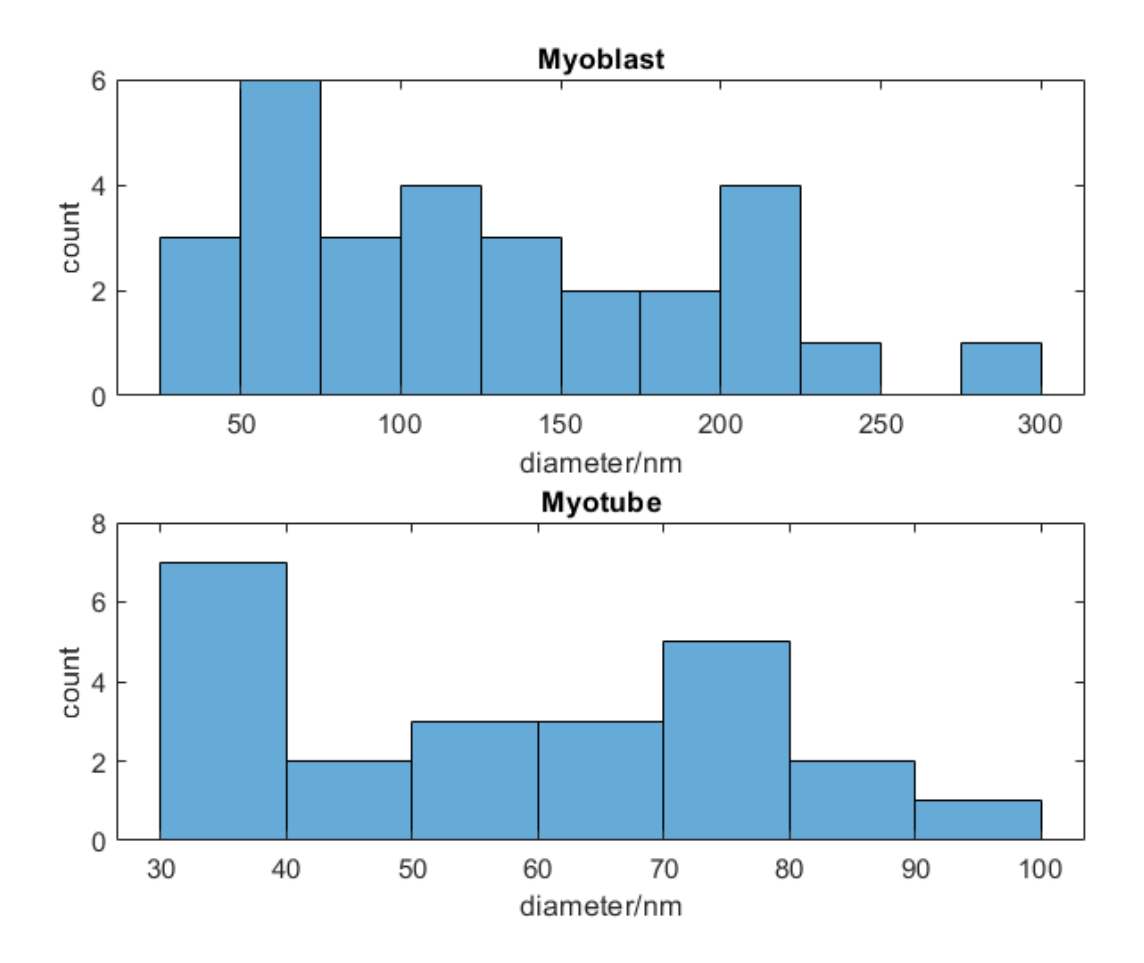


Fig. 2.15: Size distribution of vesicles derived from myoblasts and myotubes.

with 1.5 mT amplitude and frequencies 3.3 kHz and 6.6 kHz. The 3.3 kHz runs were only performed during trials where there was an excess of CDVs, of which the yield varied between batches. Priority was given to ensuring sufficient samples for control and 6.6 kHz runs and there were not always sufficient vesicles to perform the 3.3 kHz runs.

To improve signal to noise ratio of fluorescence during readout, the calcium loaded CDVs pellets were transferred into eppendorf tubes and immersed in 500 μ l of FluoroBrite DMEM, which produces lower background fluorescence than standard DMEM. These tubes were subjected to up to three magnetic field conditions in coil A consisting of a control field in which the coils were not powered, a 3.3 kHz and 6.6 kHz sinusoidal wave with amplitude 1.5 mT over 10 minutes. After exposure, the contents of the tubes were transferred into 96-well plates, 100 μ l per well, and placed into a CYTATION 5 microplate reader. Excitation and emission was set to 510 nm and 535 nm respectively, and fluorescence readout took one hour.

PEMF on myotube CDVs

In this condition, a slight modification to the CDV preparation was made – changing steps involving RPMI to Locke's solution, which is a low calcium medium. This was done to reduce and delay exposure to calcium ions up until the point of readout to avoid bleaching the calcium dye prematurely. Instead of the sine waves, the test condition is PEMF oriented downwards.

Results

Due to variations in fluorescence in each well over the course of experiments, most likely due to different concentrations of vesicles per well, the fluorescence values are normalised to the initial readings per well such that every well always begins at 1. This allows comparison of the proportionate changes in fluorescence across different experimental runs. The average fold change of calcium fluorescence is collated in Fig. 2.16 for myoblast CDVs across 6 different experiments. The compilation for myotube CDVs for exposures to sinusoidal magnetic fields is in Fig. 2.17 and PEMFs in Fig. 2.18.

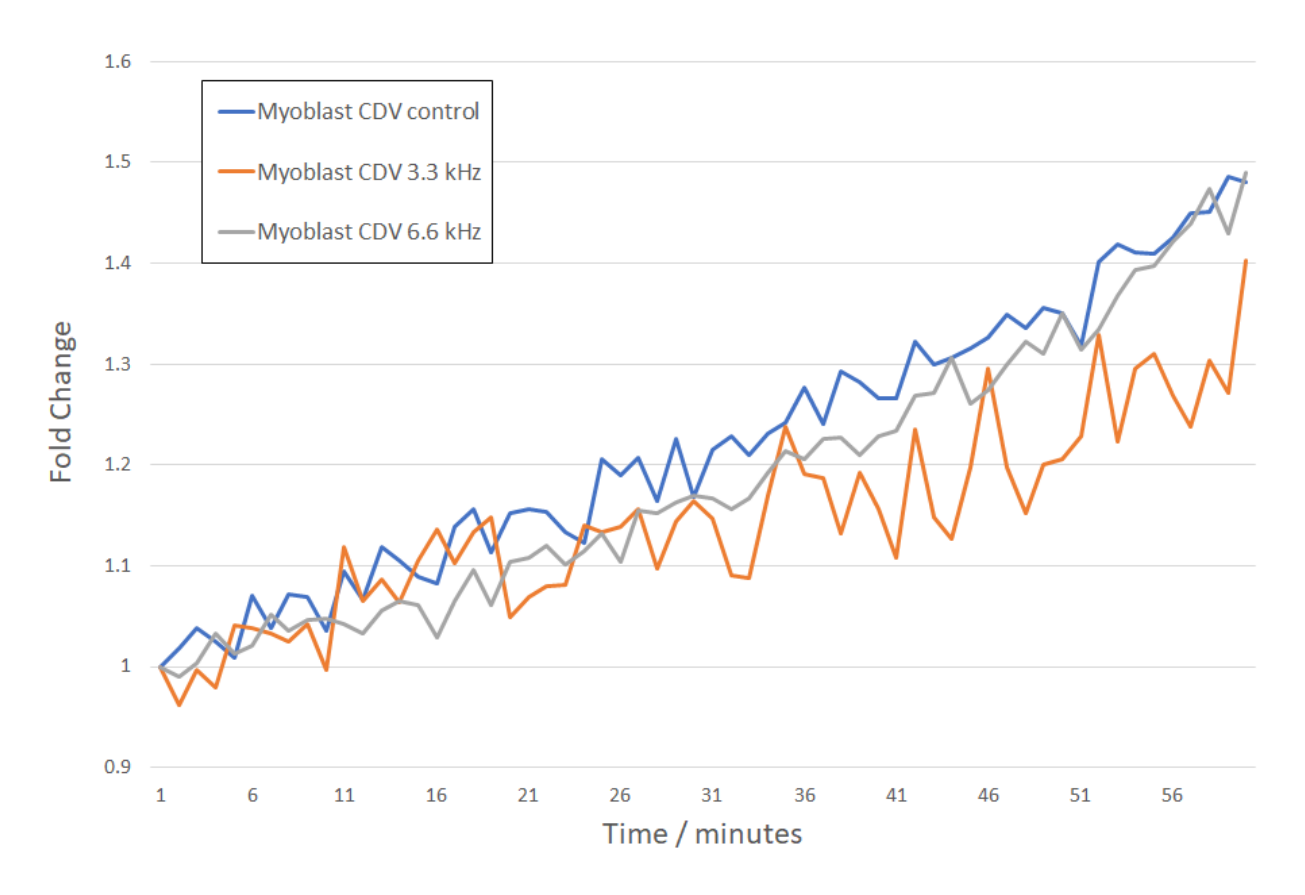


Fig. 2.16: Average fold change of calcium fluorescence in myoblast CDV after 10 minute exposure to control, 3.3 kHz and 6.6 kHz sine wave. The curves are compiled over 6 different experimental runs of the control and 6.6 kHz set and 3 runs with 3.3 kHz. The fold change is relative to the first reading of each condition (this is why every condition always begins at 1).

Discussion

Fig. 2.17 shows a small impact of sinusoidal magnetic field has on the calcium channels of myoblast/myotube CDVs, with the controls producing higher fluorescence. Fig. 2.18 shows no visible effect of magnetic field. This suggests that the pathways in which magnetic fields influence cellular activity are not restricted to membrane actions. Likely they rely on other biochemical interactions present in the full animal cell system that are absent in the vesicle system. Furthermore, decomposing the PEMF signals to their lower harmonics did not reveal any additional insight. However, it is worth mentioning that by reducing the system to the CDVs, many other biological processes that may indirectly lead to increased calcium entry into a cell are disregarded.

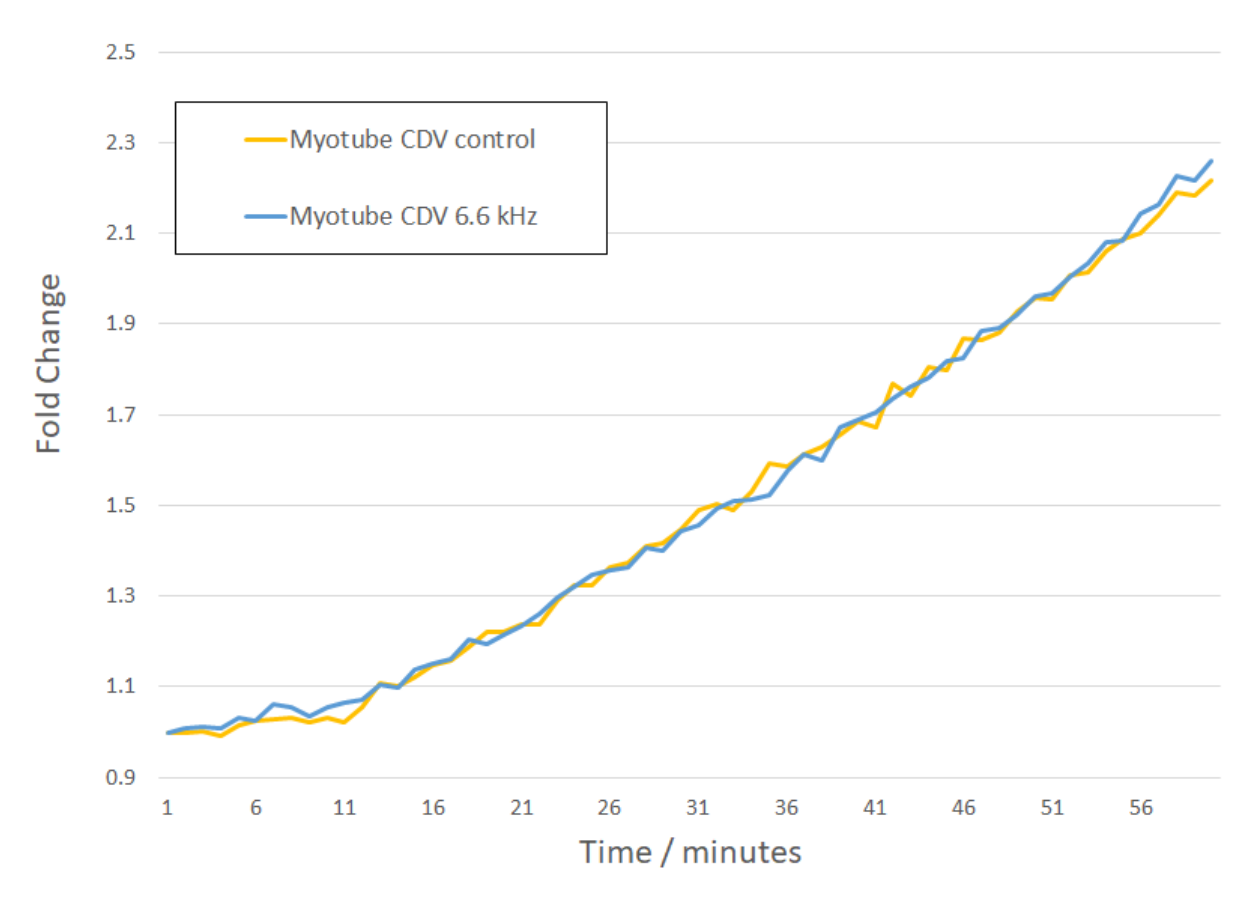


Fig. 2.17: Average fold change of calcium fluorescence in myotube CDV after 10 minute exposure to control and 6.6 kHz sine wave. These were compiled over 2 different experimental runs. The fold change here is taken from the first reading of each condition, such that every condition always begins at 1.

2.5 Conclusion

Several experiments exploring the effects of pulsed magnetic fields on animals, cells and vesicles were conducted, but their results do not show a clear connection between the application of magnetic fields and biological processes. The pulsed magnetic fields studied have a specific profile, see Fig. 2.1, with its most prominent feature being square waves with a minimum and maximum value of 0 mT and 1.5 mT. The various biological processes investigated were the mitochondrial activity of C. elegans, proliferation rate of C2C12 mouse myoblast cells as well as the calcium regulation of C2C12 myoblast/myotube derived vesicles.

Mitochondrial activity was quantified by measuring the superoxide levels in C. elegans via fluorescence microscopy. This was found to yield highly inconsistent data, most likely from the inability to closely control the quality of C. elegans samples across experimental runs, despite attempts to synchronise worm life cycles. Furthermore, the ubiquitous nature of mitochondrial activity in almost all cellular processes would have further lowered the signal to noise ratio, complicating the study. Regardless, it can be concluded that magnetic effects on mitochondrial activity, if any, were not strong enough to be detected using the current experimental protocols.

Cell proliferation of C2C12 mouse myoblasts was quantified by the cell numbers 24 hours from the point of PEMF exposures, measured by two ways: a manual counting method utilising a hemocytometer, and the fluorescence spectroscopy. Both methods yielded different cell quantities but a similar qualitative result was

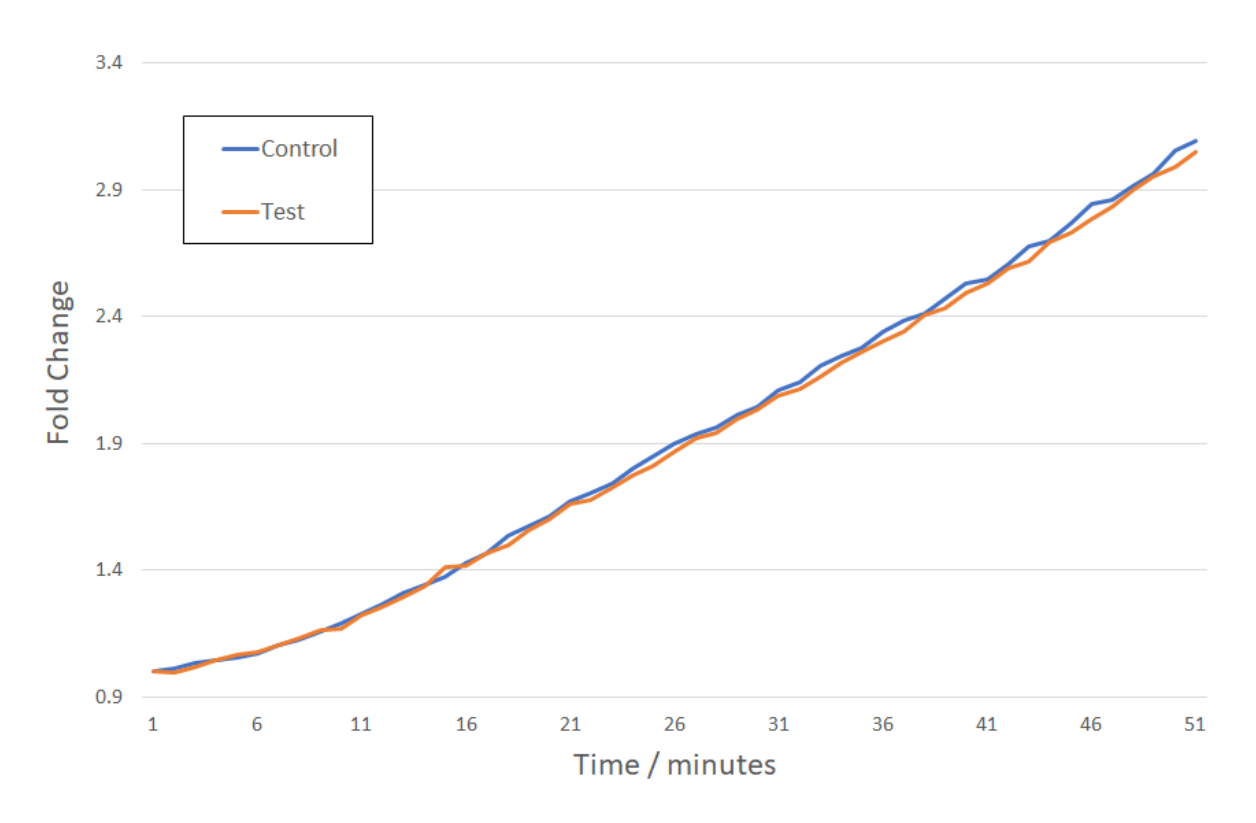


Fig. 2.18: Average fold change of calcium fluorescence in myotube CDV after 10 minute exposure to control and PEMF test field. These were compiled over 4 different experimental runs. As in Fig. 2.17 the fold change is relative to the first reading in each condition.

observed that PEMF exposure through coil C produces higher number of cells as compared to coils A and B. Further investigations into whether the lighting conditions affected cell proliferation were inconclusive. Quantitatively, the cell number estimated from the fluorescence was about 20 % lower across all coil systems. This could be explained if PEMFs altered the permeability of the cells so that either less of the CyQUANT dye binded with DNA or more background suppressors reached the cell interior, prompting focus on the cell membrane.

Calcium entry into myoblast and myotube derived vesicles were monitored using Calcium Green, a fluorescent calcium binding dye. Myoblasts/myotubes were first loaded with the dye and vesicles generated by agitation with Cytochalasin B and shearing forces. Scanning electron microscopy was used to characterise the vesicles generated by the experimental protocols used, finding that myoblasts and myotubes generate different types of vesicles. The dye-loaded vesicles were then placed in fluorobrite and the fluorescence readout indicated the rate of entry of the calcium ions from the media. Both PEMFs and sinusoidal magnetic fields with frequencies corresponding to the most prominent features of the PEMFs did not alter the rate of calcium entry.

In summary, PEMFs do not appear to have a measurable impact on the biological processes investigated in this chapter, namely mitochondrial activity, cell proliferation and calcium entry.

Part II

625

Magnetoreception

In the following chapters, we touch on another possible influence of magnetic
fields on living systems: magnetoreception. Unlike PEMFs on biological
systems, the field of magnetoreception has been around for much longer.

Furthermore, the underlying mechanisms and physical models by which the
magnetic fields interact with certain animals to imbue a magnetic sense has
been hypothesised and, in some cases, confirmed with a good deal of certainty.
We thus move from more exploratory investigations to one that might be more
familiar to the modern physicist.

$_{ iny 15}$ Chapter 3

652

653

654

655

656

657

659

660

661

663

665

667

Most Common Models of Magnetoreception

Magnetoreception is the process of sensing and translating external magnetic information into a sensory input to be utilised. While there are significant gaps in our understanding of the underlying mechanisms of magnetoreception, this thesis will attempt to elucidate what has been found so far and identify questions to be addressed with new experimental and theoretical methods.

Progress in understanding magnetoreception has been slow; not much is known beyond rudimentary models 642 like the radical pair mechanism [5,84] or magnetite models [85]. Two key issues worth mentioning are: (i) 643 design of experiments is particularly challenging due to the lack of our own magnetic sense and hence the lack 644 of intuition to draw on for isolating relevant receptor organs or pathways [86]. This is further compounded by 645 the difficulty in localising or isolating magnetic fields. Another consideration is (ii) narrowing down a species to investigate. Although prevalent across a diverse range, not all species are ideal in laboratory studies. 647 Potential issues that arise, with migratory species in particular, are the requirement of large staging areas to observe directional drifts only visible across long distances, while others occupy highly specific ecological 649 niches that require specialised setups, see [11-13, 16, 87-89]. These increase the complexity of experiments as well as place constraints on the freedom to tweak experimental environments. 651

Beyond magnetotactic bacteria, the full mechanism behind magnetoreception is not known. Magnetotactic bacteria utilise magnetotaxis to passively align with magnetic field lines [9], without a need for an active sense. This is achieved via chains of magnetic crystals encased in membranes rigidly connected to the bacteria so that the magnetic torque can directly steer the whole organism. In larger and more complex multicellular organisms like birds, an added layer of transduction pathways to convert the magnetic field information into useful signals to the organism is required. As such, it is helpful to breakdown description of magnetoreception into two processes: (i) the sensing portion and (ii) the interpretation of the signals. In this chapter, we will only be focusing on the former that will be more relevant to a physicist, with the latter leaning more to the field of neuroscience and biochemistry. More specifically, we will look into the physical processes that can comprise a rudimentary magnetic sense.

The usual candidate explanations for magnetic sensing includes ferromagnetic-based models [85] and the radical pair model [5,84,90]. The former involves the presence of ferromagnetic deposits that act like tiny compasses, while the latter involves chemical reactions with distinct products that can be modulated by an external magnetic field. These processes are not mutually exclusive and can be present in a single animal [19]. Alternative ideas exist, for example, many experimental findings are compatible with the model based on magneto-elastic properties of cells [91], where the magnetic information is directly transduced into electrical signals without necessitating a magnetic torque, but will not be in the scope of the thesis.

3.1 Ferromagnetic-based models

Ferromagnetic-based models are one of the more well-known models for magnetoreception. Much like how early humans utilised magnetic compasses to discern cardinal directions, small chains or crystals of ferromagnetic materials can align to the geomagnetic field, providing directional and navigational input to animals. Ferromagnetic deposits like the iron oxide, Fe₃O₄, also known as magnetite [92] and a sulphur equivalent, greigite Fe₃S₄ [93], have been detected in animals and even in human brains [94]. Both magnetite and greigite can also be present concurrently, in the case of magnetotactic bacteria. For our purposes, we will generalise the term magnetite to include all ferromagnetic deposits as the composition of these particles appears to be unimportant - essentially being just two iron rich variants.

3.1.1 Size considerations

To understand the importance of the size parameter in magnetites, we will first derive the Brillouin and Langevin functions in a similar manner to that outlined by Kittel [95]. We begin with the simplest of cases: the single-domain (SD) magnetic particle. Here, we refer to an SD magnetite as one that has a fixed homogenous magnetisation across the entire particle. As such, we can treat the SD as a giant atom with magnetic moment

$$\mu_{\mathbf{J}} = -g\mu_{B}\mathbf{J},\tag{3.1}$$

where **J** is the sum of the orbital and spin angular momenta in the SD. The constants g and μ_B are the electronic g-factor and Bohr magneton respectively. In the presence of an external magnetic field, **B**, the energy levels of the SD grain are given by:

$$E_m = -\boldsymbol{\mu}_J \cdot \boldsymbol{B} = -g\mu_B m_J B,\tag{3.2}$$

where m_J is the angular momentum quantum number taking on one of the values from -J, -J+1, ..., J.
Note that m_J refers to a specific quantum number out of the possible 2J+1 values. We will drop the subscript J from m_J here on.

In an environment, Brownian motion acts in opposition to any attempt for alignment. At some tempreature T, the occupation probability for each of these states is given by the Boltzmann distribution

$$P(m) = \frac{1}{Z}e^{-E_m/k_BT},$$
(3.3)

where Z is the partition function. For reasons that will be clear shortly, we make the substitution $\gamma = Jg\mu_B B/k_B T$, a ratio between maximal magnetic (Zeeman) energy and thermal energy. Explicitly, the partition function Z is

$$Z = \sum_{m'=-J}^{J} e^{\gamma m'/J},$$
 (3.4)

and we can calculate the expected value of m to be,

$$\langle m \rangle = \sum_{m=-J}^{J} m \cdot P(m) = \left(\sum_{m=-J}^{J} m e^{\gamma m/J} \right) / \left(\sum_{m'=-J}^{J} e^{\gamma m'/J} \right). \tag{3.5}$$

We can rewrite both series with the help of the ratio $r = e^{\gamma/J}$ to obtain for denominator:

$$\sum_{m'=-J}^{J} e^{\gamma m'/J} = e^{-\gamma} + e^{-\gamma}r + \dots + e^{\gamma}$$
(3.6)

$$=\sum_{k=0}^{2J}e^{-\gamma}r^k\tag{3.7}$$

$$=e^{-\gamma} \left(\frac{1 - r^{2J+1}}{1 - r} \right), \tag{3.8}$$

and similarly for the numerator,

$$\sum_{m=-J}^{J} m e^{\gamma m/J} = -J e^{-\gamma} + (-J+1)e^{-\gamma}r + \dots + J e^{\gamma}$$
(3.9)

$$= \sum_{k=1}^{2J+1} [-J + (k-1)]e^{-\gamma}r^k$$
(3.10)

$$= \frac{-Je^{-\gamma} - (J+1)e^{-\gamma}r^{2J+1}}{1-r} + \frac{e^{-\gamma}r(1-r^{2J+1})}{(1-r)^2}$$
(3.11)

$$= \frac{e^{-\gamma}}{1-r} \left[-J - (J+1)r^{2J+1} + \frac{r(1-r^{2J+1})}{1-r} \right]. \tag{3.12}$$

Putting everything together, and noting that $\frac{r+1}{r-1} = \coth\left(\frac{1}{2J}\gamma\right)$,

$$\langle m \rangle = \frac{-J - (J+1)r^{2J+1}}{1 - r^{2J+1}} + \frac{r}{1-r}$$
 (3.13)

$$=J\left(\frac{r^{2J+1}+1}{r^{2J+1}-1}\right)+\frac{1}{2}\left(\frac{r^{2J+1}+1}{r^{2J+1}-1}\right)+\frac{1}{2}+\frac{r}{1-r} \tag{3.14}$$

$$= (J + \frac{1}{2})\coth\left(\frac{2J+1}{2J}\gamma\right) + \frac{1}{2}\left(\frac{r+1}{r-1}\right) \tag{3.15}$$

$$= (J + \frac{1}{2}) \coth\left(\frac{2J+1}{2J}\gamma\right) + \frac{1}{2} \coth\left(\frac{1}{2J}\gamma\right) \tag{3.16}$$

$$= JB_J(\gamma), \tag{3.17}$$

where we call the $B_J(\gamma)$ term as the Brillouin function:

$$B_J(\gamma) = \frac{2J+1}{2J} \coth\left(\frac{2J+1}{2J}\gamma\right) - \frac{1}{2J} \coth\left(\frac{1}{2J}\gamma\right). \tag{3.18}$$

For real values of γ and J, the Brillouin function has upper and lower bounds of +1 and -1, and implies:

$$\lim_{\gamma \to \pm \infty} \langle m \rangle = \lim_{\gamma \to \pm \infty} J B_J(\gamma) = +J, \tag{3.19}$$

with the last equality coming from the fact that negative values of γ imply that J is also negative. Intuitively, if our SD grain has a much larger Zeeman energy as compared to its thermal energy, then it will face negligible opposition to align with the external field and attain its maximal value for angular momentum, J. Given that we can expect a large number of electrons for any appreciable biological length-scales, we can further simplify the Brillouin function in Eq. 3.18 in the limit that $J \to \infty$, to the Langevin function:

$$L(\gamma) = \coth(\gamma) - \frac{1}{\gamma}.$$
 (3.20)

A plot of the Langevin function is shown in Fig. 3.1, together with the typical magnetite sizes found in some organisms [96]. We may think of the Langevin function in our context as a measure of alignment to the external field. Specifically, for magnetoreception, the values of B and T are fixed to the Earth's magnetic field (about 0.05 mT) and body temperature of host organism (or room temperature for organisms without thermo-regulation, about 300 K) respectively, making the parameter γ , and by extension the Langevin function, a function of J only. In summary, Eq. 3.20 suggests that the alignment of free SD particles depends only on the value of J, the maximum projection of the angular momenta onto the aligning field. With ferromagnetic material discovered so far being mostly greigite and magnetite, we can assume that their constituents are fairly uniform so that the main parameter for J is the size and volume of these ferromagnetic deposits.

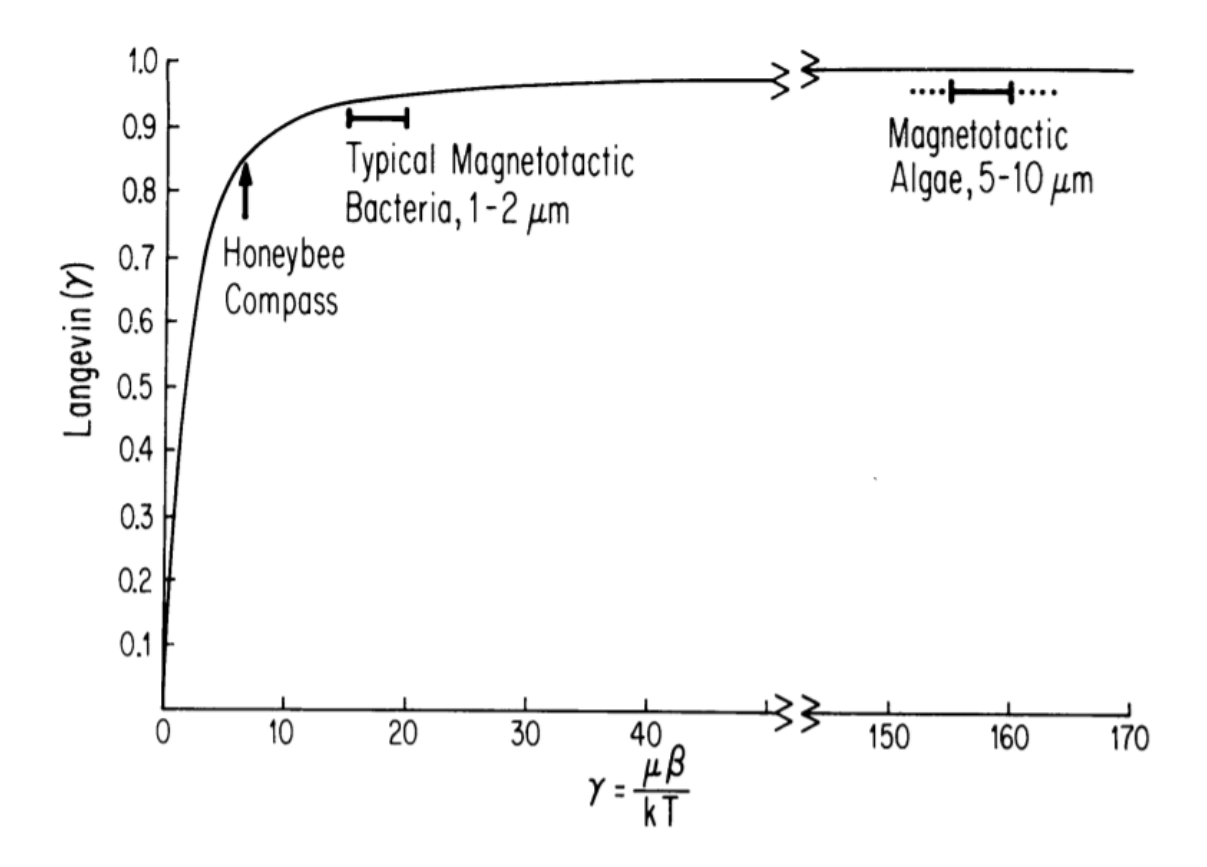


Fig. 3.1: Average alignment of magnetites against ratio of magnetic to thermal energies. The average alignment is 0.99 for algae, 0.94 for bacteria and 0.82 for honeybee, which are quite similar regardless of their varying magnetic/thermal ratios. Taken from [96].

The magnetite grain performs well for values of γ such that the Langevin function is close to 1. At lower values of γ , thermal fluctuations tend to be a significant enough hindrance to cancel out the effect of alignment to the external field. In this regime, the magnetites are superparamagnetic and are unlikely to be useful for magnetoreception. On the other hand, at the upper limit of sizes, Brown showed that it becomes more energetically favorable to form multiple distinct single domains or a "multi-domain" (MD) configuration, oriented to minimise the magnetic energy density [97], and consequently there will not be enough of a magnetic moment to be useful in magnetoreception. This is a delicate balancing act between the magnetostatic (with additional terms due to the domain interfaces), exchange and anisotropy energy terms that is solved numerically. For the most part, magnetites discovered so far fall within the size ranges that make them single domain, see Fig. 3.2.

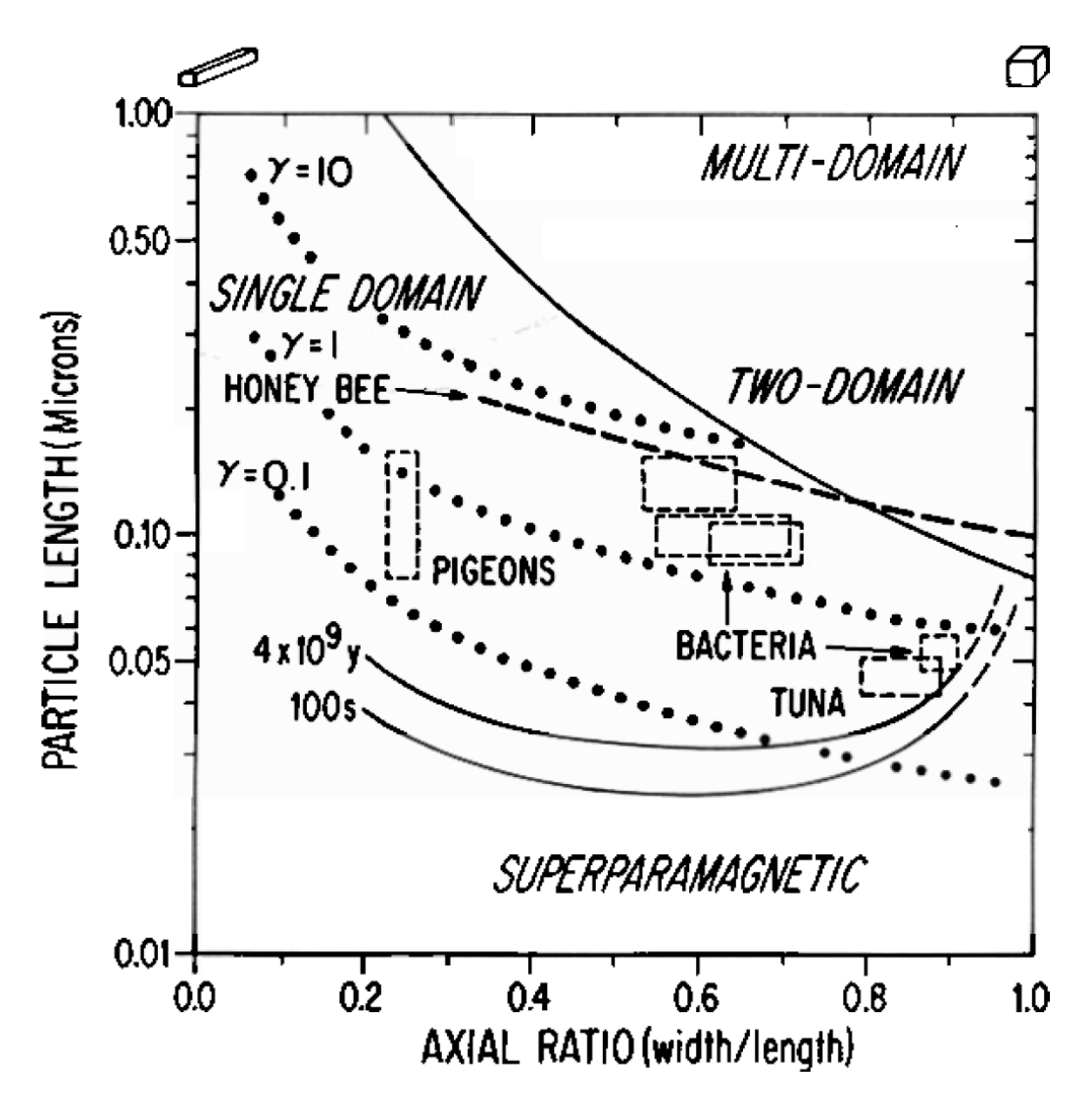


Fig. 3.2: Magnetic stability of rectangular magnetite particles. The solid lines are the theoretical partitioning of magnetite between its superparamagnetic, single-domain and multidomain configurations based on its size and shape. The dotted lines are contours with constant ratios of $\gamma = 0.1$, 1, 10 at body temperature. Most magnetite discovered in animals is also shown, residing in the single-domain region. Taken from [96]

It should be mentioned that, although our discussions may be overly simplified, the more recent models capitalising on computational advancements arrive at similar conclusions. By considering more complex nonuniform SD grains, the particle length for SD to MD transition in cubic magnetite was found to be tightened from about 76 nm to 73 nm. This correction is more pronounced for axial ratios of 0.4, reducing the length from 420 to 320 nm [98]. More detailed discussion on the transitions from SD to MD for magnetite can be found in [98–101], and in [102] for greigite. The fact remains that generally speaking, for magnetite particles to be useful in magnetoreception, they cannot be too small or too large so as to be in a stable and magnetically uniform single-domain configuration.

3.2 Radical Pair model

The radical pair mechanism (RPM) explains how a magnetic field can alter reaction kinetics via the spin dynamics of these radical pairs. Conceived in 1969 by Closs, Kaptein and Oosterhoff (CKO model) [103,104] as an explanation to Chemically Induced Dynamic Nuclear Polarization (CIDNP), which has ever since been an important technique in NMR spectroscopy [105, 106]. It was only about a decade later than Schulten and others proposed it to be involved in magnetoreception in 1978 [5]. It is worth stressing that this model requires quantum coherence.

An overview of a generic radical pair reaction, simplified to only the rudimentary components, is described as follows. It begins with the creation of a radical pair from some larger precursor molecule. A radical is an atom with an unpaired electron and hence a net angular momentum inherited from its unpaired spin, and a radical pair is two such radicals created simultaneously. This process could occur in a number of ways, perhaps a chemical reaction or photoexcitation, as long as the generation of the pair is coherent. Since we are concerned over the interaction with a magnetic field, we focus only on the unpaired electron pair. This system is described by two spin $\frac{1}{2}$ particles in a superposition of singlet and triplet states. By interacting with the magnetic field, transitions between the singlet and triplet states are possible. Additionally, the singlet and triplet states give rise to chemically distinct products, so that the final products depend on the singlet-triplet populations of its intermediate states. While semi-classical approximations to the spin dynamics can produce similar outcomes, coherence [107] and entanglement [108] both lead to enhancements of the chemical yield in the final populations. The net result, summarised in Fig. 3.3, is a chemical reaction whose products are modulated by a magnetic field.

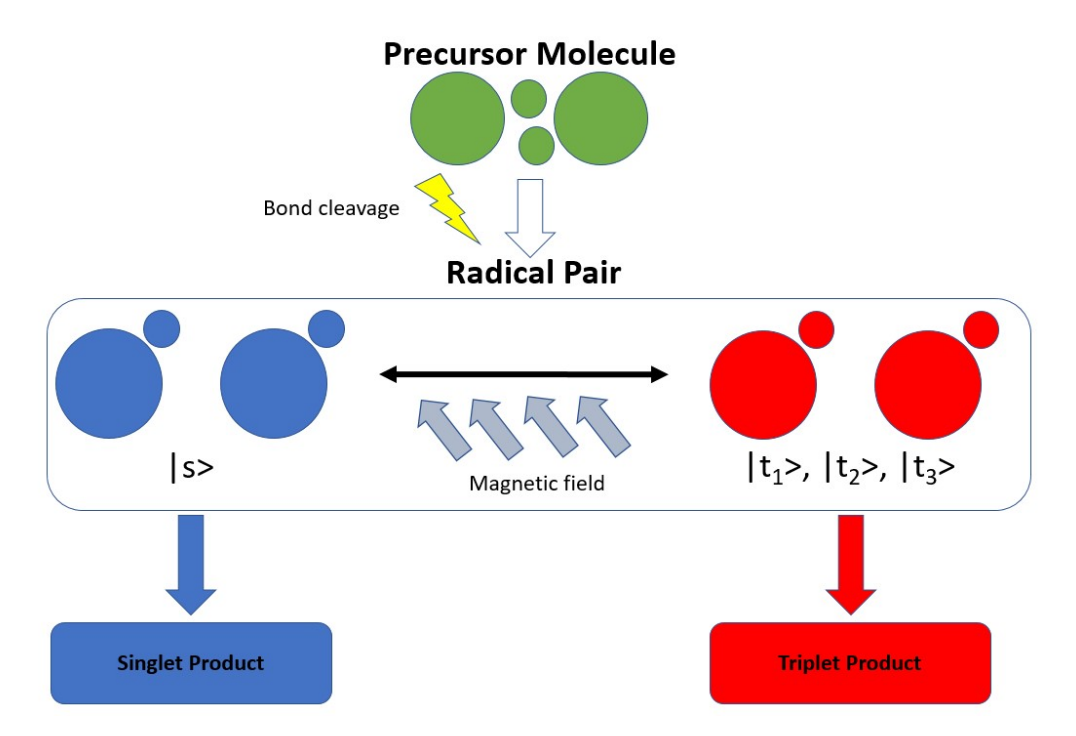


Fig. 3.3: Overview of a generic radical pair reaction. It begins with the generation of the radical pair from some precursor molecule. The radical pair, simplified to a two spin $\frac{1}{2}$ particle system, evolves in the presence of a magnetic field between the singlet or triplet states (local magnetic field for each electron is different due to interactions with the remaining of the radical). The chemically distinct final products depend on the populations of the radical pairs in the singlet or triplet state.

In order for transitions between the singlet, $|s\rangle = |\uparrow\downarrow\rangle - |\downarrow\uparrow\rangle$, and triplet states, $|t_1\rangle = |\uparrow\uparrow\rangle$, $|t_2\rangle = |\downarrow\downarrow\rangle$, $|t_3\rangle = |\downarrow\downarrow\rangle$

 $|\uparrow\downarrow\rangle + |\downarrow\uparrow\rangle$, to happen, there must be asymmetry in the fields experienced by each radical electron. This is achieved because each radical is distinct and the local hyperfine interactions experienced by each electron 753 is different. Effectively, each electron then experiences a different local field. To distinguish between the cardinal directions, some degree of spatial anisotropy is required, and is usually provided by anisotropic hyperfine interactions. 756

3.2.1Toy Model

754

758

759

760

761

762

763

764

765

769

771

772

773

774

780

781

782

784

785

787

Following the work of Gauger and others [109], we present perhaps the simplest toy model for the RPM. In this model, we have two electron spins and one nuclear spin degree of freedom. Only electron 1 interacts with the nuclear spin via hyperfine interactions, with electron 2 being free after the pair is created. Both electrons experience a Zeeman interaction with a local magnetic field. This is the asymmetry required for singlet-triplet transitions. The directionality is introduced via the nucleus with anisotropy along axis z in the Cartesian coordinates, giving a diagonal hyperfine tensor, $\bar{A} = \text{diag}(a, a, 2a)$, with $a = 0.5 \times 10^{-5}$ meV. This is the simplest form of anisotropy required to give the compass directionality, with similar magnitude to numerics in [110] and [109]. The Hamiltonian of the model reads:

$$H = I \cdot \bar{A} \cdot S_1 + \gamma_a B \cdot (S_1 + S_2), \tag{3.21}$$

where I is the nuclear spin operator, \bar{A} the hyperfine tensor, $S_i \equiv \frac{\hbar}{2} \{\sigma_x^i, \sigma_y^i, \sigma_z^i\}$ the spin operators with the subscript referring to electrons in the radical pair, γ_g the gyromagnetic ratio and B being the external 767 magnetic field. We express the magnetic field in spherical coordinates,

$$B = B_0(\cos\phi\sin\theta, \sin\phi\sin\theta, \cos\theta), \tag{3.22}$$

where the magnitude of the field is given by B_0 , and its polar and azimuthal angles, relative to the nuclear axis, are ϕ and θ . Due to the axial symmetry of the hyperfine tensor, it is sufficient to fix $\phi = 0$ without a loss of generality. While the three spins evolve in the magnetic field, incoherent chemical reactions, characterised by some decay constant k, concurrently remove some of the populations depending on which state the electron pairs are in. These decay channels can be described by introducing the shelving states for the singlet product, $|S\rangle$, and triplet product, $|T\rangle$, and using a Lindblad master equation:

$$\dot{\rho} = -\frac{i}{\hbar}[H, \rho] + k \sum_{i} P_{i} \rho P_{i}^{\dagger} - \frac{1}{2} (P_{i}^{\dagger} P_{i} \rho + \rho P_{i}^{\dagger} P_{i}), \qquad (3.23)$$

where P_i are the set of 8 decay operators: $|S\rangle\langle s,\uparrow|,|T\rangle\langle t_1,\uparrow|,|T\rangle\langle t_2,\uparrow|,|T\rangle\langle t_3,\uparrow|,$ and another 4 operators for the nucleaus in the down state, where we use the convention of $\mathcal{H}_1 \otimes \mathcal{H}_2 \otimes \mathcal{H}_N$ for the Hilbert space of 776 the electron 1, electron 2 and nuclear spin system. The readout chemical signal is then the singlet yield or triplet yield, given by the steady state population in $|S\rangle$ or $|T\rangle$ respectively. The initial state is set to be the 778 electron pair in the singlet state and the nucleus as a completely mixed state:

$$\rho(0) = |s,\downarrow\rangle\langle s,\downarrow| + |s,\uparrow\rangle\langle s,\uparrow|. \tag{3.24}$$

The initial state of radical pairs in Drosophila, Arabidopsis, Synechocystis, Human (DASH)-type cryptochrome, which are the main and only candidates for magnetically sensitive proteins so far [111], has been verified to be the singlet state in time-resolved EPR spectroscopy [112,113]. Since we are interested in magnetoreception, the main parameters to be estimated are the strength and angular orientation of an aligning 783 magnetic field. Fig. 3.4 shows the singlet yield as a function of θ , with magnetic field strengths similar to the Earth's field. Indeed, the singlet yield displays a non-trivial dependence on θ . For this toy model to be a plausible magnetic sense, an appreciable variation in the singlet yield over different angular orientations is required in order to resolve cardinal directions. Though not necessary, a one-to-one correspondence between the yield and θ is also ideal and indeed present in Fig. 3.4.

A unique consequence of the RPM is that oscillatory magnetic fields can alter the spin dynamics, potentially

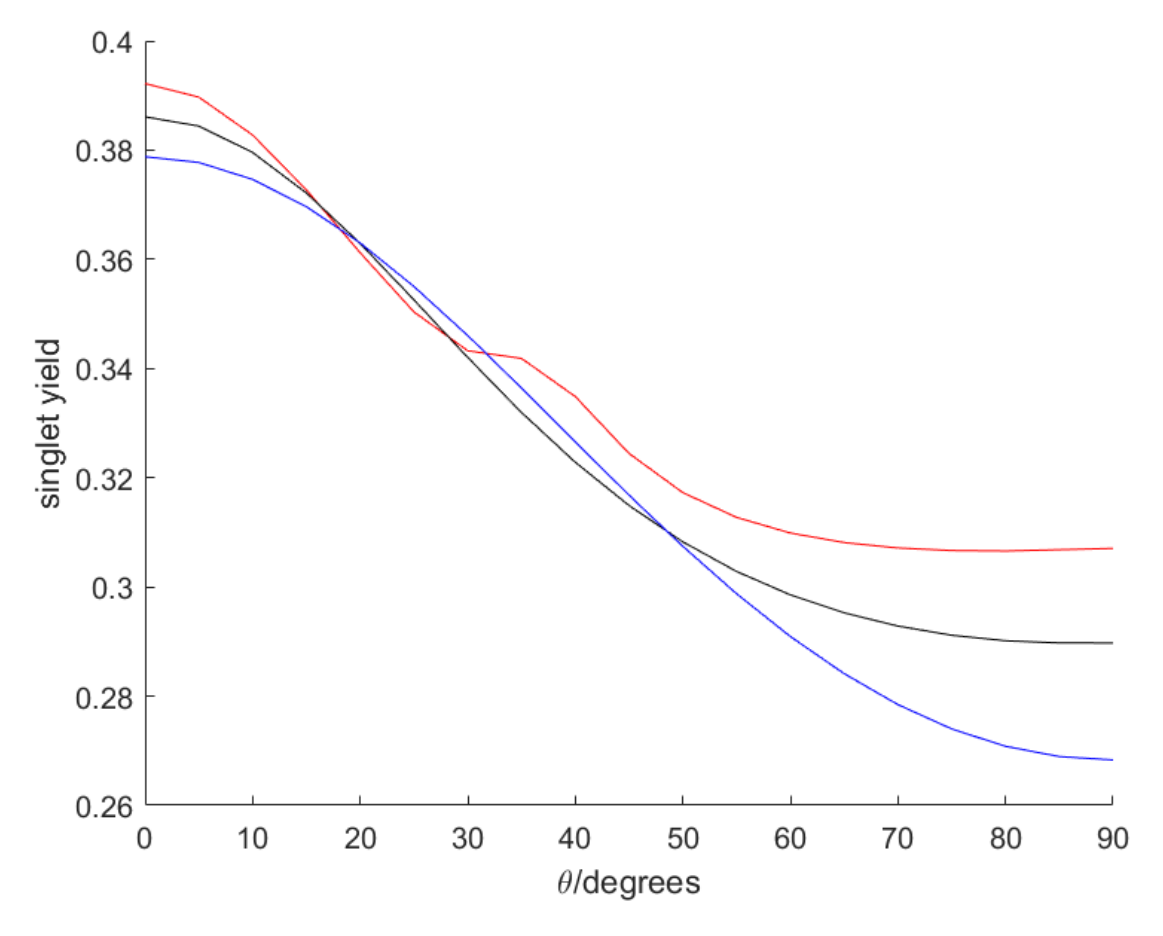


Fig. 3.4: Singlet yield for a static magnetic field $B=B_0(\sin\theta,0,\cos\theta)$. The magnitude of the field used corresponds to the upper and lower bound of the Earth's magnetic field, $B_0=0.25\mathrm{G}$ (blue) and $B_0=0.65\mathrm{G}$ (red), as well as an in between value of $B_0=0.5\mathrm{G}$ (black).

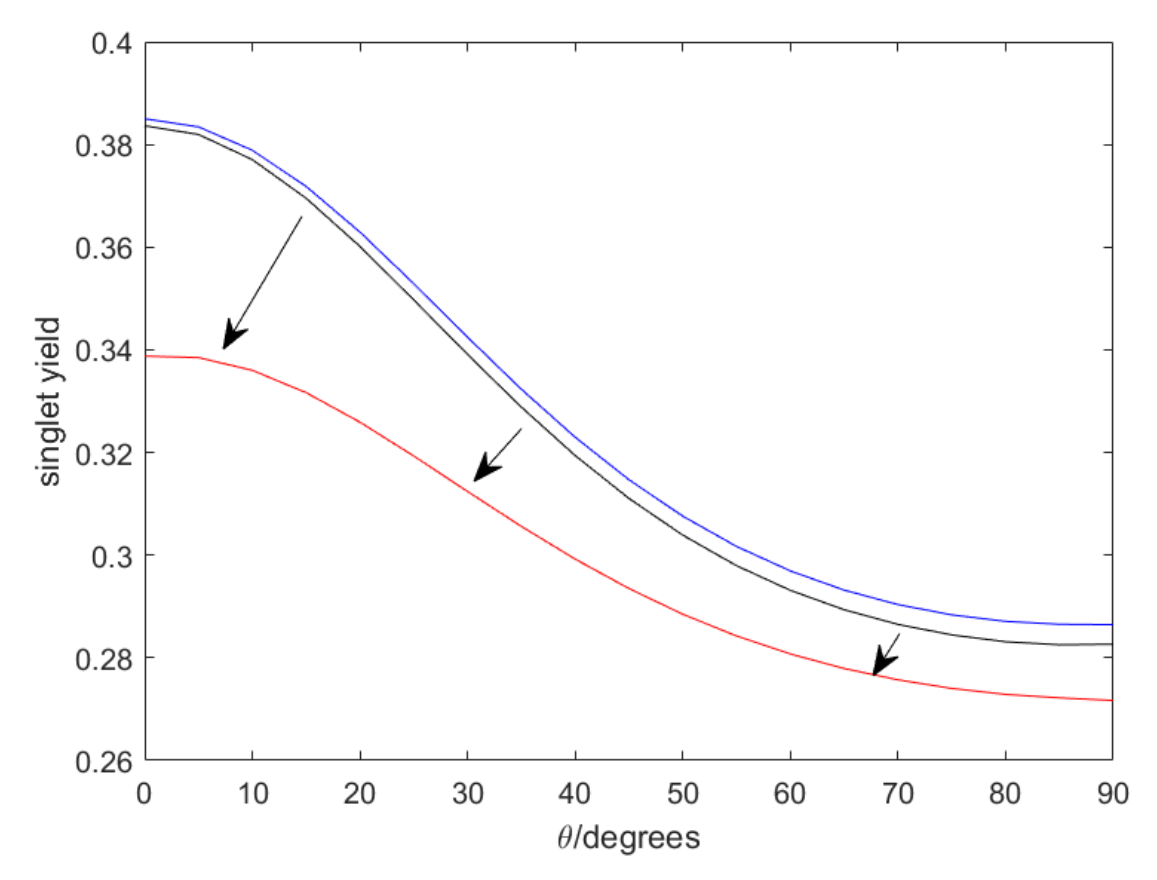


Fig. 3.5: Singlet yield for a static field of $B_0 = 47 \ \mu\text{T}$ with the rate of spin-sensitive chemical reaction $k = 10^6$ (blue) and $k = 10^4$ (black). The singlet yield for $k = 10^4$ and $B_{rf} = 150$ nT is shown in red. The singlet yield is shifted as denoted by the black arrows. The impact of the oscillatory field is more significant for lower values of k.

allowing for disruption or enhancement of magnetic sensing capabilities in animals. No such analogue exists in the magnetite model, which can be used to rule out magnetite based models in certain species. We can introduce an oscillating component in the toy model by adding it to the magnetic field:

$$B' = B_0(\cos\phi\sin\theta, \sin\phi\sin\theta, \cos\theta) + B_{rf}\cos(\omega t)(\cos\varphi\sin\theta, \sin\varphi\cos\theta, \cos\theta), \tag{3.25}$$

with angular frequency ω , magnitude B_{rf} , polar angle φ and azimuthal angle ϑ . Weak oscillating fields of $B_{rf}=5$ nT for garden warblers (Sylvia borin) [114] and $B_{rf}=15$ nT for European robins [27] were observed to disrupt their magnetic sense. Other experiments on European robins with stronger field strengths and varying frequencies were also performed, with similar observations [21,115,116]. To explain this, we simulate the effect of a conservative 150 nT orthogonal oscillating field at the equivalent Larmor frequency of an electron, $f = \frac{eg}{4\pi m}B_0 = 1.4$ MHz. Notably, the impact of the oscillating field is more strongly observed at lower values of k and almost unnoticeable for $k = 10^6$ Hz (see Fig. 3.5).

It should be mentioned that in its current form, the toy model only has very slight variations when an oscillating field is applied, with a shift in the singlet yield of only at most 10.5% with $k = 10^4$ and $B_{rf} = 150$ nT. For an even smaller field of $B_{rf} = 2.5$ nT, like the ones reported in [114] that disrupt garden warblers, the singlet yield would completely overlap with the black curve without an oscillating component. As such, some amplification of the singlet yield is to be expected between the toy model presented and the radical pair mechanism utilised in animals.

3.3 Characteristics of magnetoreception

Having given descriptions of the ferromagnetic and radical-pair mechanisms, we can now highlight some peculiarities in animal magnetoreception observed in the literature and perform educated guesswork on their root causes.

One functional characteristic observed across several species is the emergence of so-called polarity and inclination compasses [19]. Namely, a polarity compass is able to distinguish between the magnetic 'North' and
'South', while an inclination compass uses the inclination of the external field, i.e. the angle between the
field and the horison. This gives rise to a compass that differentiates between equator-ward and pole-ward
instead of discriminating between the north and south. Given that in the magnetite model the magnetic
particles play the role of tiny pole-seeking compasses, animals with inclination compasses are unlikely to
have ferromagnetic-based magnetoreception. Although there do exist models of inclination compasses that
utilize rotation of small pole-seeking needles, see e.g. Ref. [85].

3.4 Summary

In this chapter, we have described the two leading theories for the mechanism of magnetoreception: the magnetite model and the radical pair model. While the models presented in this chapter are rudimentary and overly simplified, they nonetheless highlight the main characteristics of the magnetoreception.

The magnetite model involves alignment of ferromagnets embedded inside an animal, with a balancing act between having large enough ferromagnetic crystals, to overcome thermal fluctuations, but not too large to become energetically unstable to sustain a single-domain magnetisation. Since most biogenic magnetite discovered is similar in composition, this size and shape factor become the most important parameters in deciding the viability of a magnetite compass.

The radical pair model uses a chemical reaction whose kinetics can be altered by an external magnetic field. This occurs because of radical pair intermediate products that contain unpaired electrons, allowing for the non-zero spins to interact with the magnetic field. In this two spin $\frac{1}{2}$ subspace of the unpaired electrons, the reaction proceeds differently depending on whether the electron spins are in the singlet or triplet states.

$_{\tiny 31}$ Chapter 4

Behavioral Experiments on Periplaneta americana

The ability of magnetoreception has been observed in a wide variety of species as previously mentioned in Chapter 1. One likely explanation would be that the emergence of the sense occurred early on in the evolutionary line, before the radiation of phyla [117]. This common origin would explain how very different animals, like birds and cockroaches, have been observed to possess magneto-sensitivity. This would also suggest that such a magnetic sense would share many common attributes of other sensory systems which can generally be broken down into three stages: beginning with an initial detection stage or primary transducer, followed by an amplification step to boost received signals and finally an encoding of the signals for efficient transmission and interpretation [118]. We stress again that the scope of the thesis focuses only on the first stage of detection, and will not cover the biochemistry and neurophysiology of the other two steps.

In this chapter, we describe the magneto-sensitivity behavioral experiments we have performed on *Periplaneta Americana*, American cockroaches, to (i) independently verify observations of the group of Dr. Vacha [23,119–121], as well as to (ii) elucidate other characteristics of magnetic sense in cockroaches. It is important to again bring up the distinction between magnetoreception and the sensory transduction pathways in a magnetic sense. By the nature of behavioural experiments, we may only alter the external stimuli and subsequently record any behavioural changes. This limits our ability to make statements on transduction pathways, without first narrowing down the relevant model for magnetoreception. This chapter is based on the publication titled "Numerical tests of magnetoreception models assisted with behavioral experiments on American cockroaches". Sci Rep 11, 12221 (2021) [122].

$4.1 \quad Periplaneta \ Americana$

Periplaneta Americana, or American cockroaches, are the largest species of the common cockroach. Originally native to Africa, they were introduced, via human activity, to almost all parts of the world with viable tropical climates [123]. Being a tropical creature, it does not have migration tendencies but its evolutionary predecesors, termites, do admit migration and hence cockroaches might have inherited magnetic sense [124].

Periplaneta americana have certain qualities that make it a model organism. Complete sequencing of the cockroach genome [125] opens it up for highly controlled and focused genetic studies. The cockroach's small size and resilience also translates to compact table top experiments without the need for specialised housing or holding areas, simplifying experimental complexity. One key drawback is that the magnetoreception of the american cockroach is not well-established beyond previous works in Refs. [23, 119–121]. To date, the

american cockroach is not known to exhibit any migratory tendencies, which suggests that the magnetic sense, if present, need not necessarily manifest as a directional preference so the usual metric may not be sufficient.

Our experiments expand the study based on Vacha's initial results. The key differences are as follows. The experimental observation time is increased from a period of 10:00h to 14:30h to a 12 hour observation from 06:00h to 18:00h. Additionally, the quantification of cockroach activity is expanded into a quasi-continuous quantity by taking a higher sampling rate (33ms) by using videos as compared to photographs every minute in Vacha's. The experimental outcome agrees with those of the Vacha group, with an additional observation of diminished activity times in a higher field. The main reason for our behavioural experiments is to fit these results with simulations of potential models for magnetoreception and gauge their validity.

Leveraging on computer vision, we utilise tracking algorithms to sift through large amount of video footage.
Furthermore, the time resolution, based on video frame-rate, is high enough to allow side by side real-time
comparisons between runs. We show that this allows to draw convincing conclusions without any human
involvement in the experiment itself and data analysis. We use a metric, activity time, defined as the time
the cockroach spends not at rest. Specifically, that it moved more than a threshold distance or threshold
angle of facing between video frames. The full methods are discussed in the following section. This metric
turns out to be robust and adequately captures information relevant in characterising the magnetic sense.

Additionally, based on the timescales of the field rotations and known parameters of magnetic materials, we present a numerical study in an attempt to reconcile known mechanisms with our observed results.

To avoid behavioral conditioning, randomised permutations of experimental conditions and cockroach specimen were utilised. Since a single experimental run would deprive the cockroach of food and water over a 24 hour period, the same cockroach was not used in consecutive experiments.

884 **4.1.1** Habitat

Adult cockroaches were kept separately in translucent plastic terrariums, placed in an air conditioned room with temperature maintained at about 23.5°C. They were given a diet of grounded cat food pellets. An open-top container of water with a small sponge cut out was present in every terrarium as a water source.

888 4.1.2 Magnetic field conditions

The cockroaches were exposed to a total of 3 different localised magnetic field conditions over the course of the experiments. The first condition was the control, which was just the ambient geomagnetic field,

$$\mathbf{B}_{earth} = (B_H, \theta, B_V), \tag{4.1}$$

where we have used a cylindrical coordinate system to describe the field, with B_H and B_V as the horizontal and vertical components of the geomagnetic field respectively, and θ as the azimuthal angle with the reference direction chosen to be the Earth's magnetic north (see Fig. 4.1).

The other 2 conditions were test conditions which we refer to as the Rotated Earth Strength Field (RESF) and the 5 G tests involving roughly 15 times larger in magnitude field as compared to the Earth's field. Both tests involved alternating every 5 minutes between the ambient geomagnetic field, \mathbf{B}_{earth} , and a modified field, achieved by automated switching of the power supply of the coils. When the power supply was switched on, θ was shifted 60° clockwise for the RESF test condition. In the 5 G test, θ was shifted 56.6° clockwise and B_H was increased to 5.18 G. In cylindrical coordinates, the modified field for the RESF is

$$\mathbf{B}_{RESF} = (B_H, \theta + 60^\circ, B_V), \tag{4.2}$$

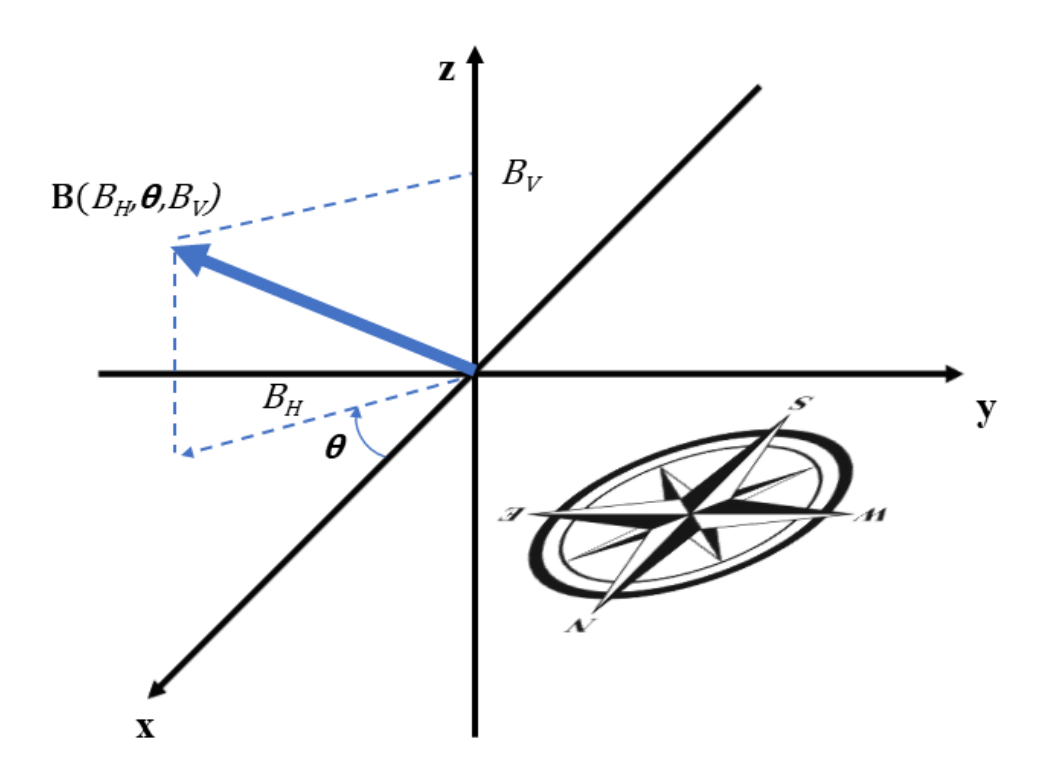


Fig. 4.1: Coordinate system used to describe the magnetic field. The magnetic north is taken to be the direction where $\theta = 0^{\circ}$, with B_H and B_V being the projections on the xy-plane and z-axis respectively.

900 and

$$\mathbf{B}_{5G} = (5.18G, \theta + 56.6^{\circ}, B_V), \tag{4.3}$$

for the 5 G tests. Over the course of the experiments, there were variations in the local geomagnetic field, with the average measured to be

$$\mathbf{B}_{earth}^{ave} = (0.35G, 0^{\circ}, 0.25G). \tag{4.4}$$

As such, the values of B_H in the RESF are not fixed but made to match the geomagnetic field measured prior to commencement of the experimental run. B_V is unchanged in all conditions as there are no contributions from the coils along the vertical axis.

To realise the test conditions, two Merritt coil systems were used to generate the modified fields [126]. These are particular configurations of square coils to generate a region of uniform magnetic field around the axis of the coil (see Fig 4.2). Specifically, the four square coil configuration was utilised, with the length of the square, d, and the distance of the inner pair of coils from the center, a, having the ratio of

$$a/d = 0.128, (4.5)$$

and for the outer coils, the ratio of the distance from the center, b, to d is,

$$b/d = 0.505 (4.6)$$

Lastly, the ratio of the number of turns in the inner coil, N_a , to the number in the outer coil, N_b , was,

$$N_a/N_b = 0.423 (4.7)$$

To realise the RESF condition we used the Merritt coil of d=1.2m positioned such that its main axis

was oriented 120° clockwise from the horizontal component of the magnetic north. We then tune the input current so that the magnetic field generated by the coils,

$$\mathbf{B}_{coil}^{RESF} = (B_H, 120^{\circ}, 0), \tag{4.8}$$

together with the ambient geomagnetic field gives 60° rotation of the magnetic north. For the 5 G test condition we used a smaller Merritt coil of d = 0.3 m positioned with its axis oriented 60° clockwise from the magnetic north so that,

$$\mathbf{B}_{coil}^{5G} = (5, 60^{\circ}, 0), \tag{4.9}$$

with the net effect being a magnetic field approximately 15 times larger than the geomagnetic field, rotated 56.6° clockwise from the magnetic north, see Fig. 4.2 for illustration.

20 4.1.3 Experimental Procedures

A single run of the experiment takes over a period of 24 hours in an isolated room, starting at 6pm on day 1. Upon commencement, a single cockroach is moved onto a Petri dish of 15 cm diameter. Cockroaches were immobilised by placing the insectarium in a 4° C environment to allow for easier transference. To minimise any visual cues from the surroundings, the Petri dishes were placed in a box with its inner surfaces lined with white paper. Cutouts on two opposite sides were made and covered with translucent film to allow for uniform illumination inside a box. For illumination, 2 x 600 lumen, 10 W LED bulbs (IKEA LED1424G10), were positioned at each cutout. Additionally, a white slip was secured along the Petri dish circumference to further limit the cockroach's vision. A small aperture was made in the top of the box for a camera to capture the cockroach and its movements in the Petri dish at 30 frames per second. The box was placed on top of a stage so that the Petri dish rests in the middle of the Merritt coil (for the uniform magnetic field).

The ambient geomagnetic field was measured using a Honeywell HMR2300 smart digital magnetometer for calibrating the RESF. The room was then sealed and undisturbed for 24 hours, with the lighting and coils set on timers for 6am the next day.

$_{\scriptscriptstyle{334}}$ 4.2 Results

921

923

924

926

927

928

929

930

Video recordings over the 12 hour period, from 6am to 6pm, were processed using self-written tracking software (C++). The program first identified the cockroach against the white background and fitted an 936 ellipse over its body on every video frame. The timestamp of each frame, coordinates of the ellipse (in pixels) and angle of the main axis was stored in a textfile. A quantity "activity time" was computed by 938 summing up the time intervals between frames (33.3 ms) over which the cockroach moved more than 3 mm or rotated its axis by more than 8 degrees. These thresholds are arbitrarily chosen but different values do not 940 significantly alter the results. The accumulated activity time of a cockroach over a period can be thought of 941 as the time the cockroach spends in motion during the period. Two particular periods of interest would be 942 5 minutes, corresponding to the switching times of the fields in the RESF and 5 G test conditions, as well as 12 hours for the duration of the whole altered fields. These two plots are shown in the main body and 944 inset of Fig. 4.3.

$_{946}$ 4.2.1 Discussion

Regardless of magnetic condition applied, activity times tend to be low, with the mean over 12 hours being at most around 100 seconds, indicating that cockroaches tend to be stationary for most of the day. This is not unexpected, given that cockroaches are nocturnal. Furthermore, their movements tend to be sporadic and in short bursts, as seen from the spikes in the main plot. The overall trend observed is a general



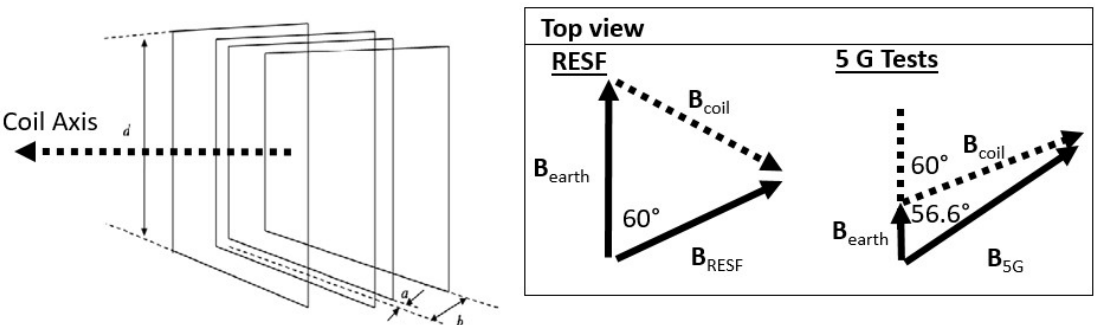


Fig. 4.2: Top: Experimental setup used for the cockroach behavioral experiments. The cockroaches were placed in the brown box at the center of the stage over the duration of experiments. The large square Merritt coils were used to generate the RESF magnetic field test conditions. Bottom left: The square Merritt coils produce a homogenous field in a region along the coil axis that uniformly covers the Petri dish with the specimen. Bottom right: The RESF and 5G test conditions were magnetic fields that were switching between the geomagnetic field and a modified field every 5 minutes. These modified fields were generated by coils oriented such that, when turned on, the resultant fields, $B_{earth} + B_{coil}$, are an equivalent Earth field (RESF) or a stronger field approximately 5 G (5 G tests) rotated 60° clockwise.

952

953

954

955

956

957

958

964

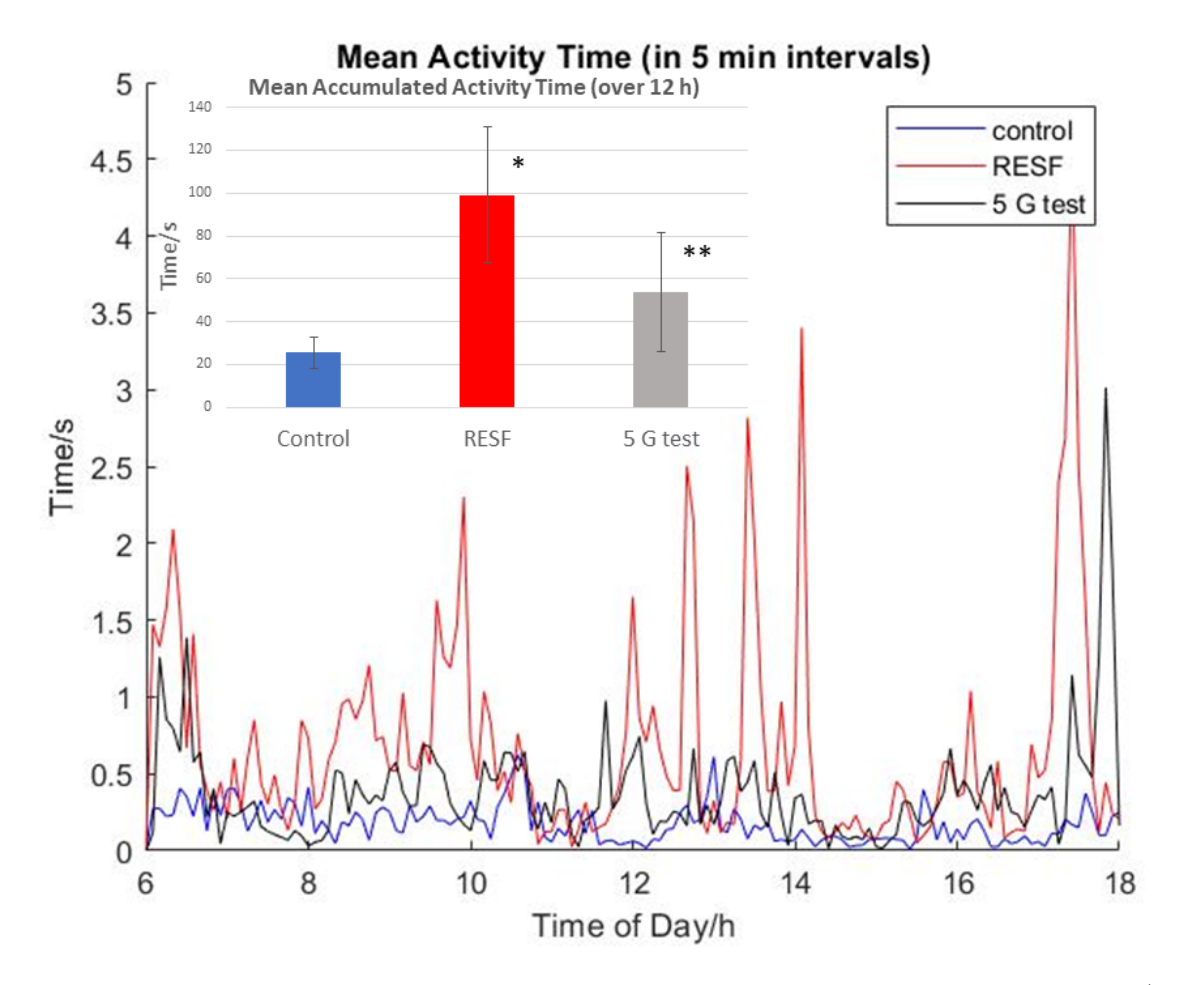


Fig. 4.3: In the main plot: Mean activity time over 5 minute intervals of the American cockroaches (N=29 for controls and RESF, N=16 for 5 G tests), calculated by summing up the time the cockroach spends translating or rotating, averaged over all measurements. In the inset: Mean activity time over the full 12 hour duration. Error bar shown is the standard error of the mean. P-values using the t-test are indicated with * for significant (p-value; 0.05) and ** for not significant.

increase in activity time in the RESF as compared to the control runs, with the effect diminished in the 5 G test conditions. Since the statistics compared are the sample means, these are approximately normally distributed by the central limit theorem. Together with the randomised permutation of the trials, and that the cockroaches were always isolated from each other, the activity times are independent of one another. As such, we can use the t-test to compare whether the activity times under the test or control fields have different means. Using the t-test on the mean accumulated activity times, the p-values were found to be significant between the controls and RESF (p-value = 0.028) but insignificant between the 5 G tests and controls (p-value = 0.222). Specifically, the t-test compares the sample means of the activity time under the test and control fields, assuming they have similar variances.

The results for the RESF confirm similar observations made by the group of Dr. Martin Vacha in Masaryk 960 University [119], although it should also be noted that the geomagnetic fields ($B_H = 0.17G$, $\theta = 28^{\circ}$) in 961 their experiments are different due to the different geographical locations. 962

Additionally, the activity time in 5 minute intervals in Fig. 4.3 appears periodic. Together with the switching 963 time, one wonders if the periodic switching time has a direct consequence on the magnetic induced restlessness. Fig. 4.4 shows the Fourier spectrum of the mean activity time without any integration time, with the 965

970

971

972

973

975

977

978

979

981

982

983

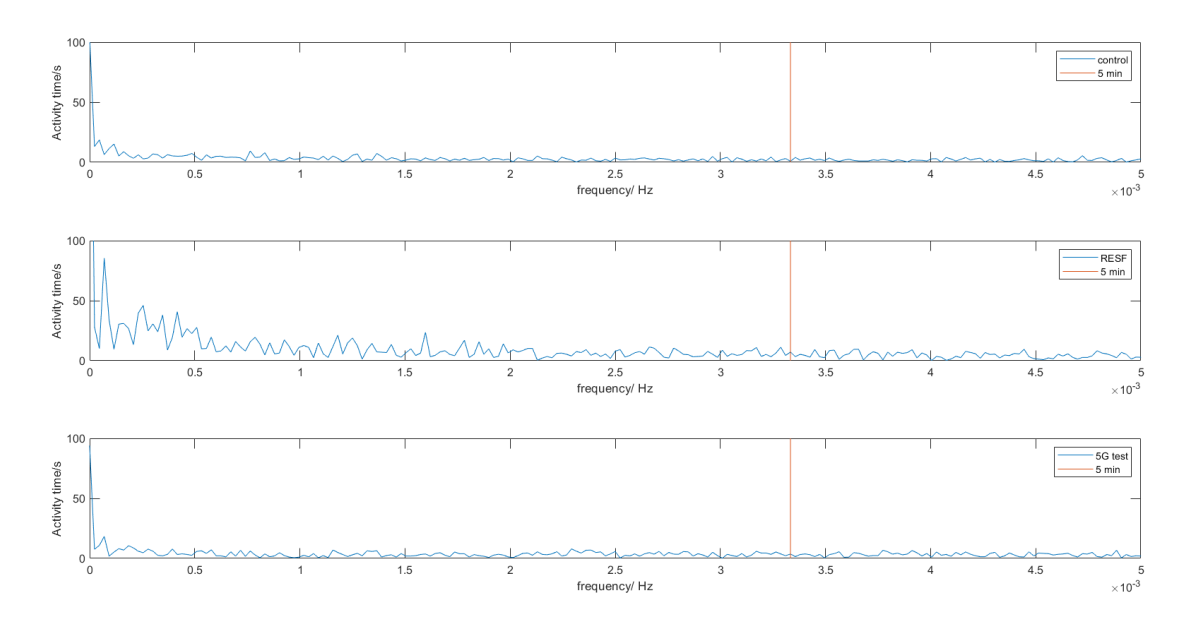


Fig. 4.4: Fourier spectra of the activity time without any integration period in the control (top), RESF (middle) and 5 G test fields (bottom). The red vertical line corresponds to the 5 minute switching frequency.

vertical red lines corresponding to the 5 minute frequency. There is no significant amplitude in the activity times corresponding to the switching frequencies. As such, the perceived periodicity in Fig. 4.3 is just an artifact of the integration period, unrelated to the switching times.

Our observations in the 5 G test condition strongly suggest that the magnetic sensing mechanism is attuned around the Earth's field, with its function inhibited in larger magnetic fields of at least 5 G. This is similar to the results obtained with birds [28] and again indicates that their sensing mechanisms share functional characteristics. In the following sections, we apply the ferromagnetic-based models and radical pair models as discussed in the previous chapter to attempt to reconcile them with our observations.

974 4.2.2 Ferromagnetic-based models

Before presenting a ferromagnetic-based compass model in the American cockroach, it is worthwhile to examine magnetic deposits discovered within the American cockroach and similar species in the literature. Magnetic deposits in live American cockroaches have been detected by atomic magnetometers [124], which were estimated, by modeling the residual magnetization of spherical grains, to have radii around 10-100 nm and sit in a highly viscous medium with viscosity $\eta=10^5$ Pa sec. Biogenic magnetite about 10-20nm has also been found in certain termite species [127, 128], which are closely related to cockroaches within the same order of Blattodea [129]. Furthermore, transmission electron microscopy of the magnetic extracts from termites display uniformity in both size (10 nm diameter) and shape (hexagonal/cubic), suggesting biogenic origin. Though below the size thresholds for SD grains, clustering and interactions would allow for these smaller grains to behave as SD.

Fitting to Ferromagnetic-based models

As our starting point, we assume that the magnetic deposits in the American cockroach are identical rigid SD magnetite or greigite with saturation magnetisation of about $M_s = 3 \times 10^5$ A/m. The efficacy of the

991

993

995

996

997

999

1000

1001

1002

1003

1004

1005

1007

1008

1009

magnetite compass depends on the "alignment" of all magnetite grains, which we define as

$$M = \frac{\sum_{i=1}^{n} \mathbf{m}_{i}}{n|m|},\tag{4.10}$$

where n is the number of grains and the i-th grain has magnetic moment \mathbf{m}_i , each with magnitude m. Since our magnetic conditions never change the vertical component of the magnetic field and the cockroach motions are restricted to the horizontal plane by the Petri dish, we constrain our model to the horizontal plane. The individual moments \mathbf{m}_i can be thought of as points on the circumference of a circle with radius |m|, and the alignment, M, takes on values from 0 to 1 depending on how aligned or closely clustered these points are on the circle. The orientation of the magnetic moments depends only on an alignment angle ϕ_i where we define the reference direction ($\phi = 0$) to be the geomagnetic north. The alignment angle is governed by Newton's law, experiencing a restoring force from the local magnetic field and an opposing frictional force due to the highly viscous environment. The equation of motion for the i-th grain is then

$$I\ddot{\theta_i} = -f\dot{\theta_i} - mB\sin\theta_i,\tag{4.11}$$

where θ_i is the angle between the external field and ϕ_i , I is the moment of inertia of the grain and f is the rotational friction coefficient. We take the grains to be structure-less spheres so that $I = \frac{2}{5}\rho V R^2$ and $f = 8\pi \eta R_h^3$. For spherical geometries, the hydrodynamic radius, R_h , is interchangeable with R. We take R = 50 nm, somewhere in the midpoint for the estimated radius by Kong et al. [124], and initialise ϕ_i for n = 36 magnetite grains to be uniformly distributed over the range (0,360] so that $\theta_i \in \{10^\circ, 20^\circ, ..., 360^\circ\}$. This initialisation serves two purposes. Firstly, this initial configuration would satisfy the observation that cockroaches do not produce any detectable magnetic field if not magnetised prior [124]. Secondly, it allows us to explore the dynamics over the whole space of ϕ .

Alignment in RESF 1006

To account for geographical variations of the geomagnetic field, we take an exaggerated estimate for the horizontal component of the geomagnetic field 0.5 G. This value is not entirely unrealistic, given local field fluctuations in magnitude and inclination. For the controls, we thus have that

$$B_{control} = 0.5G, (4.12)$$

$$\theta_i^{control} = \phi_i. \tag{4.13}$$

In the RESF and 5 G tests, due to switching nature of the local magnetic field, we additionally require discontinuous jumps of θ_i between each 5 minute interval. For the RESF,

$$B_{RESF} = 0.5G, (4.14)$$

$$\theta_i^{RESF} = \begin{cases} \phi_i, & \text{for } 0 \le t < 5, 10 \le t < 15, \dots \\ \phi_i - 60^{\circ}, & \text{for } 5 \le t < 10, 15 \le t < 20, \dots \end{cases}$$

$$(4.15)$$

and for the 5 G tests, there are also discontinuous jumps in the field strength,

$$B_{5G} = \begin{cases} 0.5G, & \text{for } 0 \le t < 5, 10 \le t < 15, \dots \\ 5G, & \text{for } 5 \le t < 10, 15 \le t < 20, \dots \end{cases}$$

$$(4.16)$$

$$B_{5G} = \begin{cases} 0.5G, & \text{for } 0 \le t < 5, 10 \le t < 15, \dots \\ 5G, & \text{for } 5 \le t < 10, 15 \le t < 20, \dots \end{cases}$$

$$\theta_i^{5G} = \begin{cases} \phi_i, & \text{for } 0 \le t < 5, 10 \le t < 15, \dots \\ \phi_i - 60^\circ, & \text{for } 5 \le t < 10, 15 \le t < 20, \dots \end{cases}$$

$$(4.16)$$

Numerical simulations of the alignment in the different \vec{B} field conditions show that field strengths of 0.5 G are generally too weak to generate significant alignment, with only 40% alignment of the magnetites achieved over the full 12 hour exposure (see Fig. 4.5).

Additionally, we can consider whether the motion of the cockroach is an attempt to maintain a certain preferred alignment. Using the measured angle of the insect in the jth frame, θ_j^{exp} , we modify the angle of the magnetic grain at times $t_j = j\Delta t$, where Δt is the time duration between the frames, by adding to them the cockroach motion, i.e. $\theta_j \to \theta_j + \theta_j^{\text{exp}}$. This does not lead to improved alignment and instead impedes it, with M staying below 0.05 in the RESF. This holds for both control and test experiments, again in disagreement with experimental finding that cockroaches behave differently in these two conditions.

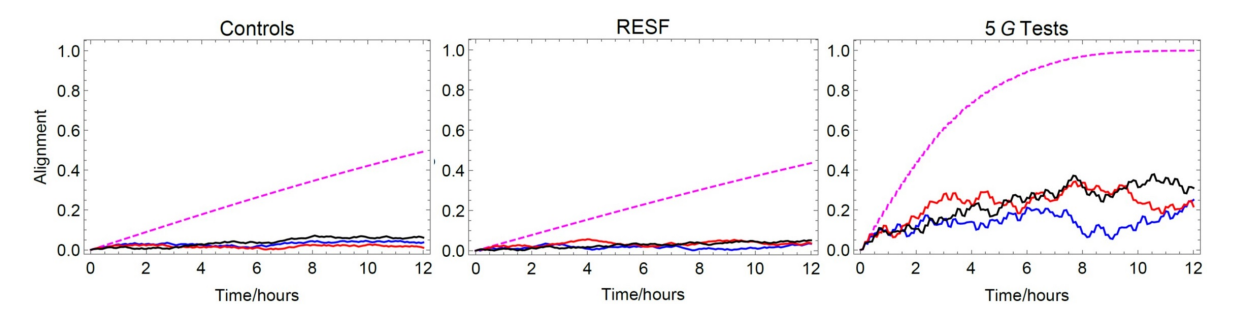


Fig. 4.5: Alignment, as defined in Eq. 4.10, as a function of time elapsed for a magnetite grain of radius 50 nm in a viscosity of 10^5 Pa s. The solid lines include motion from three typical cockroaches while the dashed line is independent of cockroach motion. The magnetic field strengths of the controls and RESF are not strong enough to produce appreciable alignment over the duration of the experiment.

To understand in further detail the dynamics of the magnetite grains, we show angular histograms of the alignment angles ϕ during intermediate time points at 3, 6, 9 and 12 hours in Fig. 4.6. The magnetic grains align toward different directions in all 3 conditions. In the controls, the grains orient themselves towards the geomagnetic north ($\phi = 0$), while they orient towards the midpoint between the rotated north and geomagnetic north ($\phi = 30^{\circ}$) in the RESF, and somewhere close to rotated north ($\phi = 50^{\circ}$) in the 5 G test. Other than the different equilibrium orientations, the controls and RESF share fairly similar characteristics in the dynamics. This suggests that the timescales for alignment in 0.5 G fields are much longer than the switching time of 5 minutes so that the grains effectively experience a time-averaged field. Rod shaped magnetites are also often found in certain species. Assuming a rod of length l = 150 nm and diameter d = 107 nm, we modify the moment of inertia, I, to that of a rod rotating along its center $I = \frac{1}{12}ml^2$ and the rotational friction to that of an ellipsoid with semi-major axis l and semi-minor axis l and semi-minor axis l and semi-minor axis l and grains. This is understandable given that the leading terms in l and l are the "size" terms (length for rods and radius for spheres).

Discussion

Our model shows that the weak geomagnetic field cannot meaningfully align magnetite particles within a highly viscous media that is expected of the internal environment of a cockroach. In fact, there is no discernible difference between the alignment in the controls and the RESF from Fig. 4.5, nor are there features that might hint at the discontinuous switching of the magnetic field (spikes or abrupt changes). This means that the timescales of a magnetite-based magnetic sense are not responsive enough to perceive the RESF. Looking at the angular histograms (Fig. 4.6 and 4.7), it is apparent that the RESF effectively behaves like an aligning field that is the average of the geomagnetic north and the rotated north, i.e. geomagnetic field rotated 30° clockwise, regardless of the geometry of the magnetite. Our model shows that a magnetite-based magnetic sense cannot explain observed increase in activity time in the RESF as compared to the control magnetic field.

Additionally, our version of the magnetite model is also incompatible with the observation of a diminished sensitivity in a stronger aligning field. Due to the form of the equation of motion (Eq. 4.11), the only way a diminishing effect can manifest is for an additional frictional term to scale with the magnetic field. Unless

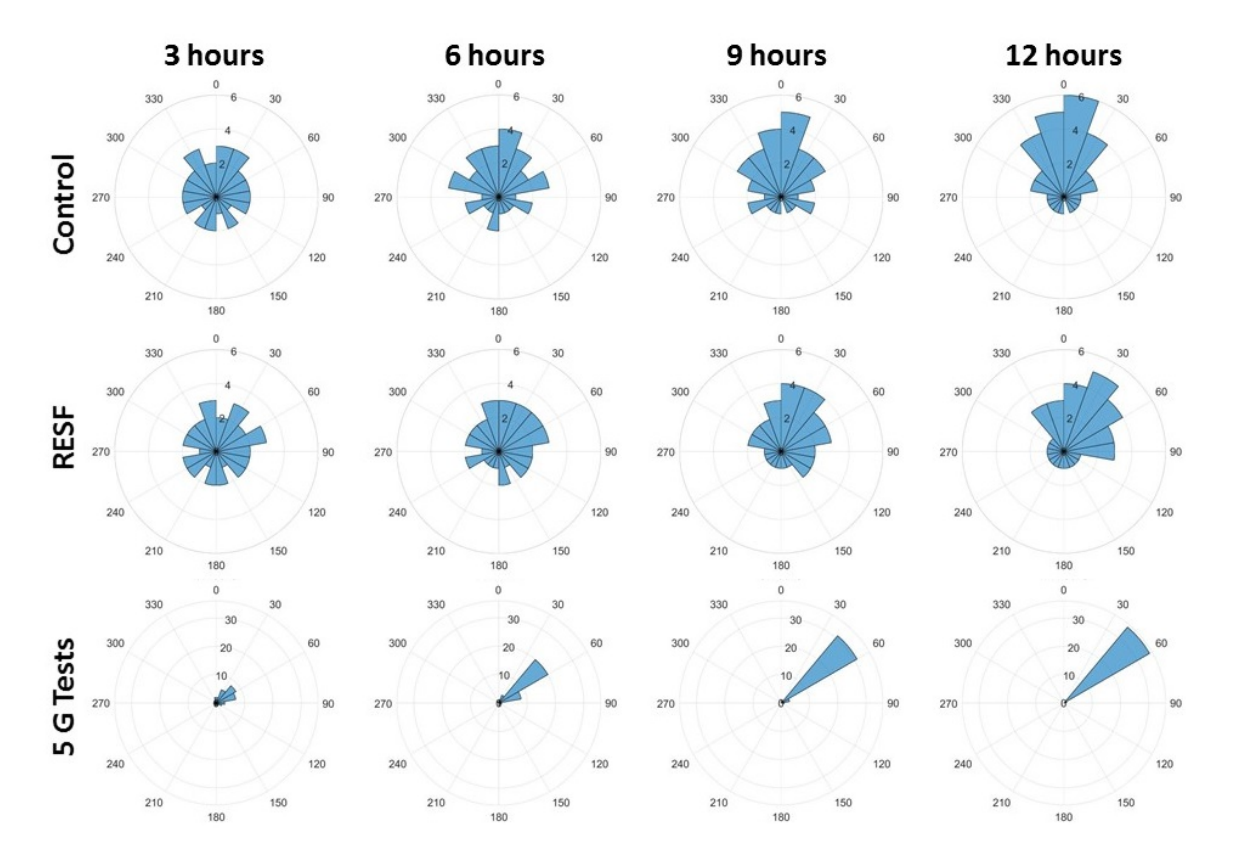


Fig. 4.6: Angular histograms of the alignment angle, ϕ , of 36 spherical magnetite grains of radius R=50 nm. A total of 36 non-interacting grains were simulated, each starting with a different value of ϕ from $10^{\circ}, 20^{\circ}, ..., 360^{\circ}$ at t=0 hr, governed by the dynamics described in Eq. 4.11 under 3 different magnetic conditions: control (upper row), RESF (middle row) and 5 G test (lower row) fields. The values of ϕ were then plotted as an angular histogram (bin size is 20°) at t=3, 6, 9 and 12 hours. The grains in the control and RESF fields only partially align by the 12 hour time point and align to 0° (geomagnetic north) and 30° (midpoint of geomagnetic and rotated field) respectively. In contrast, the grains in 5 G fields orient toward the rotated field and show good alignment, with all grains having $40^{\circ} \le \phi \le 60^{\circ}$ at t=12 hours. Note that in using the same radial scale (representing the frequency of occurrence) over the last row, the bars at t=3 and 6 hours are obscured.

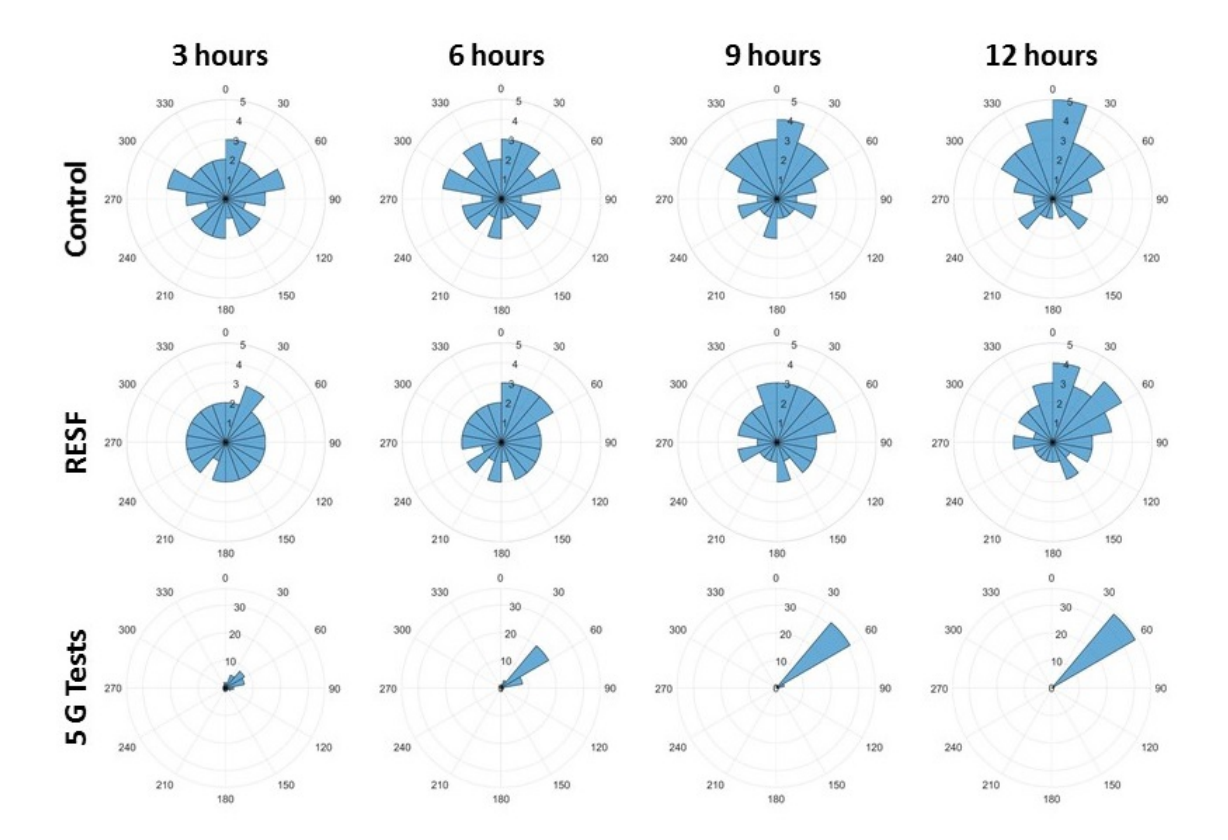


Fig. 4.7: Angular histograms of the alignment angle, ϕ , of 36 magnetite rods (l = 150 nm, d = 107 nm). The dynamics of the rods are qualitatively the same as those of the spherical grains.

complex structures of magnetite or greigite are discovered that would possess this scaling frictional property, we can further generalise that models utilising the physical motion of a magnetic particle in the presence of an external magnetic field will align more effectively in a stronger field.

Taken in totality, both the increased activity in the RESF and the diminished magnetic sense in the 5 G field suggest that the magnetic sense in the cockroach is unlikely to be magnetite-based.

4.2.3 Fitting to the Radical pair models

The Cryptochrome / Photolyase flavoprotein family have been found to be light and magnetically sensitive [90]. Following the work by Solov'yov et al. [131] on radical pair creation and subsequent dynamics in Crytochrome-1 (Cry-1) of the plant *Arabidopsis thaliana*, we move from the toy model discussed in the previous chapter to the one with more realistic parameters.

Crytochrome-2 was found, and even shown via gene silencing to mediate magnetoreception, directly below the retina of *P. americana* [121]. Similarly, Crytochrome-1a was also found in the retinal cones of *Erithacus rubecula* (European robins) and domestic chickens [132], and later in pigeons, Blackcaps, *Sylvia atricapilla*, and Zebra Finches [133]. Interestingly, some of these birds, like the cockroach, are also non-migratory, hinting at a vestigial trait. In the model that follows, we will utilise the geometry (i.e. hyperfine axes) of Cryptochrome-1 (Cry-1) from the plant *Arabidopsis thaliana* [134] and transition rates of Photolyase to various intermediate states in *Escherichia coli* [135, 136]. While Cry-1 is absent in *P. americana*, the radical pair mechanism is mostly localised within the highly conserved FAD molecular domain [137] in Cryptochrome-Photolyase family.

In this model, FAD in cryptochrome goes through a series of interactions with a nearby Tryptophan triad chain before ending up as FADH. The role of an external magnetic field is to disrupt this forward reaction by modulating a back-transfer reaction to FAD. Our following discussions are based on Cryptochrome-1 from A. thaliana.

Starting with FAD absorbing blue light, an excited neutral radical FAD* is formed. This is supported by UV/vis spectroscopy on in-vitro Arabidopsis thaliana cryptochrome 1 that displayed absorption bands centered around 444 and 370 nm, and a different spectra, consistent with the neutral flavoprotein radical of Cry1, was observed after illumination with blue light [138–140]. The radical is protonated to form FADH+, inferred from the FTIR difference spectrum showing deprotonation of either aspartic or glutamic acid. The most likely candidate is D396, from the crystal structure of the Cry1 PHR domain, that is 3.8 Å from the flavin site. Interestingly, N378 asparagine, the amino acid counterpart of D396 in E. coli photolyase, similarly facilitates the stabilisation of the protonated radical in E. coli photolyase [141]. Due to the vicinity of the Tryptophan triad chain (Trp-400, Trp-377 and Trp-324), a sequence of electron jumps occur starting with the nearest Trp-400 to form the first radical pair FADH+ Trp-400 \rightarrow FADH+ Trp-400+, then from Trp-377 to Trp-400, forming the second radical pair FADH+ Trp-377+ and finally FADH+ Trp-324+. The last radical pair is eventually deprotonated with the net effect of the sequence of reactions bringing FAD to the signalling state FADH.

The forward reaction described thus far has no magnetic field dependence. The key feature of the radical pair mechanism arises from a back-transfer reaction involving the radical pair chain, hence its namesake. The unpaired electrons (one in FADH and another in the protonated Tryptophan) form a two spin-1/2 particle subsystem. Due to the different hyperfine interactions each electron experiences, the electron pair evolves between the singlet and triplet states. Recombination is selective only to the singlet states. The reaction scheme described thus far is summarised in Fig. 4.8.

1086 Hamiltonian

The Hamiltonian for the dynamics of the electron pair is given by a sum of the Zeeman interaction term and the hyperfine interactions of each pair with their corresponding "nuclei",

$$H_{j} = g\mu_{B}\vec{B}\cdot\vec{S}_{j} + \mu_{B}\sum_{i}\vec{I}_{i}\cdot(\overleftrightarrow{A}_{ij}^{\text{iso}} + \overleftrightarrow{A}_{ij}^{\text{aniso}})\cdot\vec{S}_{j}, \tag{4.18}$$

where g is the gyromagnetic ratio, which we take to be 2 for the electrons, μ_B the Bohr magneton, \vec{S} the spin operators, \vec{A}^{iso} and \vec{A}^{aniso} are the isotropic and anisotropic hyperfine tensors. The subscripts j=1,2 refer to each of the electron in the pair while i indexes the relevant nuclei of each electron. The radical pairs sit inside a larger photolyase, which due to its size and mass has a fixed molecular axis that we take as the reference ($\theta = 0$ and $\phi = 0$). The animal then obtains its bearings based on the difference between this molecular reference axis and the geomagnetic field.

Ultimately, as already mentioned in the RPM toy model, it is the anisotropy of the effective field experienced by each radical that enables directional information to be extracted by the overall chemical reaction.
This is not to be confused with the anisotropic component of the hyperfine tensors. Both the isotropic
and anisotropic components contribute to the effective field each radical experiences. As such, the second
summation term in Eq. 4.18 is crucial for the RPM.

Myperfine Tensors

The full list of nuclei in the protein sequence would be too large of a computational cost, so only nuclei with the strongest hyperfine coupling are considered. The hyperfine tensors for electrons 1 and 2 used in the simulations are given in Table 4.1. They were measured via Electron Paramagnetic Resonance (EPR)

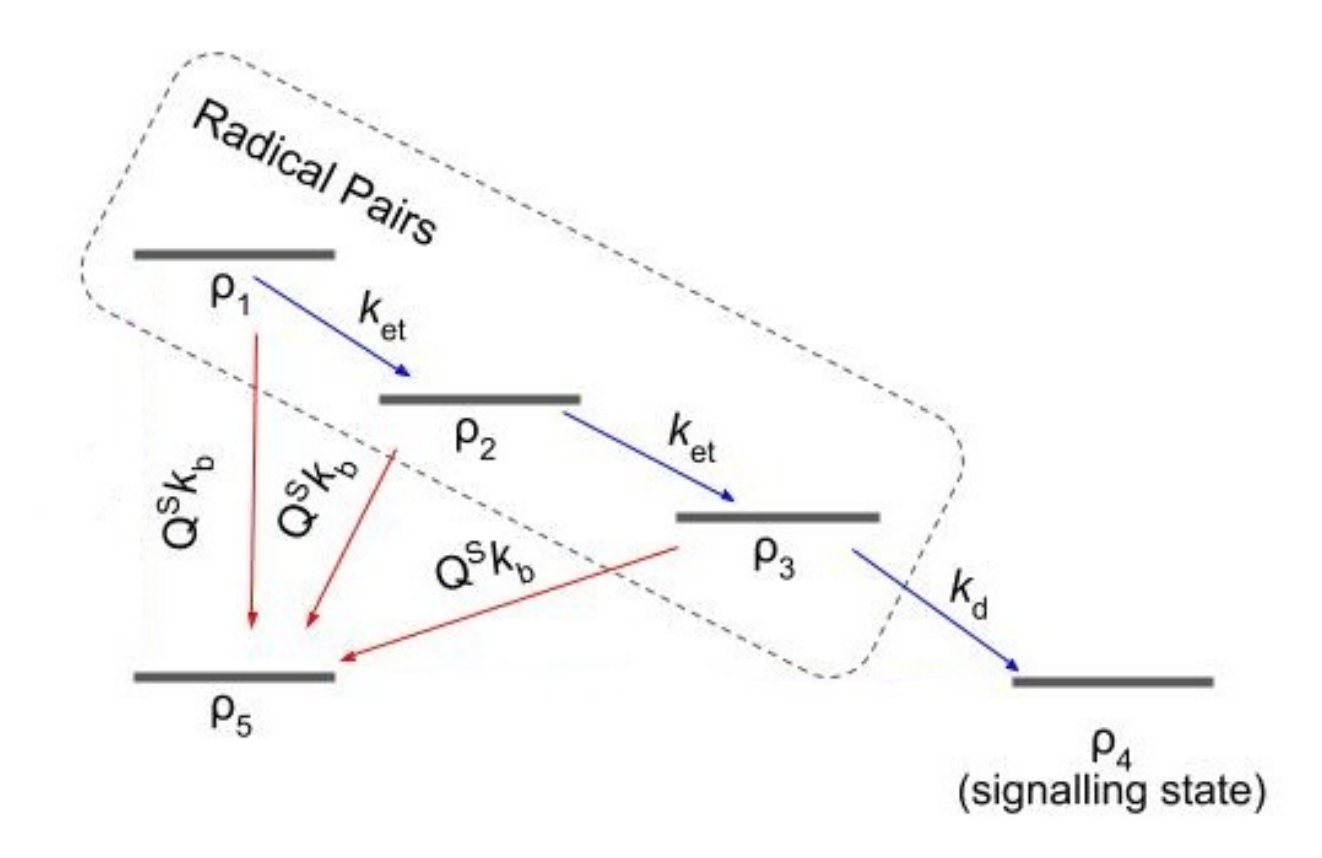


Fig. 4.8: Reaction scheme for FAD undergoing a radical pair reaction. The reaction outcomes, FADH (ρ_4) and FAD (ρ_5), can be modulated by an external magnetic field due to the spin-selective nature of the recombination step represented by the red arrows. The magnetically sensitive steps are shown in the dashed box while the blue lines represent incoherent classical decay channels.

and Electron Nuclear Double Resonance (ENDOR) spectroscopy [134, 142–144]. These are nuclei in close proximity to the site of the unpaired electrons with large hyperfine tensor values, which translate to nuclei which would interact most strongly.

Electron 1 interacts with N_5				
$A_{11}^{\mathrm{iso}} [\mathrm{G}]$	$A_{11}^{\mathrm{aniso}} [\mathrm{G}]$	hyperfine axes		
3.93	-4.98	0.4380	0.8655	-0.2432
	-4.92	0.8981	-0.4097	0.1595
	9.89	-0.0384	0.2883	0.9568
Electron 2 interacts with H_5 and H_1^{β}				
$A_{12}^{\mathrm{iso}} [\mathrm{G}]$	A_{12}^{aniso} [G]	hyperfine axes		
13.6	0	1	0	0
	0	0	1	0
	0	0	0	1
A_{22}^{iso} [G]	A_{22}^{aniso} [G]	hyperfine axes		
-4	-2.3	-0.984	0.180	0
	3.5	0.180	0.984	0
	-1.2	0	0	1

Table 4.1: Hyperfine tensors for nuclei interacting with electrons 1 and 2.

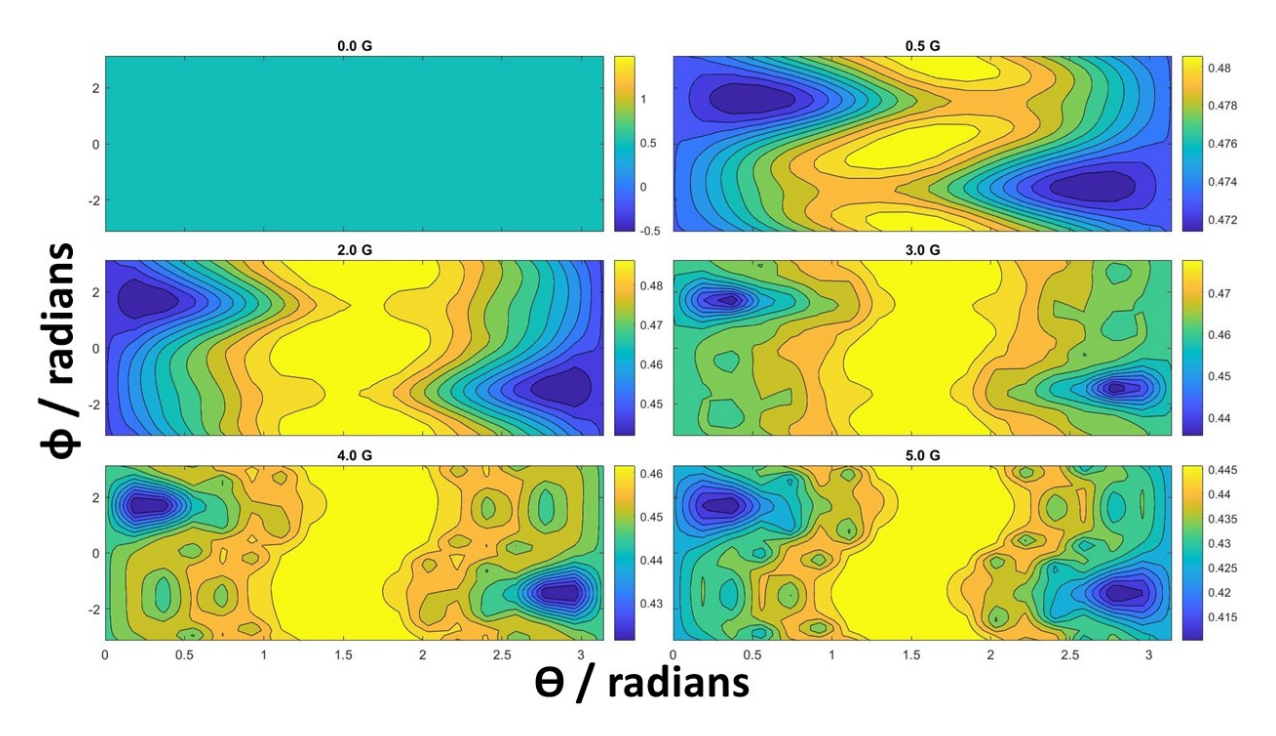


Fig. 4.9: Contour plots of the signal yield as a function of θ and ϕ in the presence of different aligning field strengths. The chemical dynamics follows the reaction scheme shown in Fig. 4.8, with each point on the plots representing the steady state population of the signalling state, ρ_4 . The decay parameters used were $k_b = 10^7$ Hz, $k_{et} = 10^8$ Hz and $k_d = 3.3 \times 10^6$ Hz.

These values are significantly more complex than those presented in the toy model. Namely, electron 1 only interacts with a single highly anisotropic N_5 nucleus while electron 2 interacts with two weakly anisotropic H_5 and H_1^{β} nuclei.

1110 Signal Yield

Setting the transition rates $k_b = 10^7$ Hz, $k_{et} = 10^8$ Hz and $k_d = 3.3 \times 10^6$ Hz, which were estimated from various experimental findings in [131], we can simulate the effect of different aligning field strengths and angular orientations on the signalling state. The angular coordinates here are the relative angles of the aligning field with respect to the molecular axis of the Cryptochrome nuclei, assumed to be locked in place in the cockroach retinal cones. From Fig. 4.8 and by noting that $k_{et} > k_b > k_d$, we can see that the population in ρ_3 is the bottleneck in the reaction dynamics and the reaction reaches the steady state once ρ_3 is zero. As such, we simulate the accumulated population of the signalling state ρ_4 after enough time to arrive at a steady state. We call this steady state population the signal yield, and we plot this as a function of the angular orientation in Fig. 4.9.

From Table 4.1, we see that the strongest coupling is given by the almost 10 G value along the axis given in the third row for N_5 . This axis roughly corresponds to $\theta=0.3$ rad and $\phi=1.4$ rad which we observe to be the global minima and unifying feature regardless of the strength of the field. Overall, due to the varying anisotropies of all the nuclei, the singlet yield is highly non-trivial. The signal yield varies in a small window (between 0.472 to 0.48) at 0.5 G compared to a larger window (between 0.415 to 0.445) with a lower baseline at 5.0 G. This presents a scenario where a minimum threshold for sensing (between 0.445 and 0.472) can account for the diminished effect at the higher field of 5.0 G. We must however take a note that an accompanying high sensitivity is required.

128 Relevant Timescales

Unlike in the ferromagnetic-based model, we have so far not considered the switching profile of the magnetic fields in our test conditions. Intuitively, since the lowest decay rate used is $k_d = 10^6$ Hz, the system would arrive at a steady state far quicker than the switching frequency. This means that a magnetic sense with the parameters proposed functions essentially instantaneously. We note that the population in ρ_4 will be unity if the radical pairs in ρ_1 , ρ_2 and ρ_3 remain in the triplet state so that no recombination to ρ_5 occurs while the population in ρ_4 will be minimal if all the radical pairs were in the singlet state. The first scenario will be referred to as the lower bound and the former as the upper bound to the population in ρ_3 . Another way to view the two scenarios is with the following rate equations:

$$\dot{p}_1 = (-k_{\text{et}} - v \, k_b) \, p_1,
\dot{p}_2 = (-k_{\text{et}} - v \, k_b) \, p_2 + k_{\text{et}} \, p_1,
\dot{p}_3 = (-k_d - v \, k_b) \, p_3 + k_{\text{et}} \, p_2,$$
(4.19)

where p_j is the population of the state ρ_j and v = 0, 1 corresponds to the upper and lower bound scenarios. This set of equations admits an analytical solution:

$$p_{1} = \exp[(-v k_{b} - k_{\text{et}})t],$$

$$p_{2} = k_{\text{et}} t p_{1},$$

$$p_{3} = \frac{k_{\text{et}}^{2}}{(k_{\text{et}} - k_{d})^{2}} \left[\exp((-v k_{b} - k_{d})t) - p_{1}\right] - \frac{k_{\text{et}}}{k_{\text{et}} - k_{d}} p_{2}.$$

$$(4.20)$$

Due to the spin selectivity of the recombination reaction, the actual value of p_3 will be somewhere between the two bounds. From these bounds, we can infer the minimum and maximum timescales of the magnetic sense. Fig. 4.10 shows the population dynamics of ρ_3 in thick solid lines for various magnetic field strengths is well within the lower and upper bounds in dashed lines. Additionally, the population dynamics of ρ_1 and ρ_2 are shown in thin lines. From the inset that shows a close-up of the dynamics, we see that the populations in ρ_1 and ρ_3 very quickly approach zero within 50 ns, so that the remainder of the reaction depends wholly on ρ_3 . Overall, the reaction terminates by around 1 μ s, which on biological scales would resemble an instantaneous sense.

It should be mentioned that in [131], the singlet / triplet populations in ρ_3 were shown to reach peak values of at most 0.05 within 500 ns (Fig. 10 in the reference). This means that the total population of ρ_3 , consisting of both singlet and triplet, is at most 0.1, which is considerably different from the current discussions that show this value to be somewhere between 0.5 to 0.9 (see Fig. 4.10). Intuitively, one should expect that because the electron transfer rate is an order of magnitude faster than the recombination rates and two orders of magnitude faster than the decay rate to the signalling state, that the dynamics in the chain $\rho_1 \to \rho_2 \to \rho_3$ will be comparatively fast, resulting in a significant build-up of pairs in the state ρ_3 , in agreement with the discussion presented.

1145 Discussion

1130

1132

1133

1134

1135

1137

1138

1139

1140

1141

1142

1143

1147

1150

1151

1152

Thus far, the radical pair model has a larger signal yield at 0.5 G than at 5 G and operates at very short timescales. This presents us with a viable magnetic sense that can account for the increase in cockroach activity in the RESF as compared to the controls as well as the diminishing effect of 5 G test. Since the radical pair reaction completes within microseconds, from the perspective of the cockroach, it would experience a discontinuous change in the population of the signalling state every 5 minutes due to the RESF. This is of course an oversimplification and more complex chemical and biological processes are probably interwoven to eventually constitute the full magnetic sensing apparatus.

The RPM model can account for the diminishing magnetic sense at 5 G in one of two ways. The most direct

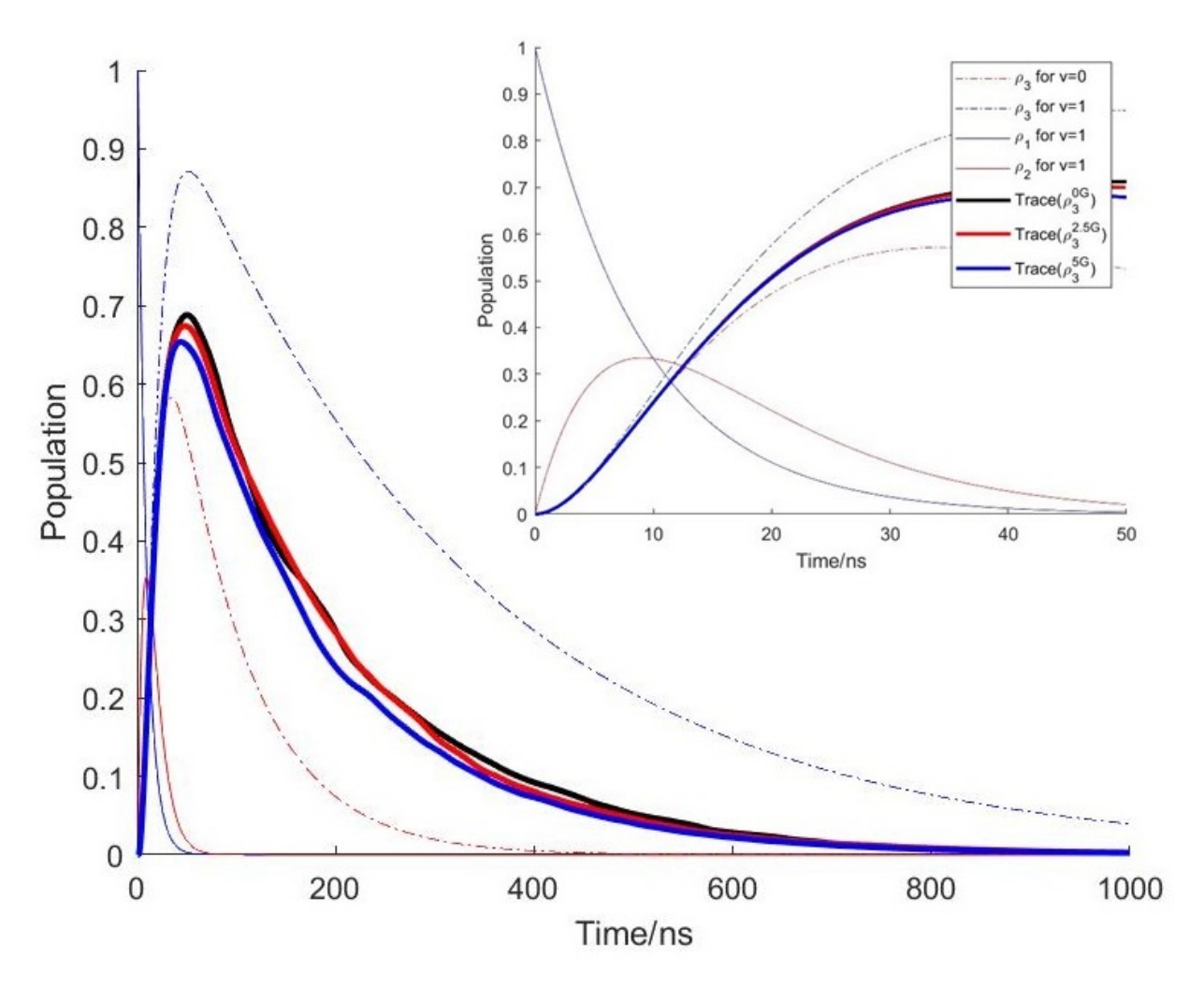


Fig. 4.10: Population dynamics of the radical pairs $(\rho_1, \rho_2, \text{ and } \rho_3)$ involved in the radical pair scheme discussed. The reaction reaches a steady state in about 1 μ s. The inset shows in more detail the dynamics between 0 to 50 ns.

explanation is a threshold for sensing, since the baseline reading in 0.5 G (0.472) is actually larger than
the maximum signal in 5 G (0.445). If a minimum value between 0.445 and 0.472 is required for proper
functioning of the magnetic sense, then the sense could be disrupted in the larger field. A caveat here is that
the variation in the signal yield at 0.5 G is quite small (only between 0.472 - 0.48), requiring an accompanying
high sensitivity. Another possibility is due to the difference in the signal profile between 0.5 G and 5 G.
As the yield at 5 G is not just a numerically scaled down version of 0.5 G, the animal may have become
disoriented at the 'new' readings. There is precedent of this in birds, where they were initially disoriented
but eventually adapted to navigate in different field strengths [20, 28].

Despite this, the current model still leaves much to be desired with this open looped reaction scheme. The timescale of the reaction presents an issue in that without some form of replenishment to ρ_1 , this reaction would proceed and terminate within microseconds with end products in ρ_4 and ρ_5 . This restricts the magnetic sense from being real-time as only a single snapshot of the magnetic field is perceivable. In the next section, we attempt to rectify this by introducing new processes in order to create a closed loop.

1167 Looped Dynamics

The most straightforward way to close the loop would be to introduce two processes: one connecting the signalling state ρ_4 back to the precursor state ρ_5 with reaction constant k_{\odot} and an excitation process to connect the precursor to the initial state ρ_1 with reaction constant k_{ex} . This looping need not necessarily involve a recycling of the population of the signalling state. A source and sink for the precursor and signal states respectively effectively serve the same function. The looped reaction dynamics is shown in Fig. 4.11.

For the looped dynamics to be meaningful, a few bounds are necessary. Firstly, $k_{\odot} \ll k_d$ is required for a meaningful accumulation of the signalling state instead of constantly recycling the products, and $k_{ex} < k_{\odot}$ for the system to reach a steady state with ρ_5 behaving as a sink. In Fig. 4.12, we show the looped signal yield by setting $k_{ex} = 5 \times 10^6$ Hz and $k_{\odot} = 10^7$ Hz. Notably, we obtain a qualitatively similar profile to that of the base reaction scheme (Fig. 4.9), except with a lower baseline. Nevertheless, this shows that the radical pair mechanism is somewhat robust, still functioning in less sterile environments with chemicals entering and leaving the system.

1180 4.2.4 Summary

To summarise, we have conducted behavioural experiments on American cockroaches (Periplaneta ameri-1181 cana), showing that they display sensitivity to periodical directional switching of the Earth-strength magnetic 1182 fields, manifesting as an increased activity time during the day. This agrees with previous experimental find-1183 ings of the group of Dr. Vacha [23,119] which they have dubbed as Magnetically Induced Restlessness (MIR). 1184 We have additionally found that this magnetic sensitivity appears to be tuned to Earth's geomagnetic field, 1185 having become diminished in a 5G switching field. A similar observation, of disorientation in fields with 1186 strengths higher from the typical geomagnetic values, is found in several species of birds [20, 28], and even 1187 the honeybee Schwaziana quadripunctata [145]. 1188

We analysed the magnetite and radical pair mechanisms and concluded that our experimental observations suggested that the radical pair mechanism is the basis for cockroach magnetic sensitivity. It should be noted that fast switching magnetic fields are not often found in nature, so magnetic sensitivity at short time scales is unlikely a necessity for a functioning magnetic sense. It is still possible for both the magnetite and radical pair mechanism to work in tandem for cockroach magnetic sensitivity.

Using parameters of the single-domain magnetite grain sizes from other experiments [124], the weak strength of the RESF is unable to overcome the much larger viscous forces of the cellular media inside the cockroach. Furthermore, if the alignment was directly correlated to the efficacy of magnetic sensitivity, then the magnetic model is irreconcilable with the diminishing magnetic sense in a larger field. On the other hand,

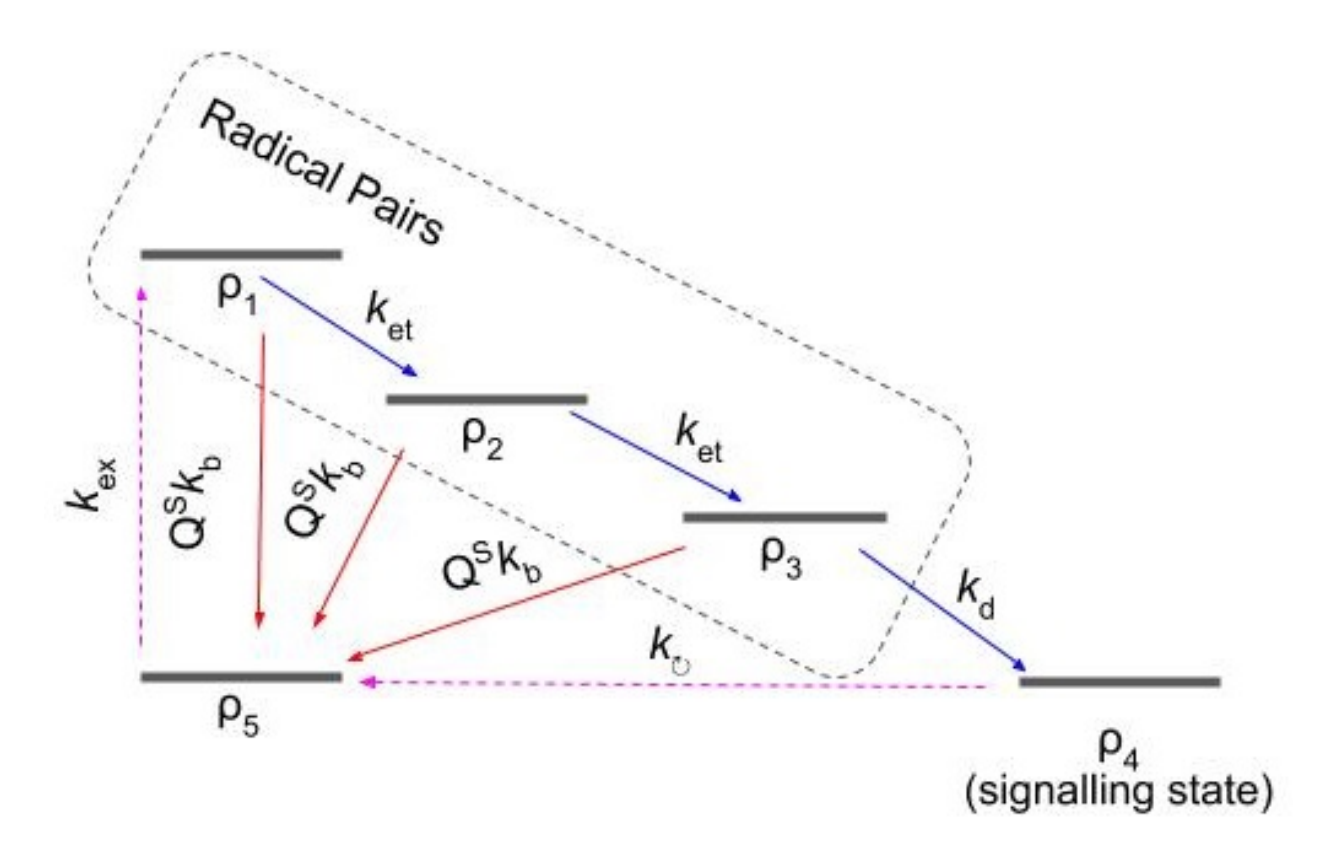


Fig. 4.11: The proposed 'looped' dynamics: introducing two extra channels (as compared to the base reaction scheme in Fig. 4.8) shown as pink dashed arrows. These two new channels are governed by decay constants k_{ex} for excitation of precursor ρ_5 to the first radical pair ρ_1 and k_{\circlearrowleft} for the recycling of the signal state ρ_4 back to the precursor.

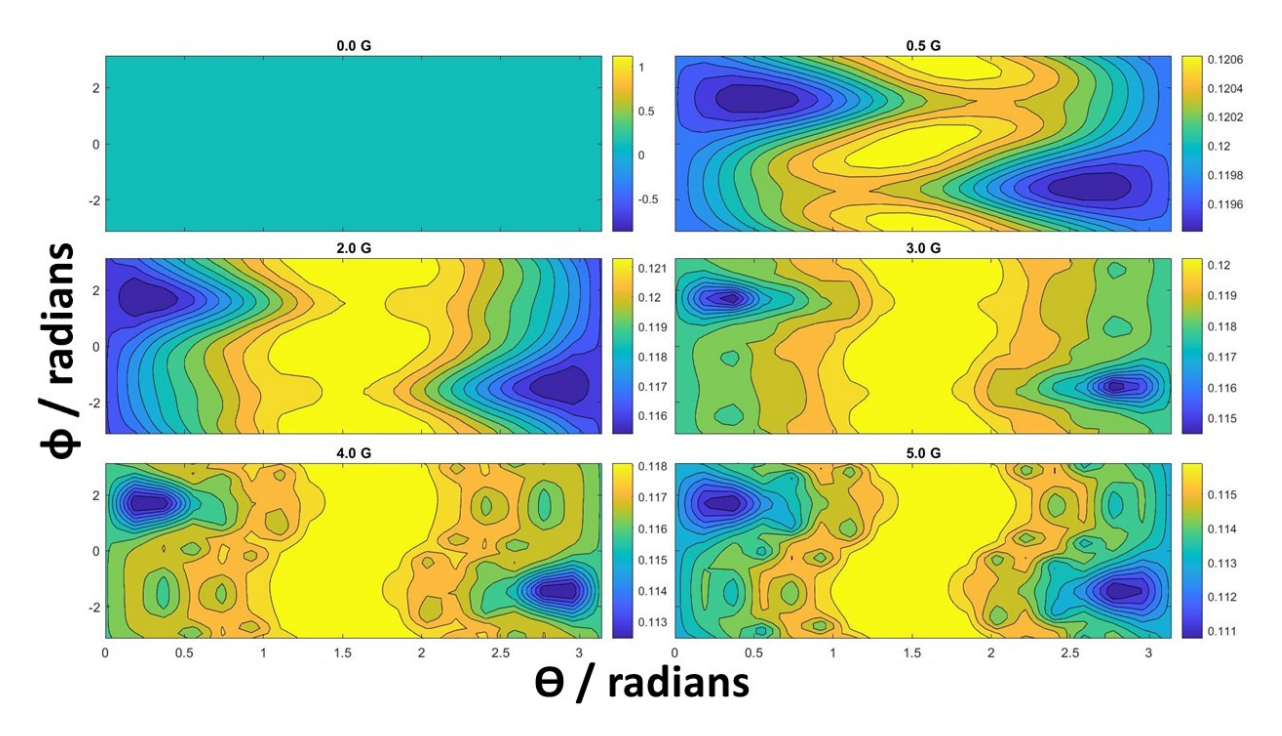


Fig. 4.12: Contour plots of the steady state signal yield in the looped reaction scheme shown in Fig. 4.11 as a function of θ and ϕ in the presence of different aligning field strengths. The decay parameters used were $k_b = 10^7$ Hz, $k_{et} = 10^8$ Hz and $k_d = 3.3 \times 10^6$ Hz, similar to that in the original model without any looping. Additionally, the two newly introduced channels have decay parameters $k_{ex} = 5 \times 10^6$ Hz and $k_{\circlearrowleft} = 10^7$ Hz.

the radical pair mechanism can respond fast enough to the RESF, and the qualitatively different signal profiles under different magnetic field conditions could disorient the cockroach. The caveat however, is that the current model requires a high sensitivity threshold with the variation of the maximum and minimum signal yield at 0.5 G only being about 0.08. Lastly, a looped model is discussed and shown to still perform qualitatively similar to the original model.

As an outlook, we point out that the current calculations were performed using the geometry and hyperfine coupling values from *Arabidopsis thaliana* Cryptochrome-1, and transition rates from *E. coli* photolyase. While the cryptochrome/photolyase family of proteins have highly conserved structures, it will still be worth revisiting these calculations using parameters from *Periplaneta americana* Cryptochrome-2 (recall that this form of cryptochrome was identified in Ref. [121]) given the non-trivial relationship between the hyperfine coupling and signal yield.

Part III

1209

1210

Entanglement in Living Systems

Perhaps the most direct way to observe quantum effects is to attempt to
entangle a biological system with a quantum one. In the following chapters, we
introduce some theoretical background of the relevant models used to describe
quantum systems, before describing an experiment to observe entanglement in
a qubit-qubit-tardigrade system.

Chapter 5

Quantum Harmonic Oscillators

As Sidney Coleman once put it, "The career of a young theoretical physicist consists of treating the harmonic oscillator in ever-increasing levels of abstraction." In this chapter, we go through a brief theoretical
background on relevant concepts for the chapters that follow.

5.1 Theoretical Background

To begin our discussion, we need to build some theoretical overview of the relevant systems to be used. In this chapter, a modest review of the physics behind quantum systems, then quantum harmonic oscillators and eventually into qubits, are presented. The qubit systems that we are concerned with, superconducting transmons, are also discussed.

1226 5.1.1 Spin

1235

1237

1238

1239

1240

Spin is an intrinsic angular momentum of elementary particles. It was named as such by George Uhlenbeck and Samuel Goudsmit back in 1925 [146] because it was initially thought to have originated from an electron physically rotating in space. Interestingly, Ralph Kronig had proposed this earlier in that year but was intimidated by Werner Heisenberg and Wolfgang Pauli into not publishing it. Whichever the case, this interpretation was soon proven wrong by the Dirac equation [147] that showed the origin of the electron spin was in actuality, a consequence of quantum mechanics and relativity. In short, spin is one of the hallmarks of quantum mechanics.

5.1.2 Quantum systems

In the most simplest of sense, quantum systems are, literally from its namesake, discrete systems. In our modern formulation of quantum mechanics, for any quantum system, there exists some mathematical entity called the state, usually denoted by the Greek letter ψ and sometimes ϕ , that contains and fully describes all of its physical properties. This is one of the fundamental axioms of quantum mechanics. As an example, let us now consider a stationary spin $\frac{1}{2}$ particle like an electron. We adopt Dirac's bra-ket notation so that the two-dimensional Hilbert space for this system is spanned by the orthonormal states $|\uparrow\rangle$ and $|\downarrow\rangle$. The state of this system can then be written as a superposition of these basis states:

$$|\psi\rangle = a |\uparrow\rangle + b |\downarrow\rangle, \tag{5.1}$$

where a and b are complex coefficients. By convention, it is usually implied when writing states like in Eq. 5.1 that they are normalised in the following way: $|a|^2 + |b|^2 = 1$. If we were to attempt to check the spin of our particle, i.e. by making a measurement, then we would find that the spin would be up with probability $|a|^2$ and down with $|b|^2$, so the normalisation ensures consistency of this probabilistic interpretation.

5.1.3 Multi-particle systems

1246

If we now have multiple spin $\frac{1}{2}$ particles, each individually described by the state given in Eq. 5.1, then the combined system is described by Hilbert space being a tensor product of individual Hilbert spaces,

$$\mathcal{H}_{12} = \mathcal{H}_1 \otimes \mathcal{H}_2 \tag{5.2}$$

This space contains states that cannot be writen as $|\psi_1\rangle \otimes |\psi_2\rangle$, such states are said to be entangled. Well-known examples of entangled states are the Bell-states,

$$\begin{aligned} \left|\phi^{+}\right\rangle &= \frac{1}{\sqrt{2}}(\left|\downarrow\downarrow\right\rangle + \left|\uparrow\uparrow\right\rangle) \\ \left|\phi^{-}\right\rangle &= \frac{1}{\sqrt{2}}(\left|\downarrow\downarrow\right\rangle - \left|\uparrow\uparrow\right\rangle) \\ \left|\psi^{+}\right\rangle &= \frac{1}{\sqrt{2}}(\left|\downarrow\uparrow\right\rangle + \left|\uparrow\downarrow\right\rangle) \\ \left|\psi^{-}\right\rangle &= \frac{1}{\sqrt{2}}(\left|\downarrow\uparrow\right\rangle - \left|\uparrow\downarrow\right\rangle). \end{aligned}$$

$_{\scriptscriptstyle{249}}$ 5.1.4 Quantum Harmonic Oscillator

A classical harmonic oscillator corresponds to a system that experiences some restoring force, \vec{F} , proportional to the displacement, \vec{x} , from its equilibrium position. In other words,

$$F = -kx, (5.3)$$

where k as the constant of proportionality and we have restricted ourselves to the 1-dimensional case for simplicity. As an example, let us now consider specifically a particle of mass m attached on one end to a spring with spring constant k and the other end fixed to some surface. If we were to give the particle some initial displacement $x(0) = x_0$, then we can expect it to oscillate back and forth over time. More specifically, the particle is expected to have kinetic energy, T, at some time t given by

$$T(t) = \frac{p(t)^2}{2m},\tag{5.4}$$

where p(t) is the momentum of the particle. Consequently, the spring system contains elastic potential energy,

$$V(t) = \frac{1}{2}kx(t)^{2}. (5.5)$$

In the Hamilton's description, this system has the Hamiltonian given by the sum of its kinetic and potential energy components,

$$H = T + V \tag{5.6}$$

$$=\frac{p(t)^2}{2m} + \frac{1}{2}kx(t)^2. (5.7)$$

In moving from the classical to the quantum picture, one performs the first quantization which involves replacing the position and momentum conjugate variables x and p with their quantum mechanical operator counterparts,

$$x \to \hat{x}$$
 (5.8)

$$p \to \hat{p},$$
 (5.9)

that obey the commutation relations

$$[\hat{x}, \hat{p}] = i\hbar. \tag{5.10}$$

We will solve the quantum harmonic oscillator using ladder operators, a remarkably elegant method first used by Paul Dirac [148]. By defining the following operators,

$$\hat{a} = \sqrt{\frac{m\omega}{2\hbar}} \left(\hat{x} + \frac{i}{m\omega} \hat{p} \right), \tag{5.11}$$

$$\hat{a^{\dagger}} = \sqrt{\frac{m\omega}{2\hbar}} \left(\hat{x} - \frac{i}{m\omega} \hat{p} \right), \tag{5.12}$$

we can rewrite the Hamiltonian of quantum harmonic oscillator as

$$\hbar\omega(a^{\dagger}a + \frac{1}{2}) = \frac{m\omega^2}{2} \left(\hat{x}^2 + \frac{i}{m\omega}\hat{x}\hat{p} - \frac{i}{m\omega}\hat{p}\hat{x} + \frac{1}{m^2\omega^2}\hat{p}^2\right) + \frac{1}{2}\hbar\omega \tag{5.13}$$

$$=\frac{\hat{p}^2}{2m} + \frac{1}{2}m\omega^2\hat{x}^2 + \frac{i\omega}{2}[\hat{x},\hat{p}] + \frac{1}{2}$$
 (5.14)

$$=\frac{\hat{p}^2}{2m} + \frac{1}{2}m\omega^2\hat{x}^2. \tag{5.15}$$

Moreover, by applying $\hat{H}\hat{a}^{\dagger}$ and $\hat{H}\hat{a}$ on eigenstates of H, we see that by using the commutation relations $[\hat{a}, \hat{a}^{\dagger}] = 1$,

$$\hat{H}\hat{a}^{\dagger} |\psi\rangle = \hbar\omega(\hat{a}^{\dagger}\hat{a} + \frac{1}{2})\hat{a}^{\dagger} |\psi\rangle \tag{5.16}$$

$$=\hbar\omega\hat{a}^{\dagger}(\hat{a}\hat{a}^{\dagger}+\frac{1}{2})|\psi\rangle \tag{5.17}$$

$$= \hbar \omega \hat{a}^{\dagger} (1 + \hat{a}^{\dagger} \hat{a} + \frac{1}{2}) |\psi\rangle \tag{5.18}$$

$$= (E + \hbar\omega)\hat{a}^{\dagger} |\psi\rangle, \qquad (5.19)$$

and similarly,

$$\hat{H}\hat{a}|\psi\rangle = (E - \hbar\omega)\hat{a}|\psi\rangle. \tag{5.20}$$

Thus, the action of \hat{a}^{\dagger} and \hat{a} on the eigenenergy states is to raise or lower them by $\hbar\omega$. This is why they are also called the creation and annihilation operators respectively.

5.1.5 Fock states

1264

1263 The new form of the harmonic oscillator Hamiltonian in terms of creation and annihilation operators reads:

$$\hat{H} = \hbar\omega(\hat{a}^{\dagger}\hat{a} + \frac{1}{2}). \tag{5.21}$$

Now, one can also ask what the actions of the creation and annihilation operators are on the energy eigenstates. To do this, it is helpful to define an occupation number operator \hat{N} as,

$$\hat{N} = \hat{a}^{\dagger} \hat{a},\tag{5.22}$$

from which we can see that the eigenstates of the quantum harmonic oscillator are also eigenstates of this number operator. To understand the significance of the number operators, we first write explicitly the eigenequation,

$$\hat{N}|n\rangle = n|n\rangle, \tag{5.23}$$

where $|n\rangle$ are the eigenstates or "Fock states" with corresponding non-negative integer eigenvalues n. While we do not show this rigorously, the spectrum of the quantum harmonic oscillator is indeed discretely separated by the energy quanta of $\hbar\omega$ as seen from Eq. 5.19 and 5.20. Now, we consider the effect of the operators $\hat{N}\hat{a}^{\dagger}$ and $\hat{N}\hat{a}$ on the eigenstate $|n\rangle$,

$$\hat{N}\hat{a}^{\dagger} | n \rangle = \hat{a}^{\dagger} \hat{a} \hat{a}^{\dagger} | n \rangle \tag{5.24}$$

$$= \hat{a}^{\dagger} (\hat{a}^{\dagger} \hat{a} + 1) \hat{a} | n \rangle \tag{5.25}$$

$$= (n+1)\hat{a}^{\dagger} |n\rangle , \qquad (5.26)$$

and,

$$\hat{N}\hat{a}|n\rangle = \hat{a}^{\dagger}\hat{a}\hat{a}|n\rangle \tag{5.27}$$

$$= (\hat{a}\hat{a}^{\dagger} - 1)\hat{a} |n\rangle \tag{5.28}$$

$$= (n-1)\hat{a} |n\rangle, \qquad (5.29)$$

from which we can infer that

$$\hat{a}^{\dagger} | n \rangle = \sqrt{n+1} | n+1 \rangle , \qquad (5.30)$$

$$\hat{a}|n\rangle = \sqrt{n}|n-1\rangle,\tag{5.31}$$

where the square root terms are for normalisation. These eigenkets $|n\rangle = |0\rangle, |1\rangle, |2\rangle, \dots$ help in visualising quantum harmonic energy levels as an evenly spaced discrete ladder of energies.

5.1.6 Zero-point Energy

From Eq. 5.21, we note that the lowest possible energy of the quantum harmonic oscillator is a non-zero value,

$$\hat{H}|0\rangle = \frac{1}{2}\hbar\omega|0\rangle, \qquad (5.32)$$

which is also often referred to as the zero-point energy. This is the lowest energy a physical system can possess, and is fundamentally related to the Heisenberg uncertainty principle.

Often times, this zero-point energy is not directly relevant experimentally when one is looking at transition energies as the additive terms cancel out. As such, we will neglect the zero-point energy in the following chapters.

With some understanding on quantum harmonic oscillators, we can now move on to cavity quantum electrodynamics. In essence, cavities and electromagnetic fields can also be generalised to some form of a quantum harmonic oscillator, and thus can be thought of as more complex systems of interacting oscillators.

Sample Chapter 6

Cavity Quantum Electrodynamics

One of the basic results of quantum electrodynamics is the quantisation of the electromagnetic fields, recasting the Hamiltonian of the field into a similar form to that of a harmonic oscillator [149] which can then be quantised in a similar manner outlined in the previous chapter. In cavity quantum electrodynamics (cQED), the boundary conditions of a cavity are then applied to restrict the radiation modes to the discrete cavity modes. While usually applied to the coupling and interaction of atoms to photonic cavity modes, the model easily generalises to other systems given that most systems can be simplified to harmonic oscillators and further reduced to two-level systems at low enough temperatures.

In this chapter, we birefly outline a few models commonly used in cQED: Rabi [150,151], Jaynes-Cummings [152], Dicke [153] and Tavis-Cummings models [154]. These models are very closely related, and names are often times used interchangeably. In this chapter, the Rabi model will refer to coupling between a single two-level system (TLS) with cavity modes while the Dicke model involves an ensemble of N two-level systems coupled to the cavity modes. The Jaynes-Cummings and Tavis-Cummings models refer to simplifications by taking the Rotating Wave Approximation (RWA) of the Rabi and Dicke models respectively. The main differences are summarised in Table 6.1.

	Number of Two-Level Systems	Rotating Wave Approximation
Rabi	N = 1	No
Jaynes-Cummings	N = 1	Yes
Dicke	N > 1	No
Tavis-Cummings	N > 1	Yes

Table 6.1: Main differences between the Rabi, Jaynes-Cummings, Dicke and Tavis-Cummings models.

6.1 Rabi model

The semi-classical Rabi model was first proposed in 1936 by Isidor Rabi to describe interactions between a two-level atom with a gyrating magnetic field [150,151]. It would not be till 1963 that a fully quantised Rabi model was introduced by Jaynes and Cummings [152] - the very same Jaynes and Cummings who developed the ubiquitous Jaynes-Cummings model with applications ranging from quantum optics [155] to condensed-matter [156]. We will return to the Jaynes-Cummings model in the following section. The quantum Rabi model has the Hamiltonian

$$H_R = \hbar \omega_c a^{\dagger} a + \hbar \omega_a \sigma_z + \hbar g (a^{\dagger} + a)(\sigma_+ + \sigma_-), \tag{6.1}$$

where $\sigma_{z,\pm}$ are the Pauli-z, raising and lowering operators for the qubit with lower (higher) energy state denoted as $|0\rangle$ ($|1\rangle$), a (a^{\dagger}) is the lowering (raising) operator for the oscillator, and $\hbar g$ is the interaction energy. Note that vanishing energy of the qubit has been set in the middle between its energy levels and the ground state of the oscillator is assigned energy zero. Even though this form of matter-light interaction appears in almost every branch of modern physics (since the coupling is the quantised version of dipole interactions), the Rabi hamiltonian was only fully solved in 2011 by Braak [157].

To start off, we first highlight the reason that makes the Rabi problem more complex than the Jaynes-Cummings. For the choice of basis for the Hilbert space of this system, we take the number states of the form $|\alpha\rangle|\beta\rangle$ where α is either 0 or 1, representing the lower and higher energy level of the TLS respectively, and β takes on any non-negative integer value, representing the occupation number of the cavity mode. In this representation, we note that the first two terms in Eq. 6.1 preserve number of excitations, $N_{exc} = \alpha + \beta$. For the terms in the brackets, we have the "rotating terms", $a^{\dagger}\sigma_{-} + a\sigma_{+}$, that also preserve N_{exc} , which can be thought of as absorption and emission of photons by the TLS. However, this symmetry is broken by the remaining terms in the brackets, the "counter rotating terms", $a^{\dagger}\sigma_{+} + a\sigma_{-}$, that change the excitation number by ± 2 . The Rabi model only has a \mathbb{Z}_{2} symmetry, sometimes called parity, which decomposes the Hilbert space into a direct sum of two infinite dimensional subspaces,

$$\mathcal{H} = \mathcal{H}_{+} \bigoplus \mathcal{H}_{-}, \tag{6.2}$$

each with a different parity denoted as +1 for even and -1 for odd. Without a definite excitation number, the Rabi problem becomes significantly complicated and was even initially thought to be non-integrable [158].

Instead of following Braak's original derivations, which are highly mathematical, we adopt the method of Chen [159] which will be more familiar to most physicists. We begin by rewriting the Rabi Hamiltonian in a slightly different form and setting \hbar to 1,

$$H_R = \omega_c a^{\dagger} a + \omega_a \sigma_x + g(a^{\dagger} + a)\sigma_z, \tag{6.3}$$

which is identical to Eq. 6.1 except that $|0\rangle = \frac{1}{\sqrt{2}}[1,1]$ and $|1\rangle = \frac{1}{\sqrt{2}}[1,-1]$ are now the eigenvectors of σ_x instead of the standard basis form of $|0\rangle = [1,0]$ and $|1\rangle = [0,1]$. This Hamiltonian (Eq. 6.3) has the matrix form,

$$H_R = \begin{pmatrix} a^{\dagger} a + g(a^{\dagger} + a) & \omega_c \\ \omega_c & a^{\dagger} a - g(a^{\dagger} + a) \end{pmatrix}, \tag{6.4}$$

where we can apply the Bogoliubov transformations:

$$A = a + g, (6.5)$$

$$B = a - g, (6.6)$$

so that

$$H_R = \begin{pmatrix} A^{\dagger}A - g^2 & \omega_c \\ \omega_c & A^{\dagger}A - 2g(A^{\dagger} + A) + 3g^2 \end{pmatrix}. \tag{6.7}$$

Now we use the ansatz for the time-independent Schrödinger equation:

$$|\psi\rangle = \begin{pmatrix} \sum_{n=0}^{\infty} \sqrt{n!} e_n |n\rangle_A \\ \sum_{n=0}^{\infty} \sqrt{n!} f_n |n\rangle_A \end{pmatrix}$$
 (6.8)

where e_n and f_n are undetermined constants as of yet, while $|n\rangle_A$ is a so-called "extended coherent state", satisfying the equation

$$|n\rangle_A = \frac{(A^\dagger)^n}{\sqrt{n!}} |0\rangle_A, \tag{6.9}$$

with $|0\rangle_A$ being the vacuum state for the Bogoliubov operators, given by

$$|0\rangle_A = \exp\left(-\frac{1}{2}g^2 - ga^{\dagger}\right)|0\rangle_a, \qquad (6.10)$$

where we have used $|0\rangle_a$ to denote the vacuum state of the Fock number states. The state $|0\rangle_A$ is a coherent state, which is an eigenstate of the annihilation operator, i.e.

$$a \left| 0 \right\rangle_A = -g \left| 0 \right\rangle_A. \tag{6.11}$$

Some helpful relations of the Bogoliubov operators A and A^{\dagger} acting on the extended coherent states will be derived, starting with

$$A^{\dagger} |n\rangle_{A} = \sqrt{n+1} \frac{(A^{\dagger})^{n+1}}{\sqrt{(n+1)!}} |0\rangle_{A}$$
 (6.12)

$$=\sqrt{n+1}\left| n+1\right\rangle _{A}, \tag{6.13}$$

and

$$A|n\rangle_A = \frac{A(A^{\dagger})^n}{\sqrt{n!}}|0\rangle_A \tag{6.14}$$

$$= \frac{n(A^{\dagger})^{n-1} + (A^{\dagger})^{n}(a+g)}{\sqrt{n!}} |0\rangle_{A}$$
(6.15)

$$= n \frac{(A^{\dagger})^{n-1}}{\sqrt{n(n-1)!}} |0\rangle_A \tag{6.16}$$

$$=\sqrt{n}\left|n-1\right\rangle_A,\tag{6.17}$$

where we have used the commutation relations $[A, A^{\dagger}] = 1$ and Eq. 6.11 to obtain our results. Finally, combining both Eq. 6.13 and 6.17, we have

$$A^{\dagger}A |n\rangle_{A} = n |n\rangle_{A}. \tag{6.18}$$

In short, the Bogoliubov operators act like creation and annihilation operators on the extended coherent states. Plugging the ansatz into the time-independent Schrödinger equation, $E|\psi\rangle = H_R|\psi\rangle$, and the relations in Eq. 6.13-6.18, we obtain the pair of equations

$$E\sum_{n=0}^{\infty} \sqrt{n!} e_n |n\rangle_A = \sum_{n=0}^{\infty} (n - g^2) (\sqrt{n!} e_n |n\rangle_A + \omega_c \sqrt{n!} f_n |n\rangle_A), \tag{6.19}$$

$$E\sum_{n=0}^{\infty} \sqrt{n!} f_n |n\rangle_A = \sum_{n=0}^{\infty} \sqrt{n!} [(\omega_c e_n + (n+3g^2) f_n) |n\rangle_A - 2g\sqrt{n} f_n |n-1\rangle_A - 2g\sqrt{n+1} f_n |n+1\rangle_A]. \quad (6.20)$$

Using the orthogonality property of the extended coherent states, left multiplying by $_{A}\left\langle m\right|$ gives

$$(m - g^2 - E)e_m = -\omega_c f_n \tag{6.21}$$

$$(m+3g^2-E)f_m - 2g(m+1)f_{m+1} - 2gf_{m-1} = -\omega_c e_m.$$
(6.22)

In other words, the coefficients f_m have a recursive relation:

$$mf_m = \Omega(m-1)f_{m-1} - f_{m-2},\tag{6.23}$$

$$\Omega(m) = \frac{1}{2g} \left((m + 3g^2 - E) - \frac{\omega_c^2}{m - g^2 - E} \right), \tag{6.24}$$

with initial values $f_0 = 1$ and $f_1 = \Omega(0)$, while e_m is determined from f_m by the expression,

$$e_m = -\frac{\omega_c}{2(m - g^2 - E)} f_m. (6.25)$$

We can repeat the same process for the operator B to get,

$$H_R = \begin{pmatrix} B^{\dagger}B + 2g(B^{\dagger} + B) + 3g^2 & \omega_c \\ \omega_c & B^{\dagger}B - g^2 \end{pmatrix}, \tag{6.26}$$

and define another ansatz for this Hamiltonian as

$$|\phi\rangle = \begin{pmatrix} \sum_{m=0}^{\infty} (-1)^m \sqrt{m!} f'_m | m \rangle_B \\ \sum_{m=0}^{\infty} (-1)^m \sqrt{m!} e'_n | m \rangle_B \end{pmatrix}, \tag{6.27}$$

with another set of undetermined coefficients e'_m and f'_m . Repeating as before, the relations for e'_m and f'_m are

$$e'_{m} = -\frac{\omega_{c}}{m - q^{2} - E} f'_{m}, \tag{6.28}$$

$$mf'_{m} = \Omega'(m-1)f'_{m-1} - f'_{m-2}, (6.29)$$

$$\Omega'(m) = \frac{1}{2g} \left[(m + 3g^2 - E) - \frac{\omega_c^2}{m - g^2 - E} \right], \tag{6.30}$$

with $f'_0 = 1$ and $f'_1 = \Omega'(0)$. If the ansatz of Eq. 6.8 and 6.27 are indeed proper eigenfunctions, then they will only differ by a complex factor r,

$$\sum_{n=0}^{\infty} \sqrt{n!} e_n |n\rangle_A = r \sum_{m=0}^{\infty} (-1)^m \sqrt{m!} f'_m |m\rangle_B$$
 (6.31)

$$\sum_{n=0}^{\infty} \sqrt{n!} f_n |n\rangle_A = r \sum_{m=0}^{\infty} (-1)^m \sqrt{m!} e'_m |m\rangle_B$$
 (6.32)

By noting that

$$\sqrt{n!}_a \langle 0|n\rangle_A = \sqrt{n!} \left(_a \langle 0| \frac{(A^{\dagger})^n}{\sqrt{n!}}\right) \exp\left(-\frac{1}{2}g^2 - ga^{\dagger}\right) |0\rangle_a \tag{6.33}$$

$$=_a \langle 0 | \frac{g^n}{\exp}(-\frac{1}{2}g^2) | 0 \rangle_a \tag{6.34}$$

$$=\exp\left(-\frac{1}{2}g^2\right)g^n,\tag{6.35}$$

and in similar fashion, $(-1)^m \sqrt{m!}_a \langle 0|m\rangle_B = \exp\left(-\frac{1}{2}g^2\right)g^m$, we can remove $|n\rangle_A$ and $|m\rangle_B$ from Eq. 6.31 and 6.32 by left multiplication of $_a\langle 0|$, and divide one of the resulting equations by the other to further reduce the pair of equations to a single relation

$$\sum_{n=0}^{\infty} e_n g^n \sum_{m=0}^{\infty} e'_m g^m = \sum_{n=0}^{\infty} f_n g^n \sum_{m=0}^{\infty} f'_m g^m.$$
 (6.36)

Using the relationships between e_n and f_j , as well as e'_m and f'_k , we arrive at

$$\sum_{n=0}^{\infty} \frac{\omega_c}{n - g^2 - E} f_n g^n \sum_{m=0}^{\infty} \frac{\omega_c}{m - g^2 - E} f'_m g^m = \sum_{n=0}^{\infty} f_n g^n \sum_{m=0}^{\infty} f'_m g^m.$$
 (6.37)

Rearranging and rewriting for clarity,

$$G(E) = \omega_c^2 \sum_{n=0}^{\infty} \frac{1}{n - g^2 - E} f_n g^n \sum_{m=0}^{\infty} \frac{1}{m - g^2 - E} f'_m g^m - \sum_{j=0}^{\infty} f_j g^j \sum_{k=0}^{\infty} f'_k g^k = 0,$$
 (6.38)

which is Braak's solution, i.e. the roots of the function G(E) are the eigenenergies of the Rabi Hamiltonian. It should be mentioned that this solution is not truly analytic: the G functions can be reduced to Heunn functions [160], which are in turn not analytic. Numerical techniques are required to obtain the zeros of G(E).

1344 6.1.1 Jaynes-Cummings Model

The Jaynes-Cummings model is a simplification of the Rabi model. The Jaynes-Cummings Hamiltonian is

$$H_{JC} = \omega_c a^{\dagger} a + \omega_a \sigma_z + g(a^{\dagger} \sigma_- + a \sigma_+), \tag{6.39}$$

with the difference being that the counter-rotating terms, $a\sigma_{-}$ and $a^{\dagger}\sigma_{+}$, are omitted. This is often referred to as the Rotating-Wave Approximation (RWA). From a physical standpoint, the omitted terms correspond to processes that do not conserve energy - simultaneous absorption of a photon and lowering the atomic energy or emitting a photon and raising the atomic energy. A more rigorous justification states that most systems studied operate in the near-resonance regime, where the driving field and atomic frequency are not too far off-resonance. In this regime, the detuning $\Delta = |2\omega_a - \omega_c| \ll \omega_c + \omega_a$ so terms containing a sum of frequencies are rapidly oscillating and average quickly to zero [161]. To see how the RWA helps in simplifying the Rabi problem, we first show that the excitation number operator, $C = a^{\dagger}a + \sigma_{+}\sigma_{-}$, commutes with the Jaynes-Cummings Hamiltonian (Eq. 6.39),

$$[H_{JC}, C] = \omega_c[a^{\dagger}a, C] + \omega_a[\sigma_z, C] + g[a^{\dagger}\sigma_- + a\sigma_+, C]$$

$$= g\left([a^{\dagger}\sigma_-, a^{\dagger}a] + [a^{\dagger}\sigma_-, \sigma_+\sigma_-] + [a\sigma_+, a^{\dagger}a] + [a\sigma_+, \sigma_+\sigma_-]\right)$$

$$= g\left(\sigma_-[a^{\dagger}, a]a^{\dagger} + a^{\dagger}[\sigma_-, \sigma_+]\sigma_- + \sigma_+[a, a^{\dagger}]a + a[\sigma_+, \sigma_-]\sigma_+\right)$$

$$= g\left(-\sigma_-a^{\dagger} + a^{\dagger}\sigma_- + \sigma_+a - a\sigma_+\right)$$

$$= 0,$$

showing that the excitation number N is a conserved quantity. The eigenstates of C are tensor products of the atomic levels and number Fock states $\{|g,0\rangle;|g,1\rangle,|e,0\rangle;...;|g,N\rangle,|e,N-1\rangle;...\}$. Due to the conserved quantity, a continuous U(1)-symmetry [162] further subdivides the Hilbert space into an infinite number of two-dimensional subspaces with N number of excitations. Since N is invariant in time, it is sufficient to diagonalise in the subspace $\{|g,N+1\rangle,|e,N\rangle\}$. In this subspace, the eigenstates with N excitations are of the form

$$|\psi_N\rangle = A|g, N+1\rangle + B|e, N\rangle.$$
 (6.40)

Plugging this into the Schrödinger equation, we find that the eigenenergies are given by

$$E_{\pm}(N) = \omega_c \left(N + \frac{1}{2} \right) \pm \frac{1}{2} \sqrt{\Delta^2 + 4g^2(N+1)},$$
 (6.41)

with corresponding eigenstates

$$|N, +\rangle = \cos\theta |e, N\rangle + \sin\theta |g, N+1\rangle, \tag{6.42}$$

$$|N, -\rangle = \sin \theta |e, N\rangle - \cos \theta |g, N+1\rangle,$$
 (6.43)

and the mixing angle $\theta = \tan^{-1} \left(\frac{2g\sqrt{N+1}}{\Delta} \right)$.

The biggest advantage of the Jaynes-Cummings model is the closed form of the eigen-solutions. To help appreciate the effect of the counter-rotating terms, we show in Fig. 6.1 the Jaynes-Cummings and Rabi energy levels, which for the most part agree well when both conditions of near-resonance and weak coupling are fulfilled but begin to diverge quite significantly once the conditions are not met.

6.1.2 Dicke Model

1352

1356

1357

1358

1359

1364

In the Dicke model, we extend the Rabi Hamiltonian (Eq. 6.1) by considering an ensemble of N > 1 identical TLS. The Dicke Hamiltonian is then,

$$H_D = \omega_c a^{\dagger} a + \omega_a \sum_{i}^{N} \sigma_z^{(i)} + g(a^{\dagger} + a) \sum_{i}^{N} (\sigma_-^{(i)} + \sigma_+^{(i)}), \tag{6.44}$$

with the superscripts in the brackets referring to the *i*-th TLS. The Dicke Hamiltonian, like the Rabi Hamiltonian, lacks the strong continuous symmetry due to the counter-rotating terms. The presence of the collective operator terms (those in the summation brackets) makes the Dicke model difficult to solve for general values of N, and still remains an open problem. Nonetheless, several attempts have been performed by Braak, extending his methods for solutions of the Rabi Hamiltonian for N=2 [163] and N=3 [164], as well as some numerical solutions [165, 166].

6.1.3 Tavis-Cummings model

Similar to the methods outlined for the Jaynes-Cummings model, the Tavis-Cummings model is a simplification of the Dicke model by taking the RWA of Eq. 6.44, obtaining the Tavis-Cummings Hamiltonian,

$$H_{TC} = \omega_c a^{\dagger} a + \omega_a \sum_{i} \sigma_z^{(i)} + g \sum_{i} (a^{\dagger} \sigma_{-}^{(i)} + a \sigma_{+}^{(i)}).$$
 (6.45)

We can use the Holstein-Primakoff transformation [167] on the collective operators [168].

$$\sum_{i}^{N} \sigma_{-}^{(i)} = (N - b^{\dagger}b)^{\frac{1}{2}}b, \tag{6.46}$$

$$\sum_{i}^{N} \sigma_{+}^{(i)} = b^{\dagger} (N - b^{\dagger} b)^{\frac{1}{2}}, \tag{6.47}$$

$$\sum_{i}^{N} \sigma_{z}^{(i)} = b^{\dagger}b - \frac{N}{2}.$$
(6.48)

The transformation allows us to rewrite the Tavis-Cummings Hamiltonian (Eq. 6.45) in the limit of large N as,

$$H_{TC} \approx \omega_c a^{\dagger} a + \omega_a \left(-\frac{N}{2} + b^{\dagger} b \right) + g \sqrt{N} (a^{\dagger} b + a b^{\dagger}),$$
 (6.49)

by neglecting small terms with N in the denominator. Comparing this to the Jaynes-Cummings Hamiltonian (Eq. 6.39), we see that Eq. 6.49 is fairly similar, with a \sqrt{N} scaling on the coupling strength $g \to \sqrt{N}g$.

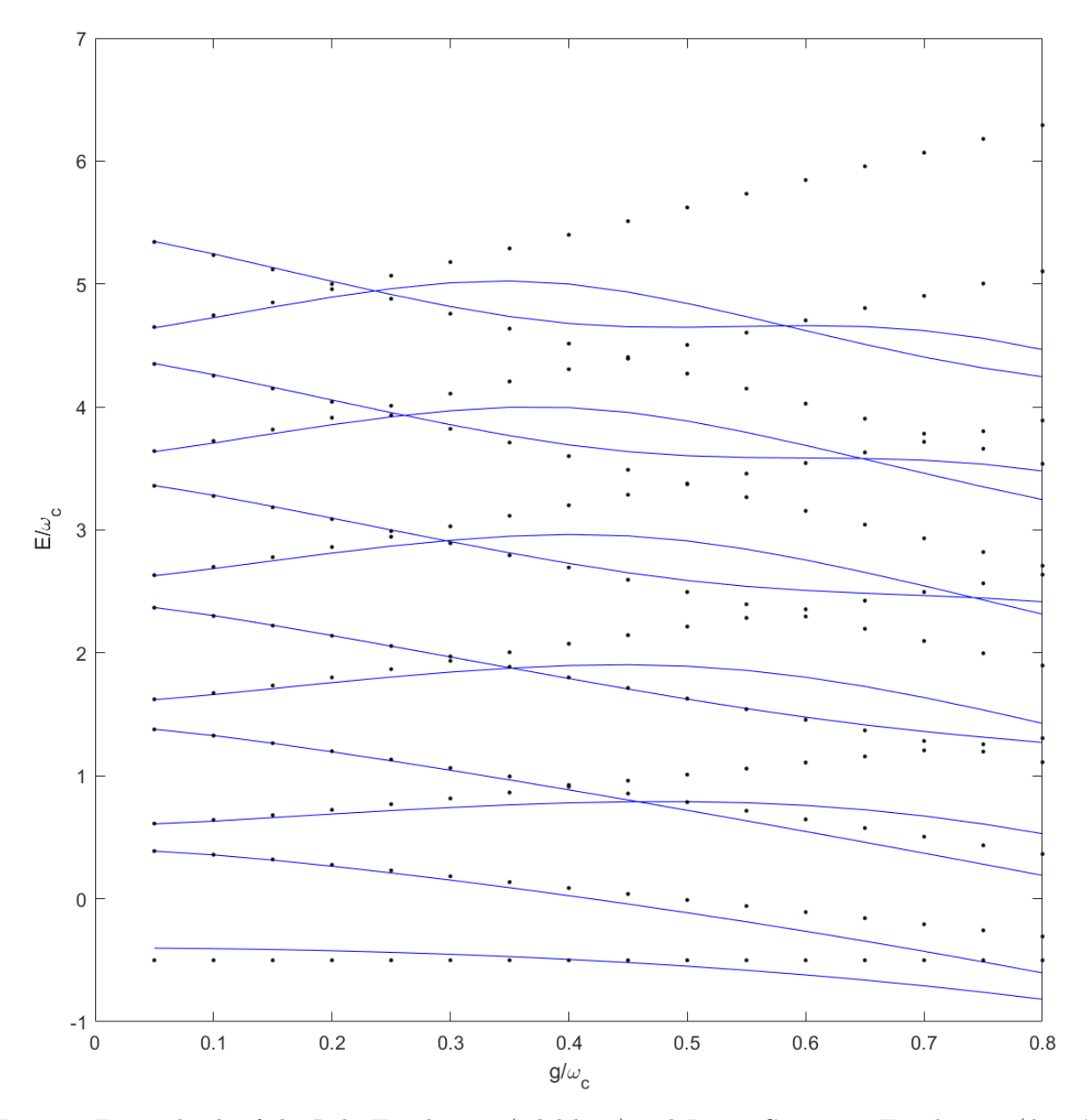


Fig. 6.1: Energy levels of the Rabi Hamiltonian (solid lines) and Jaynes-Cummings Hamiltonian (dotted lines) for $\omega_c = 1$ and $\omega_a = 0.4$, corresponding to near resonance $\Delta = 0.2$. The energy levels are similar for weak coupling but begin diverging at stronger coupling strengths.

369 **6.2** Summary

In this chapter, we have discussed the Rabi, Jaynes-Cummings, Dicke and Tavis-Cummings Hamiltonians commonly used to model cQED experiments. Other than the Dicke Hamiltonian that remains unsolved for a general N number of atoms in a cavity, the eigensystems are solved for the other Hamiltonians. Unless working in the strong coupling or far off-resonance regime, the Rabi and Jaynes-Cummings do not differ significantly. With multiple atomic systems as in the Tavis-Cummings model, the whole system can effectively be described as a giant oscillator with a larger effective coupling strength. As such, the Jaynes-Cummings is in general sufficient to describe most experimental situations.

With some background in cavity quantum electrodynamics, we will now move to our experiment on entanglement in a qubit-qubit-tardigrade system.

$_{59}$ Chapter 7

Entanglement in a qubit-qubit-tardigrade system

The following experiment bears some similarity to another experiment [169] described by Marletto et al., in which living sulphur bacteria were exposed to light and could be shown to be entangled under the Dicke model. Our experiment pushes this further by using a more complex unit of life, the multi-cellular eukaryote that is the tardigrade, interacting electrically with superconducting quantum bits. Additionally, we prepare maximally entangled Bell states between qubit-tardigrade system and another qubit.

In Neils Bohr's 1933 lectures titled "Light and Life" [170], he highlighted that studying atomic processes necessitates irreversible damage the structure of complex life forms, while studying the processes relevant to life mask the underlying atomic processes. Quantum systems tend to require highly controlled and cold environment to manifest quantum effects, while biological systems require "hot and wet" conditions to thrive. Such is the contradiction of quantum biology: quantum systems are too unconducive to life, while biological systems are too noisy to observe quantum effects. While Bohr might have been right with what was known and the technology available at that time (and for several years after), we revisit the notion here and try to convince the reader that this is no longer the case. There are two possible workarounds to the complementarity problem: increasing the robustness to quantum systems or studying biological systems that can survive in such extreme conditions. While at first glance, the latter seems absurd as the very chemical processes to maintain life must surely cease, there exists some animals that retain their functionality. In this chapter, we begin by describing the transmon qubit, a particular type of superconducting qubit, followed by the model organism: tardigrade, and an experiment to entangle the tardigrade degree of freedom with the transmon. This chapter is based on the preprint "Entanglement between superconducting qubits and a tardigrade" on the Arxiv, 2021 [171].

7.1 Transmon Qubit

The following derivations are adapted from those found in [172]. Starting from a classical inductor and capacitor circuit, usually called an LC circuit, with capacitance C and inductance L, we can write its Lagrangian in terms of the capacitive and inductive energy,

$$\mathcal{L} = \frac{LI^2}{2} - \frac{Q^2}{2C} \tag{7.1}$$

$$=\frac{L\dot{Q}^2}{2} - \frac{Q^2}{2C} \tag{7.2}$$

1411

1413

where we have additionally used charge conservation to replace the current term, I, with the time derivative of the charge, Q, in the last line.

The momentum conjugate to the charge is given by

$$\Phi = \frac{\delta \mathcal{L}}{\delta \dot{Q}} = LI,\tag{7.3}$$

which is the flux through the inductor. We can then write the Hamiltonian in terms of the charge, momentum conjugate and the Lagrangian,

$$H_{LC} = \Phi \dot{Q} - \mathcal{L} = \frac{Q^2}{2C} + \frac{\Phi^2}{2L},$$
 (7.4)

where Q and Φ are the corresponding charge on the capacitor and flux through the inductor, respectively. Eq. 7.4 looks fairly similar to Eq. 5.7, and we can perform the same treatment of raising the canonically conjugate variables into operators, $Q \to \hat{Q}$ and $\Phi \to \hat{\Phi}$. At this point, it is helpful to use the operators more commonly associated with superconducting transmons, which are the Cooper-pair number operator, n = Q/2e, and the reduced flux, $\phi = 2e\Phi/\hbar$, sometimes also referred to as the phase. This allows us to work with the commutation relation $[\phi, n] = i$, and recast our Hamiltonian (Eq. 7.4) as

$$H = 4E_c n^2 + \frac{1}{2}E_L \phi^2, \tag{7.5}$$

where $E_C = \frac{e^2}{2C}$ is the charging energy of a Cooper-pair and $E_L = \frac{\hbar L}{4e^2}$ is the inductive energy of a quanta of superconducting magnetic flux. By treating ϕ as the generalised position coordinate and n as the generalised momentum, we reformulate Eq. 7.5 in terms of the familiar ladder operators,

$$H = \hbar\omega \left(a^{\dagger} a + \frac{1}{2} \right), \tag{7.6}$$

with $\omega = \frac{1}{\sqrt{LC}}$. Note that we have used ϕ as the generalised position coordinate while Eq. 7.3 suggests that it should be the generalised momentum. This is done so that the commutation relation, $[\phi, n] = i$, remains consistent with that for x and p (Eq. 5.10).

We can also express the number and phase operators as functions of the raising and lowering operators

$$n = in_{zpf}(a - a^{\dagger}), \tag{7.7}$$

$$\phi = \phi_{zvf}(a + a^{\dagger}),\tag{7.8}$$

where $n_{zpf} = (\frac{E_L}{32E_C})^{1/4}$ and $\phi_{zpf} = (\frac{2E_C}{E_L})^{1/4}$ are the zero-point fluctuations of the charge and phase, analogous to that for quantum harmonic oscillators in position-momentum space.

The LC circuit can in principle be used as a qubit system with precise control of the excitations. However, in practice, additional steps have to be taken in order to confine the system to only the ground and first excited level. This is usually achieved by introducing anharmonicity to the system, disrupting the uniform spacings between the energy levels so that the radiation that excites the ground to the first excited state cannot excite the second to the third excited state and so forth. This is done by introducing a Josephson junction that acts as a nonlinear element to the circuit. A Josephson junction consists of two superconductors separated by a barrier, giving rise to the Josephson relations,

$$I = I_c \sin \varphi, \tag{7.9}$$

$$\frac{\partial \varphi}{\partial t} = \frac{2e}{\hbar}V,\tag{7.10}$$

where V is the potential difference across the junction and I_c is the critical current of the Josephson junction, characterising the maximum amount of current allowed to coherently cross the junction. This critical current

1431

1439

1440

1442

is often written in terms of the Josephson energy, E_J , which is the energy required for a Cooper pair to tunnel across the junction as $I_c = \frac{2eE_J}{\hbar}$.

Using the Josephson relations, Eq. 7.10, we can work out the energy stored in the junction by treating it as an inductor and evaluating the integral

$$U_L = \int IVdt \tag{7.11}$$

$$= \int I_c \sin \varphi \frac{\hbar}{2e} \frac{\partial \varphi}{\partial t} dt \tag{7.12}$$

$$=E_{J}\int\sin\varphi d\varphi\tag{7.13}$$

$$= -E_J \cos \varphi. \tag{7.14}$$

Replacing the inductive element with a Josephson junction, we then obtain a modified Hamiltonian,

$$H' = 4E_C n^2 - E_J \cos \varphi, \tag{7.15}$$

where we update $E_C = \frac{e^2}{2(C_s + C_J)}$ to also include the capacitive contribution from the junction. The presence of the nonlinear cosine term introduces anharmonicity and creates non-equidistant energy levels. The behavior of the anharmonicity is characterised by the ratio E_J/E_C , and for $E_J \gg E_C$, often achieved by using a large capacitor for the shunt, we operate in what is often known as the "transmon" regime. In this limit, expanding the cosine term in its power series gives us

$$E_J \cos \varphi = 1 - \frac{1}{2} E_J \varphi^2 + \frac{1}{24} E_J \varphi^4 + \mathcal{O}(\varphi^6),$$
 (7.16)

from which we see that only keeping the quadratic term gives us Eq. 7.5, while the quartic term (and beyond) gives us the necessary anharmonicity. Keeping the terms up to fourth order, we can rewrite Eq. 7.15 as

$$H' = -4E_C n_{zpf}^2 (a^{\dagger} - a)^2 - E_J (1 - \frac{1}{2} \phi_{zpf}^2 (a + a^{\dagger})^2 + \frac{1}{24} \phi_{zpf}^4 (a + a^{\dagger})^4 + \dots)$$
 (7.17)

$$\approx \sqrt{8E_C E_J} (a^{\dagger} a + \frac{1}{2}) - E_J - \frac{E_C}{12} (a^{\dagger} + a)^4, \tag{7.18}$$

where we have used the relation $8E_C n_{zpf}^2 = E_J \phi_{zpf}^2 = \sqrt{2E_C E_J}$ in simplifying the expression. We neglect the constant terms as we are only interested in the energy level spacings and ignore the terms that do not preserve particle number to finally arrive at the transmon Hamiltonian.

$$H_{tr} = \omega_0 a^{\dagger} a + \frac{\delta}{2} \left((a^{\dagger} a)^2 + a^{\dagger} a \right), \tag{7.19}$$

with $\omega_0 = \sqrt{8E_CE_J}$ and $\delta = -E_C$. It can be seen with some re-arrangement that we now have an energy ladder with frequency $\omega = \omega_0 + \frac{\delta}{2}$, with an anharmonic quadratic term $a^\dagger a a^\dagger a$. Notably, the anharmonic term does not alter the ground or first excited state but does affect the higher lying energy states, allowing us to use the transmon system as a qubit with frequency $\omega_q = \omega$.

7.2 Tardigrades

The phylum of tardigrada consist of microscopic eight-legged segmented invertebrates that typically grow to an adult length of 50-1200 μ m [173]. Tardigrades are one of the most resilient multi-cellular eukaryotes that we know of, with many of species possessing extraordinary survival capabilities [174], being able to survive in miliKelvin temperatures [175] and low Earth orbit pressures [176]. This is achieved via a latent state of life

known as cryptobiosis [174,177], induced by extreme physicochemical conditions like anhydrobiosis (desiccation), anoxybiosis (oxygen depletion), chemobiosis (high toxicant concentrations), cryobiosis (extremely low temperatures) and osmobiosis (high solute concentration) [178]. Specifically, during desiccation, tardigrades revert to an ametabolic state, known as a "tun" by withdrawing its legs and contracting longitudinally into a cuboid structure. This state can be reversed by reintroducing the tardigrade into water.

In our experiments, we have used specimens of a Danish population of Ramazzottius varieornatus Bertolani and Kinchin, 1993 (Eutardigrada, Ramazzottiidae), frequently found in transient freshwater habitats. R. 1450 varieornatus requires itself encased in a film of water to remain in its active form. Adult specimens were 1451 collected on February 2018 from a roof gutter in Nivå, Denmark (N 55°56.685', E 12°29.775'). The roof gutter 1452 sample, containing the tardigrades, was frozen under wet conditions and stored at -20° C until October 2020, 1453 when the sample was thawed, diluted in ultrapure water (Millipore Milli-Q[®] Reference, Merck, Darmstadt, 1454 Germany) and examined for active adult tardigrades with the help of a stereomicroscope. Single adult tardigrades were removed from the sample with the aid of hand pulled glass pasteur pipettes and desiccated 1456 on filter paper substrates for use in the experiments. 1457

An exemplary photo of an adult R. varieornatus and its tun state is shown in Fig 7.1. Typically, the adult forms have lengths of 200-450 μ m, while the tun states are 100-150 μ m. From here on, any mention of tardigrade refers to this particular species.

7.3 Experimental Overview

1468

1469

1470

1471

1472

1473

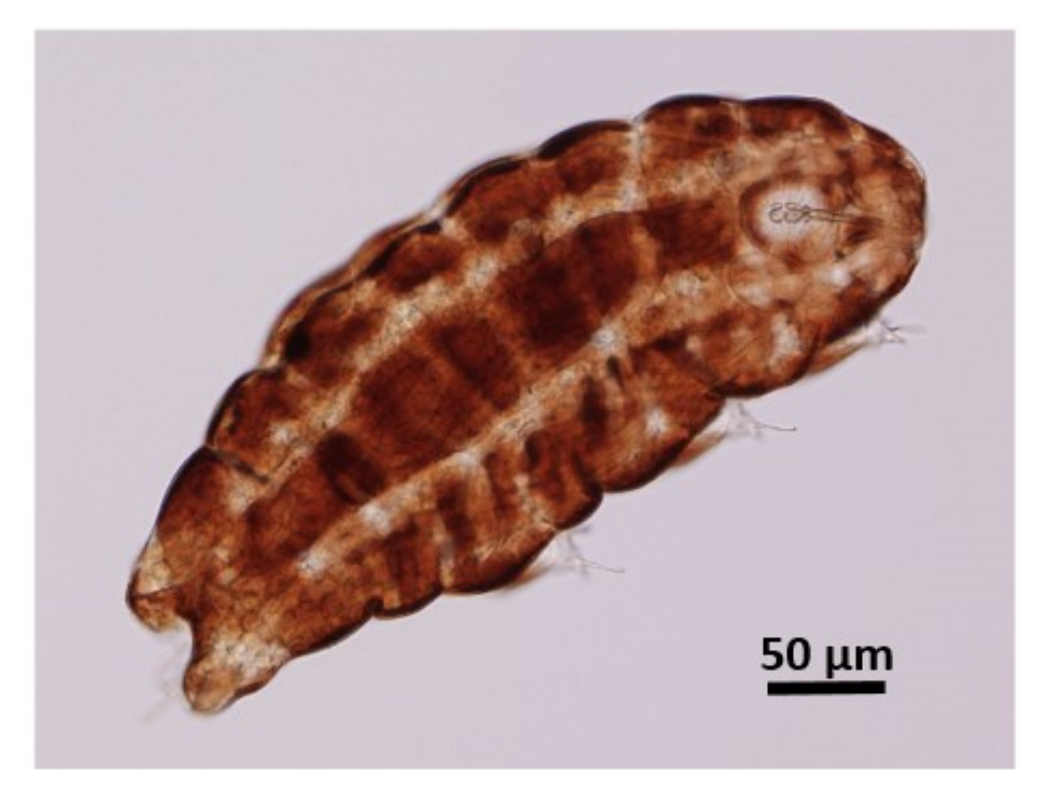
In our experiment, a single R. varieornatus tardigrade in the tun state is placed in between the shunt capacitor pads of a transmon qubit chip which we designate as 'qubit B', refer to Fig. 7.2. Together with a second similar qubit chip, the two transmon qubits were mounted back to back inside an oxygen-free, high thermal conductivity copper 3D microwave cavity with a TE_{101} frequency of 4.521 GHz. The separation between the qubits was about 1 mm, approximately twice the thickness of the silicon chips they are embedded on. The frequency of qubit A is $f_A = 3.048$ GHz and qubit B $f_B = 3.271$ GHz without the tardigrade tun.

The cavity, together with the qubits and tardigrade tun, was placed in a Helium dilution fridge, and brought to base temperatures below 10 mK and pressures below 6×10^{-6} mbar over about 3 days, after which measurements on the qubit-tardigrade system were performed. It should be noted that in total, the tardigrade spent 420 hours in the fridge, after which it was revived successfully in water when brought back to room temperatures and pressures. This marks the most extreme and prolonged exposure to low temperatures and pressures that a tardigrade has been recorded to survive.

The full experiment can be split into two parts: the first involves (i) readout of qubit A and composite tardigrade-qubit B frequencies, and the second involves (ii) preparation of a highly entangled state between the three systems. We will first mention the results of (i) and proceed to discuss the models used to explain the observation, and then continue in a similar fashion for (ii).

7.4 Frequency Readout Experiment

Upon performing frequency readouts on qubit A and B, the frequency of qubit A was unchanged, but the frequency of qubit B was shifted low by 8 MHz, to $f'_B = 3.263$ GHz.



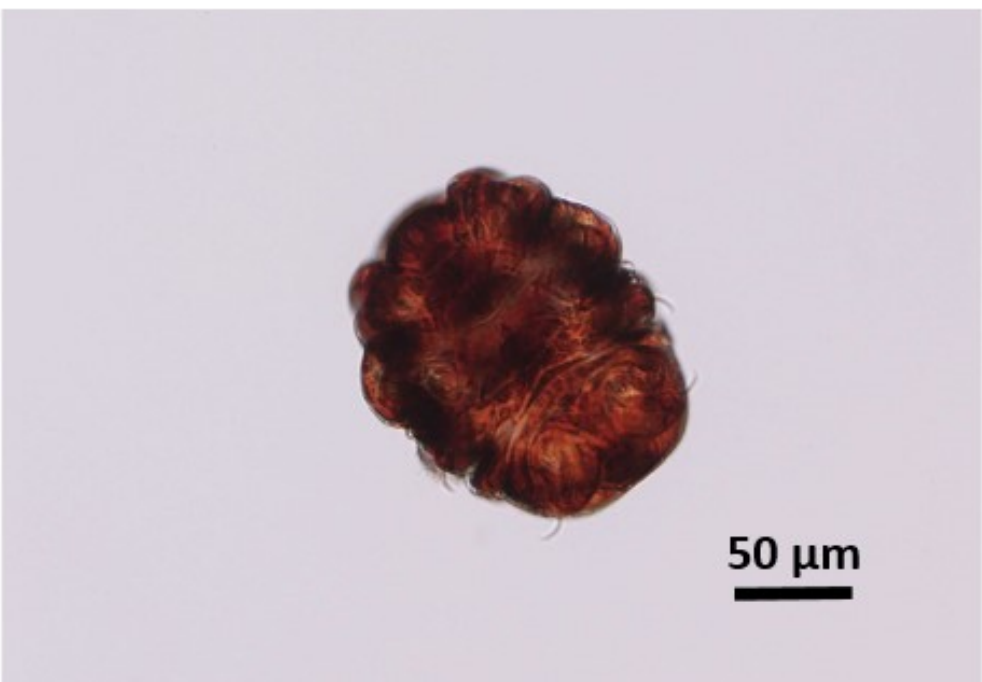


Fig. 7.1: Top: Active adult tardigrade. Bottom: Tardigrade in the tun state. Photographs courtesy of Nadja Møbjerg.

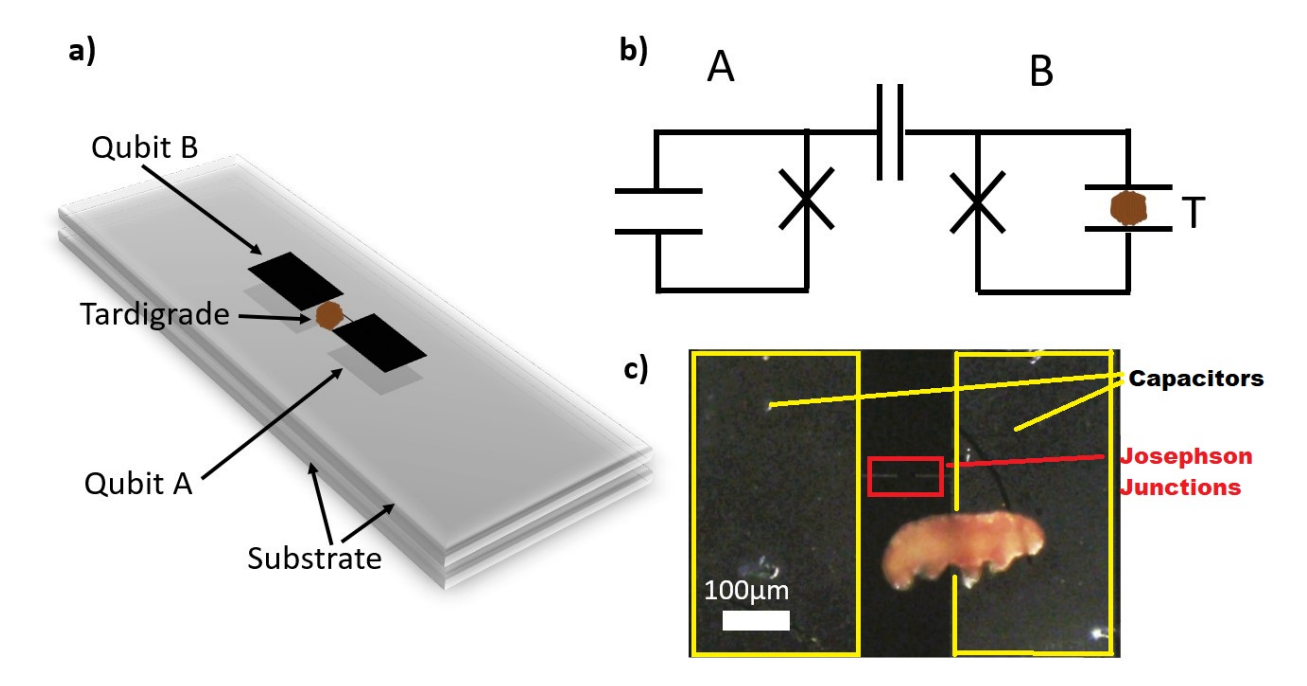


Fig. 7.2: Sketch of the experiment. a) Tardigrade in the tun state is placed on qubit B, between the capacitor plates, with qubit A on the underside, separated by a distance of about 1 mm. b) Circuit diagram of the system of qubit A, qubit B and the tardigrade. c) Magnified photograph of the tardigrade in the active state on the qubit chip for illustration purposes. A tun was used in the actual experiments.

7.4.1 Dielectric shift

1481

1482

1484

1485

1486

1488

1490

1491

1492

1493

By placing a tardigrade in between the capacitor plates of the transmon chip, the tardigrade acts as a dielectric and increases the effective capacitance of the qubit. While we do not know the exact permittivity of the tardigrade in the tun state, it is clearly larger than that of the vacuum so that the relative permittivity, $\epsilon_r > 1$, will increase the capacitance, $C' = \epsilon_r C$. Consequently, the charging energy is lowered and the qubit frequency is shifted down (see Fig. 7.3). Realistically, this shift can also be attributed to the aging of the Josephson junctions, together with the addition of the tardigrade. However, the measured frequency shift corresponds to tardigrade dielectric constant of $\epsilon_r \approx 4$ which is in the lower range of the dielectric constants for proteins (between 4 to 30 [179]), indicating that the contribution from the aging effect is small, in agreement with measurements on qubit A.

A drawback of this dielectric model is that it treats the tardigrade as a macroscopic effective medium and is unable to discern the microscopic details of the tardigrade system. Therefore, we will need a different microscopic model to explore the tardigrade system.

7.4.2 Transmon qubit subspace

In our experimental setup, the transmon can be operated as a qubit with only the ground state and first excited state accessible. Thus, it is sufficient to reduce the description of the transmon from an anharmonic oscillator to a two level system,

$$H_{tr} = \frac{\hbar\omega_q}{2}\sigma_z,\tag{7.20}$$

where ω_q is the corresponding frequency difference between the ground and excited state.

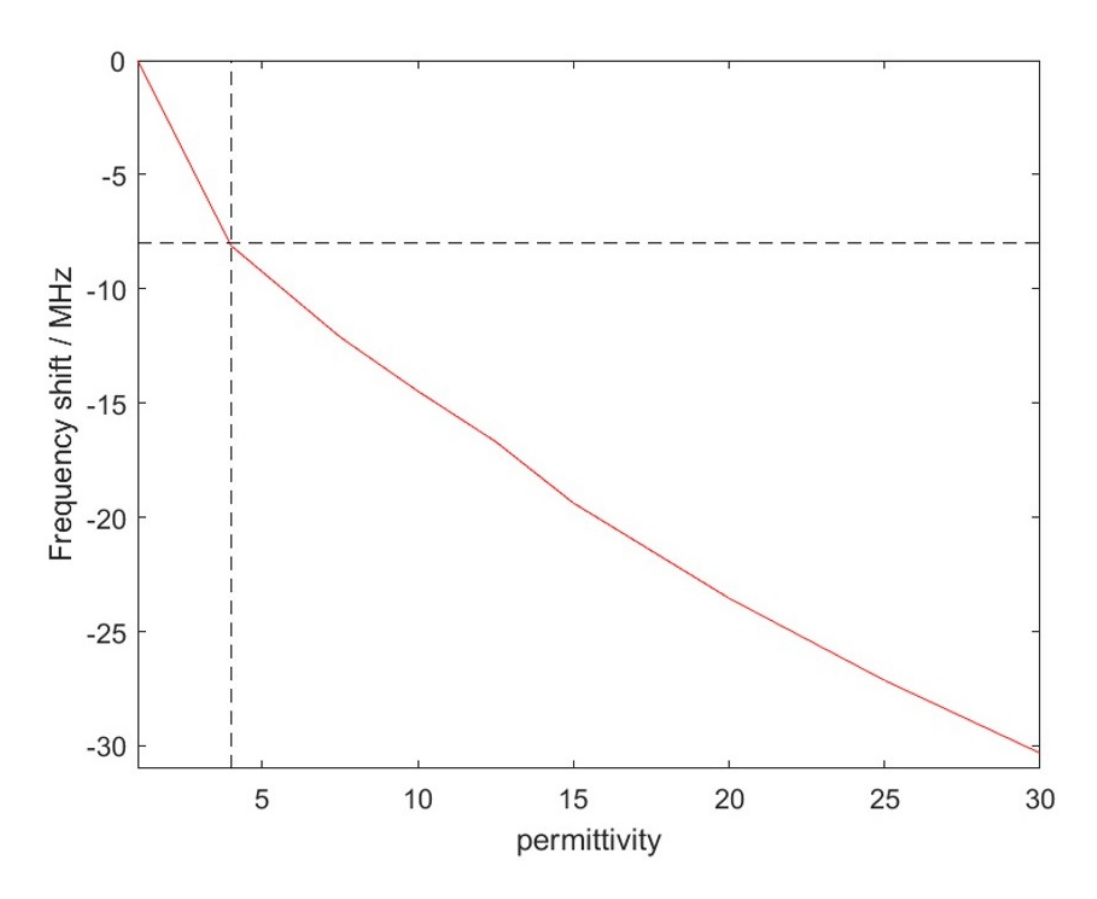


Fig. 7.3: Frequency shift as a function of the permittivity of the tardigrade, modeled as a dielectric cube. The horizontal dashed line marks the experimentally observed frequency shift, with the vertical dashed line indicating the permittivity required to produce such a shift ($\epsilon \approx 4$).

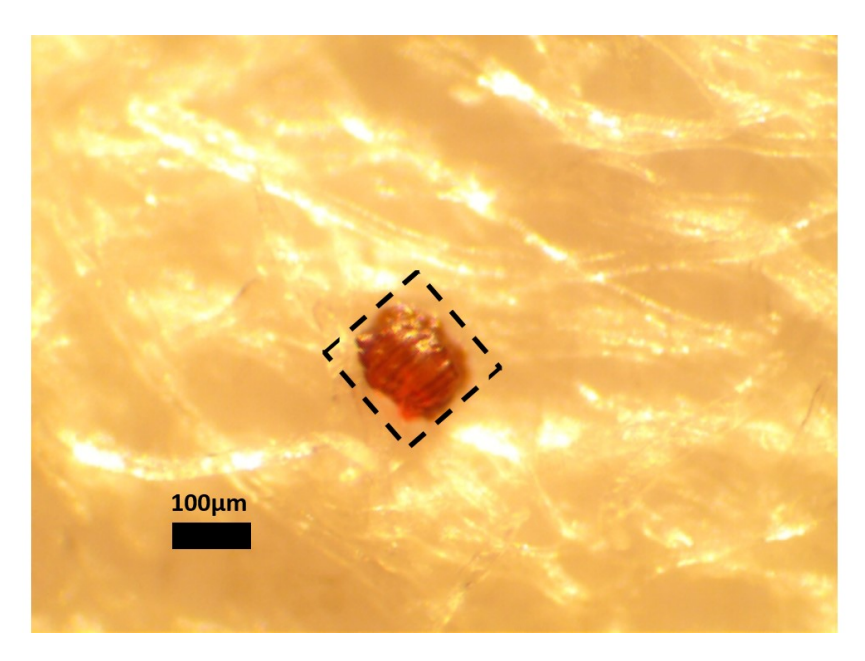


Fig. 7.4: Picture of the tardigrade in the tun state attached to filter paper. A small square section of length approximately 150 μ m, together with the tun, was cut out and used in the experiments.

7.4.3 Tardigrade as a collection of harmonic oscillators

Similar to the Debye model, the tardigrade can also be treated as a collection of N harmonic oscillators, each with frequency $\omega_1, \omega_2, ..., \omega_N$ that need not be equal. The Hamiltonian of the tardigrade system therefore reads:

$$H_{tardigrade} = \sum_{i=1}^{N} \hbar \omega_i a_i^{\dagger} a_i, \tag{7.21}$$

where the subscripts label the oscillator modes.

In the experiment, the tardigrade was still attached to a square piece of filter paper approximately 150 μ m in length, see Fig. 7.4. This was necessary as extraction from the filter paper caused irreversible damage to the tardigrade cuticle, hindering their ability to revive in water. This filter paper contributes minimally to our model as it is sufficiently displaced from the transmon plane, where most of the interactions between the qubit and transmon take place. Further elaborations can be found in the following section discussing the interactions.

7.4.4 Qubit-Tardigrade system

The combined system is similar to the Tavis-Cummings model described in Chapter 5 (one oscillator and many two-level systems). The twist here is that we have oscillators and one two-level system. Namely, the qubit plays the role of the TLS, with the tardigrade as a multimode quantum harmonic oscillator. As the coupling term is symmetric between the cavity and atom, the cavity and atom role can be interchanged without affecting the interaction term. The coupling is achieved via dipole-dipole interaction between the electric field produced by the transmon capacitor plates and the charges inside the tardigrade. Due to the geometry of the transmon chip, the electric fields are mostly confined to the plane of the substrate and close to the Josephson junctions. In contrast, the tardigrade tun resembles a cuboid structure of height $100~\mu m$ and only a very small portion of the tardigrade experiences the qubit electric field. We verify this by using ANSYS Maxwell to simulate the electric field produced by a 20~mV excitation across the shunt

1522

1523

1524

1526

1527

1528

1530

1532

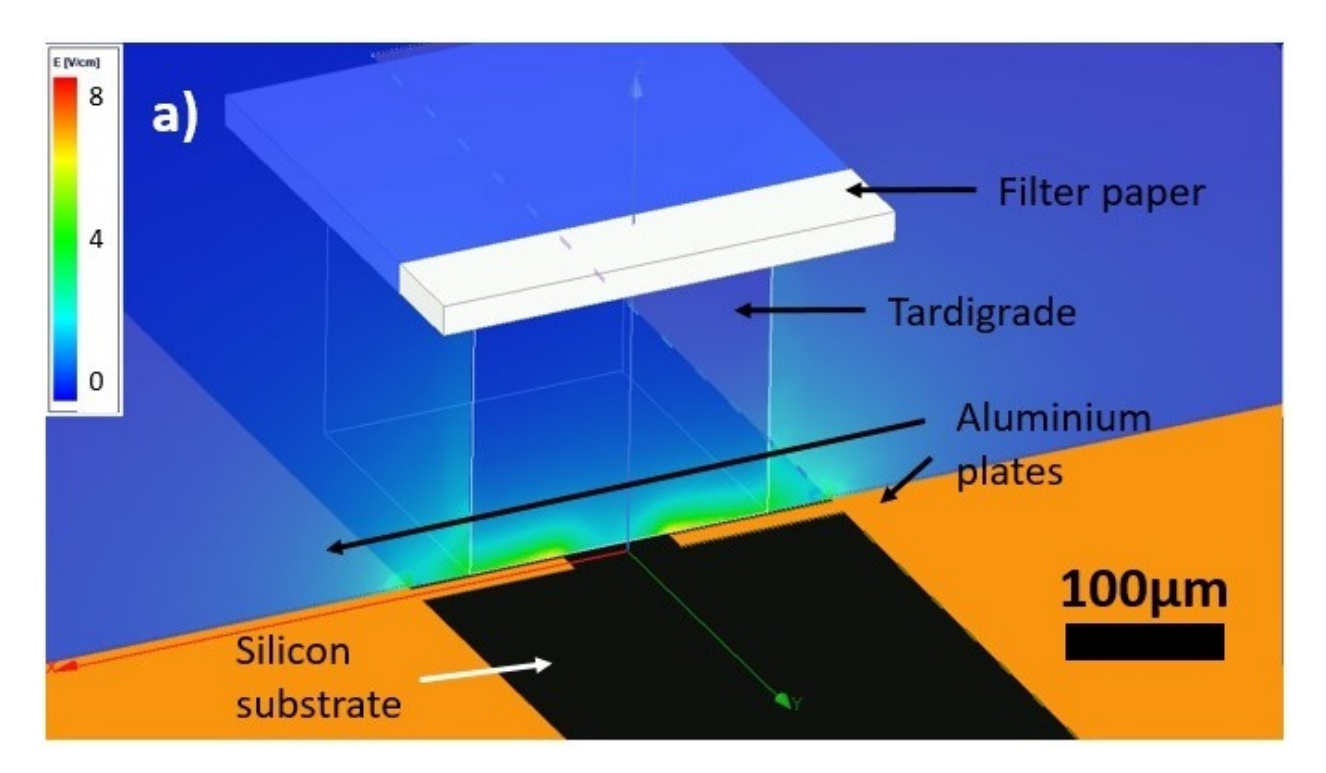


Fig. 7.5: Numerical simulations of the electric field along the surface of the tardigrade ($\epsilon = 4$) for an exemplary potential difference of 20 mV across the shunt capacitor plates.

capacitor plates of the transmon, with the tardigrade tun slightly displaced from the axis. The tardigrade was simulated with a dielectric constant of 4, with a 150 μ m square filter paper with dielectric constant of 4.5 on its top. The electric field is highly localised around the capacitor plates and falls off quickly with distance. The numerical simulation of the electric field along the surface of the tardigrade is shown in Fig. 7.5. The evanescent field around the capacitor plates reach values around 8 V/cm while the corner regions close to the plates reach on about 4 V/cm, suggesting that the interactions between the qubit and tardigrade are weak.

The Hamiltonian for this multiple oscillator-qubit system has a form similar to Eq 6.45,

$$H_{MOQ} = \hbar \sum_{i} \omega_{i} a_{i}^{\dagger} a_{i} + \hbar \omega_{a} \sigma_{z} + g \sum_{i} (a_{i}^{\dagger} \sigma_{-} + a_{i} \sigma_{+}), \tag{7.22}$$

where the sums are over the oscillator modes. It should be noted that due to the complexity of the tardigrade as a multicellular organism containing a large collection of molecules and thereby oscillator modes, we are unlikely operating in the near resonance regime and thus it is not entirely appropriate to take the RWA. However, the RWA greatly simplifies the problem and is in general a good approximation for weak coupling strengths.

For a weak coupling, we can apply quantum perturbation theory to obtain solutions for H_{MOQ} by first splitting it into an unperturbed Hamiltonian, H_0 , and the perturbation, V:

$$H_0 = \hbar \sum_i \omega_c^{(i)} a_i^{\dagger} a_i + \hbar \omega_a \sigma_z, \tag{7.23}$$

$$V = \sum_{i} (a_i^{\dagger} \sigma_- + a_i \sigma_+), \tag{7.24}$$

so that $H_{MOQ}=H_0+gV$. The eigenstates of H_0 are the number states of the form $|0\rangle_a|n_1\rangle|n_2\rangle...|n_N\rangle$

and $|1\rangle_a |n_1\rangle |n_2\rangle ... |n_N\rangle$ with the corresponding eigenenergies of $\pm \frac{\omega_q}{2} + \sum_{i=1}^N n_i \omega_i$, where the subscripts in the oscillator number states enomerates their mode. The eigenenergies up to the second order are given by,

$$E_m = E_m^{(0)} + gE_m^{(1)} + g^2 E_m^{(2)}, (7.25)$$

with the zeroth order term being the eigenenergies of the unperturbed Hamiltonian, H_0 ,

$$H_0 \left| \psi_m^{(0)} \right\rangle = E_m^{(0)} \left| \psi_m^{(0)} \right\rangle \tag{7.26}$$

with first-order correction given by,

$$E_m^{(1)} = \left\langle \psi_m^{(0)} \middle| V \middle| \psi_m^{(0)} \right\rangle, \tag{7.27}$$

and the second-order correction.

$$E_m^{(2)} = \sum_{n \neq m} \frac{\left| \left\langle \psi_n^{(0)} \middle| V \middle| \psi_m^{(0)} \right\rangle \right|^2}{E_m^{(0)} - E_n^{(0)}}.$$
 (7.28)

1540 Consequently, the eigenstates up to second order are,

$$\left|\psi_{m}\right\rangle = \left|\psi_{m}^{(0)}\right\rangle + g\left|\psi_{m}^{(1)}\right\rangle + g^{2}\left|\psi_{m}^{(2)}\right\rangle,\tag{7.29}$$

with the first and second order corrections given by,

$$\left|\psi_{m}^{(1)}\right\rangle = \sum_{k \neq m} \frac{\left\langle \psi_{k}^{(0)} \middle| V \middle| \psi_{m}^{(0)} \right\rangle}{E_{m}^{(0)} - E_{k}^{(0)}} \left| \psi_{k}^{(0)} \right\rangle,$$
 (7.30)

and.

$$\left|\psi_{m}^{(2)}\right\rangle = \sum_{k \neq m} \sum_{j \neq m} \frac{\left\langle \psi_{k}^{(0)} \middle| V \middle| \psi_{j}^{(0)} \right\rangle \left\langle \psi_{j}^{(0)} \middle| V \middle| \psi_{m}^{(0)} \right\rangle}{(E_{m}^{(0)} - E_{k}^{(0)})(E_{m}^{(0)} - E_{j}^{(0)})} \left|\psi_{k}^{(0)}\right\rangle - \sum_{k \neq m} \frac{\left\langle \psi_{k}^{(0)} \middle| V \middle| \psi_{m}^{(0)} \right\rangle \left\langle \psi_{m}^{(0)} \middle| V \middle| \psi_{m}^{(0)} \right\rangle}{(E_{m}^{(0)} - E_{k}^{(0)})^{2}} \left|\psi_{k}^{(0)}\right\rangle$$

$$(7.31)$$

$$-\frac{1}{2} \sum_{k \neq m} \frac{\left| \left\langle \psi_k^{(0)} \middle| V \middle| \psi_m^{(0)} \right\rangle \right|^2}{(E_m^{(0)} - E_k^{(0)})^2} \left| \psi_m^{(0)} \right\rangle. \tag{7.32}$$

While this system is infinite dimensional, due to the weak coupling to the embedding microwave cavity, we can only probe the two states closest to the qubit ground, $\left|\psi_0^{(0)}\right> = \left|0\right> \left|0\right> \dots \left|0\right>$, and excited states, $\left|\psi_1^{(0)}\right> = \left|1\right> \left|0\right> \dots \left|0\right>$. The perturbation V conserves excitation number, mapping $\left|\psi_0^{(0)}\right>$ to 0, since the ground state remains unaffected by all the perturbation terms,

$$E_0 = E_0^{(0)} = -\frac{\hbar\omega_q}{2},\tag{7.33}$$

1546 and,

$$|\psi_0\rangle = |\psi_0^{(0)}\rangle = |0, 0, 0, ..., 0\rangle,$$
 (7.34)

consistent with the Tavis-Cummings model. In contrast, V maps $|\psi_1^{(0)}\rangle$ to a superposition of other orthogonal eigenstates with excitation number of 1,

$$V\left|\psi_{1}^{(0)}\right\rangle = |0, 1, 0, ..., 0\rangle + |0, 0, 1, ..., 0\rangle + ... + |0, 0, 0, ..., 1\rangle.$$
 (7.35)

Using the relation in Eq. 7.35, we see from Eq. 7.27 and 7.28 that $E_1^{(1)}$ vanishes due to the orthogonality of the number states, while $E_1^{(2)}$ reads,

$$E_1^{(2)} = \left(\frac{\hbar}{4}\right) \sum_{i}^{N} \frac{1}{\omega_q - \omega_i}.$$
 (7.36)

Writing the detuning $\delta_j = \omega_q - \omega_j$, we have the energy of the first excited state as,

$$E_1 = E_1^{(0)} + gE_1^{(1)} + g^2E_1^{(2)} (7.37)$$

$$=\frac{\hbar\omega_q}{2} + \left(\frac{\hbar g^2}{4}\right) \sum_{i}^{N} \frac{1}{\delta_i} \tag{7.38}$$

which translates to an observed transition frequency of

$$\Delta f = \frac{E_1 - E_0}{h} \tag{7.39}$$

$$= \frac{1}{2\pi} \left(\omega_q + \frac{g^2}{4} \sum_i^N \frac{1}{\delta_i} \right). \tag{7.40}$$

We can do the same for the correction terms of the eigenstates to get

$$|\psi_1\rangle = \cos\frac{\theta}{2}|1\rangle|\bar{0}\rangle + \sin\frac{\theta}{2}|0\rangle|\phi\rangle,$$
 (7.41)

where $\cos \frac{\theta}{2} = 1 - (g^2/8) \sum_j (1/\delta_j^2)$ and we have used the notations for the tardigrade states such that $|\bar{0}\rangle = |0,...,0\rangle$ and

$$|\phi\rangle = c_1 |1, 0, ..., 0\rangle + ... + c_N |0, ..., 0, 1\rangle$$
 (7.42)

for suitable coefficients $c_1, ..., c_N$. Their exact form is not important, with the key point being that $|\phi\rangle$ is orthogonal to $|\bar{0}\rangle$. The orthogonality implies that in this model, the tardigrade effectively behaves as another two-level system, with the ground state $|\bar{0}\rangle$ and an excited stated $|\phi\rangle$.

7.5 Preparation of Bell state

1557

1558

1559

1560

1561

1562

1563

1565

1566

1567

1568

1569

1570

1572

In the second part of the experiment, a Bell state between qubit A and qubit B-tardigrade system was produced and reconstructed using quantum state tomography. To generate the Bell state, a sequence of pulses: Hadamard followed by a controlled-NOT (cNOT) gate was used, see Fig. 7.6. As there was no way to directly address the tardigrade system alone, all pulses and measurements could only be applied to the four-dimensional subspace of qubit A and the dressed state of the joint qubit B-tardigrade system. The cNOT gate was implemented via Speeding up Waveforms by Inducing Phases to Harmful Transitions (SWIPHT) protocol, described in [180, 181]. The resulting pulse sequence ideally produces the Bell state $|\psi^{+}\rangle = \frac{1}{\sqrt{2}}(|0_A, e_{BT}\rangle + |1_A, g_{BT}\rangle)$, which was then verified using quantum state tomography, as shown in Fig. 7.6. The tomography was performed by applying 16 different combinations of single qubit gates on qubit A and the joint qubit B-tardigrade system, followed by simultaneous readout of both states from the cavity [182]. In order to constrain the density matrix to have the physical properties of being normalised and positive semi-definite, a maximum likelihood estimation was utilised [183], producing an expected density matrix with state fidelity of F = 82% [184]. This expected density matrix, ρ_{exp} is shown in Fig. 7.7, together with the theoretical density matrix for ideal implementations of the quantum gates. From ρ_{exp} , we can reconstruct the density matrix of the full qubit A, qubit B and tardigrade system using the dressed states derived in Eq. 7.42. The reconstructed density matrix, in the order $\mathcal{H}_A \otimes \mathcal{H}_B \otimes \mathcal{H}_T$, depends on the

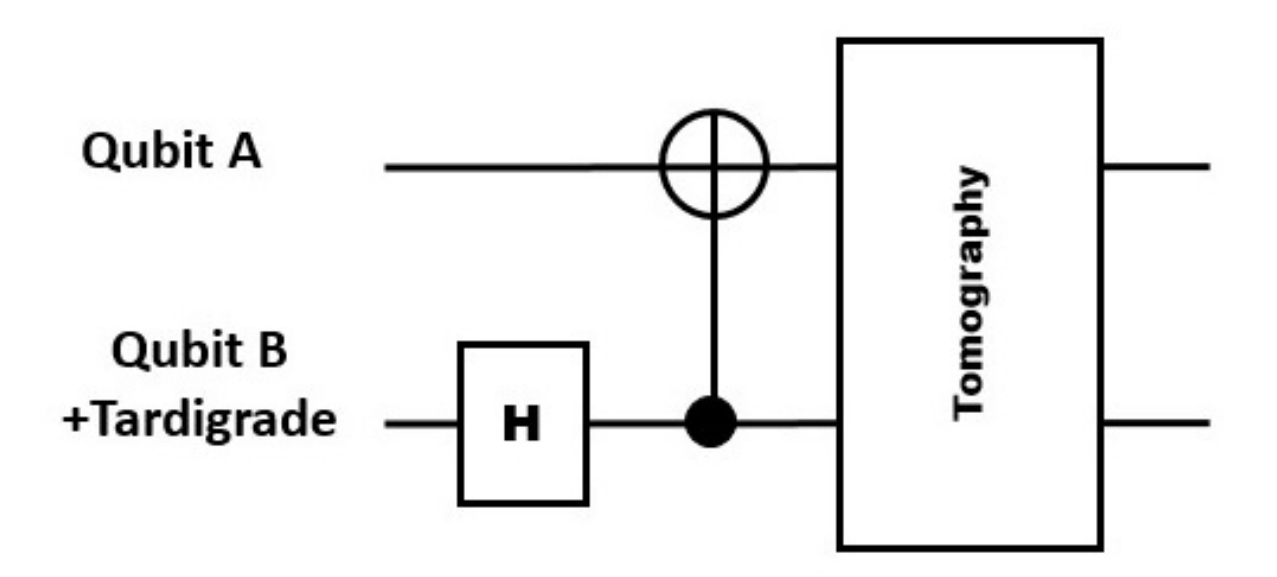


Fig. 7.6: Sequence of quantum gates used to generate the maximally entangled Bell state $|\psi^{+}\rangle$ between qubit A and the composite tardigrade-qubit B system.

coupling strength, θ , between qubit B and the tardigrade, and reads,

where the ρ_{ij} terms are the matrix elements of ρ_{exp} . Due to assumptions that the system is not energetic enough for simultaneous excitation of qubit B and the tardigrade, ρ_{ABT} has 28 vanishing matrix elements corresponding to terms containing double excitations in the qubit B-tardigrade system, i.e. $|01\underline{1}\rangle$, $|11\underline{1}\rangle$, $|01\underline{1}\rangle$, $|11\underline{1}\rangle$, $|111\rangle$

7.5.1 Entanglement quantifiers

To better understand the entanglement within the tripartite system, we have to choose an entanglement monotone to quantify the entanglement. We utilise the so-called tangles in a similar fashion as defined in [185]. For a bipartite system, the well-known negativity [186] is given by

$$N_{X:Y} = ||\rho_{XY}^{T_X}|| - 1, (7.44)$$

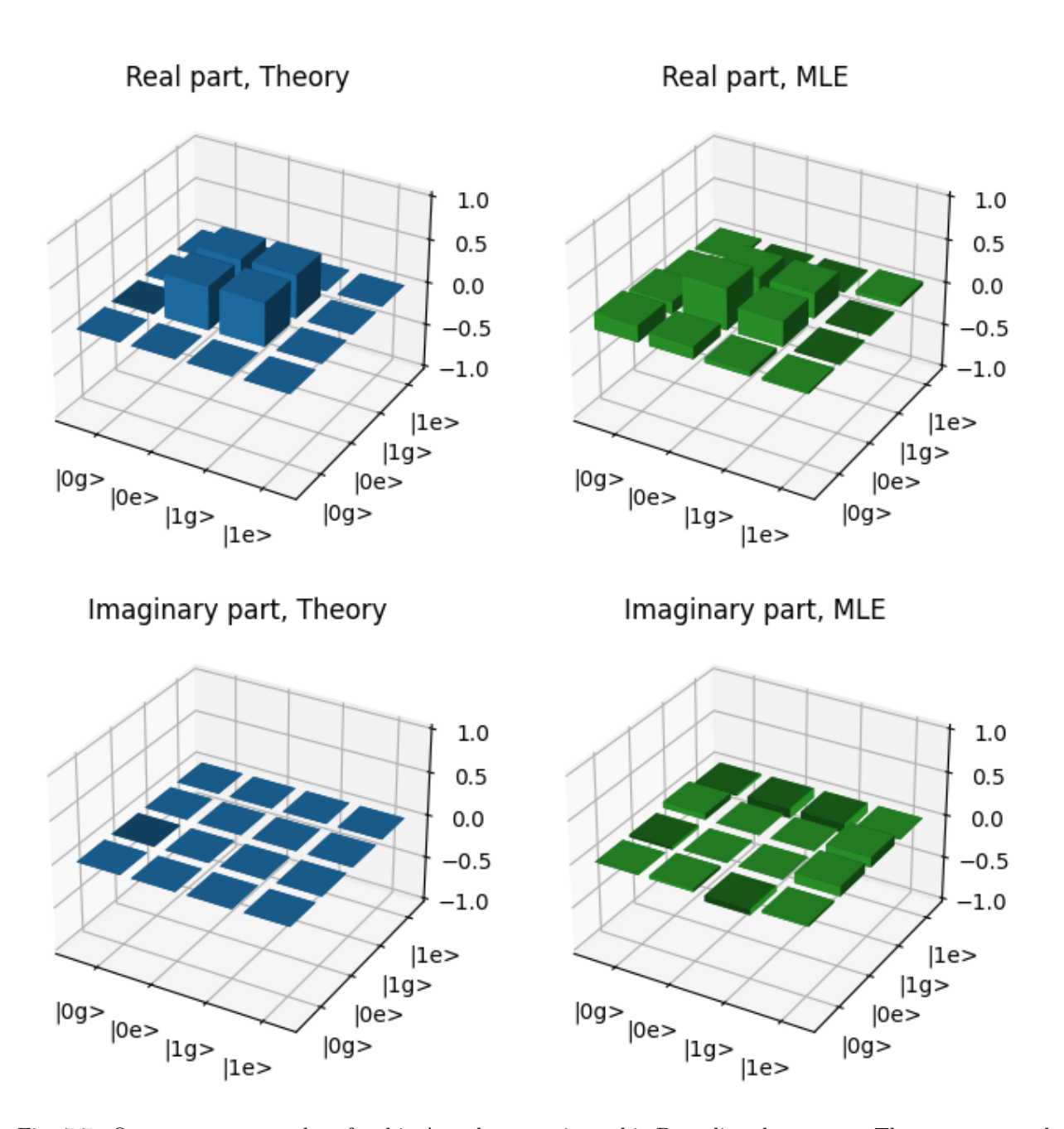


Fig. 7.7: Quantum tomography of qubit A and composite qubit B-tardigrade system. The reconstructed density matrix via maximum likelihood estimation has a fidelity of 82%.

where $||M|| = \text{Tr } \sqrt{M^{\dagger}M}$ is the trace norm of the square matrix M, while the T_X superscript represents the partial transpose operation over the subsystem X. If we were to extend Eq. 7.44 to a tripartite system, the negativity would encompass both bipartite and genuine tripartite (irreducible to pairwise) entanglement. To account for this, we define the π -tangle,

$$\pi = \frac{\pi_A + \pi_B + \pi_C}{3},\tag{7.45}$$

where

$$\pi_A = N_{A:(BC)}^2 - N_{AB}^2 - N_{AC}^2, \tag{7.46}$$

$$\pi_B = N_{B:(AC)}^2 - N_{BA}^2 - N_{BC}^2, \tag{7.47}$$

$$\pi_C = N_{C:(AB)}^2 - N_{CA}^2 - N_{CB}^2, \tag{7.48}$$

such that the pairwise entanglement contributions are excluded from the π -tangle. We plot the π -tangle and bipartite negativities in Fig. 7.8. As a sanity check, we see that the bipartite entanglement between the tardigrade and the subsystems, $N_{T:(AB)}$, $N_{A:T}$ and $N_{B:T}$, as well as the π -tangle start off close to zero and increase with the coupling strength. The bipartite entanglement between qubit A and the qubit B-tardigrade subsystem, $N_{A:(BT)}$, is close to 0.5 (negativity maximum) because the prepared state is close to the Bell-state $|\psi^{+}\rangle$ which is a maximally entangled state. From our models of the dressed states, we have demonstrated entanglement in the qubit A-qubit B-tardigrade tun system, even though qubit A and the tun do not locally influence each other, as long as we have non-zero coupling strength.

7.6 Bystander model

It is still technologically challenging to directly address or probe the tardigrade system alone. As such, the quantum description of the tardigrade was required to indirectly infer the entanglement of the tardigrade with qubits A and B. This leaves some room for doubt on whether entanglement was achieved in the experiment. Here, we discuss an alternative model that is semi-classical in nature and show that it leads to some contradictory results.

In this model, which we will call the bystander model, the tardigrade acts as a dielectric and has no interaction with qubit B, like a bystander. The ground and excited states are then $|g\rangle = |0_d\rangle |d_0\rangle$ and $|e\rangle = |1_d\rangle |d_1\rangle$, where the $|d_i\rangle$ are the tardigrade states dependent on the state of qubit B and subscripts d for the qubit energy levels are to indicate that these are shifted due to the different dielectric properties and are not the same levels as in the bare qubit case. The exact intricacies and form of these new levels are unimportant for this discussion, while the use of quantum notation for the tardigrade is necessitated by the unambiguously quantum nature of the qubit. This is different from the quantum model where the ground and excited states are dressed states due to the interactions between the qubit and tardigrade. At this juncture, reading a frequency shift of qubit A does not imply any entanglement yet. In the next stage of the experiment, we generate a Bell state between qubit A and the composite qubit B-tardigrade, where the joint state is $\frac{1}{\sqrt{2}}(|0\rangle|e\rangle + |1\rangle|g\rangle$), with the first ket describing qubit A. The only way for the tardigrade degree of freedom to remain separable (no entanglement) from the qubit subspaces is for $|d_0\rangle = |d_1\rangle = |d\rangle$, i.e. the tardigrade behaves as a passive bystander regardless of whether the qubit B is in the ground or excited state.

It is possible to write down a mathematical model with the tardigrade as a bystander, while still producing the observed frequency shift. As a simple example, assume that the tardigrade is modelled as a two-level system with frequency ω_t coupled to the superconducting qubit according to the following total Hamiltonian:

$$H = \frac{\hbar\omega_q}{2}\sigma_z \otimes \mathbb{1} + \frac{\hbar\omega_t}{2}\mathbb{1} \otimes \sigma_z + \frac{\hbar g}{2}\sigma_z \otimes \sigma_z.$$
 (7.49)

The eigenstates of this Hamiltonian are product states being the eigenstates of local σ_z operators. The

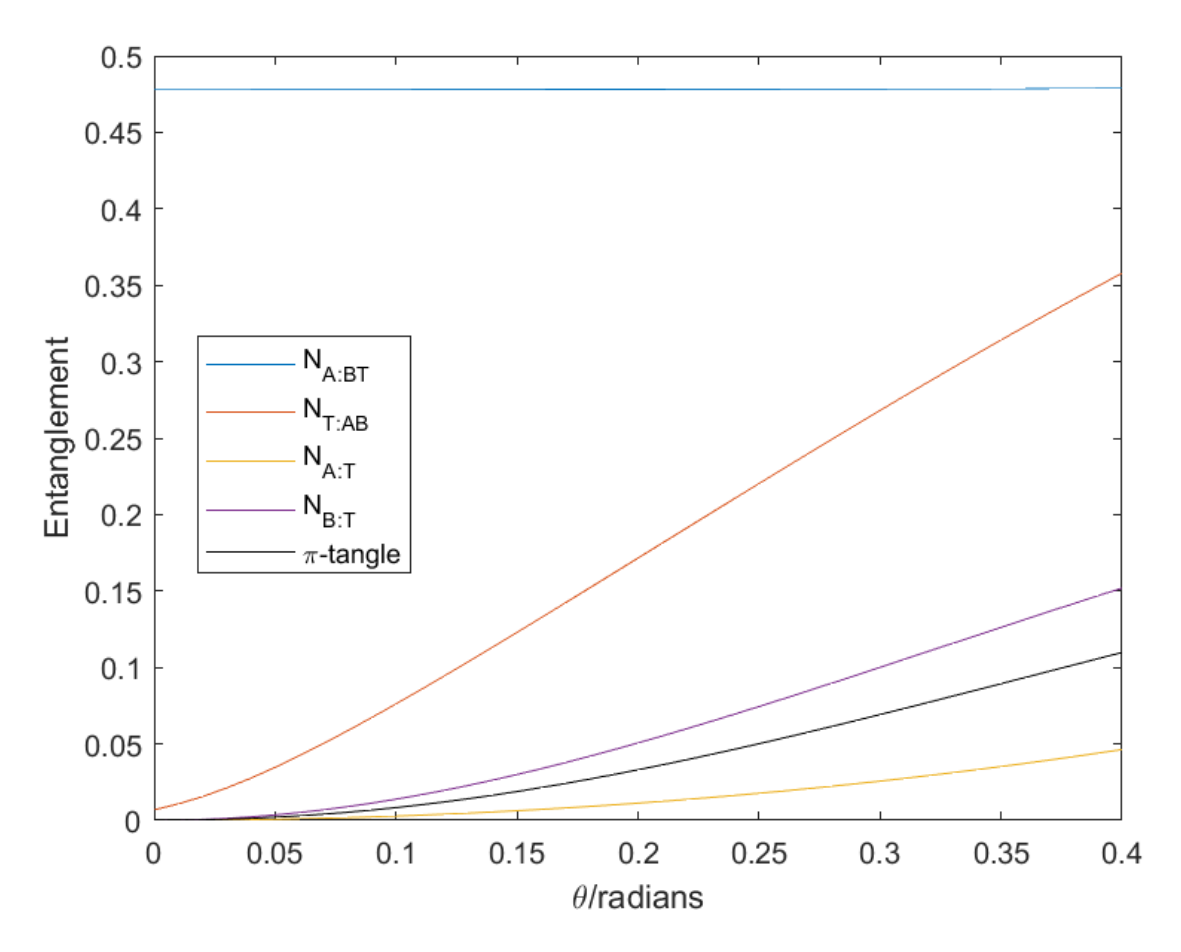


Fig. 7.8: Bipartite and tripartite entanglement in ρ_{exp} as a function of coupling strength θ .

eigenenergies are

1622

$$E_{00} = -\frac{\hbar}{2}(\omega_t + \omega_q - g), \tag{7.50}$$

$$E_{10} = -\frac{\hbar}{2}(\omega_t - \omega_q + g), \tag{7.51}$$

$$E_{01} = \frac{\hbar}{2}(\omega_t - \omega_q - g),\tag{7.52}$$

$$E_{11} = \frac{\hbar}{2}(\omega_t + \omega_q + g), \tag{7.53}$$

which for positive coupling, g > 0, results in a lower value for E_{00} and E_{11} as compared to the bare qubit and tardigrade. With $\omega_t > \omega_q$, the energy difference between ground and first excited state is $E_{10} - E_{00} = \hbar(\omega_q - g)$, i.e. lower as observed in the experiment, with the tardigrade remaining in $|d\rangle$ and thus no entanglement.

7.6.1 Electric field coupling

However, the coupling in this bystander model is different from how superconducting qubits are known to physically couple to their surrounding, which is via the electric field, $E = E_0(a^{\dagger} + a)$. When reduced to the qubit subspace, the field is proportional to σ_x Pauli matrix. Therefore, the general class of Hamiltonians must instead be of the form:

$$H = -\frac{\hbar\omega_q}{2}\sigma_z + H_T + \frac{\hbar g}{2}\sigma_x \otimes h_T, \tag{7.54}$$

where H_T and h_T are the arbitrary free and interaction tardigrade Hamiltonians.

We now show that with the constraint on electric field coupling and without entanglement, this model produces a contradictory outcome, namely an increase of the frequency readout from the qubit B-tardigrade system, opposite of our experimental findings.

Consider the ground state equation for the combined system, $H |0_d\rangle |d\rangle = E_g |0_d\rangle |d\rangle$, and setting the tardigrade energy, $H_T |d\rangle = 0$. This implies that $|d\rangle$ must be the eigenstate of the interaction part, $h_T |d\rangle = |d\rangle$. This leaves $|0_d\rangle$ and $|1_d\rangle$ as eigenstates of $-\frac{\hbar\omega_q}{2}\sigma_z + \frac{\hbar g}{2}\sigma_x$, allowing us to obtain the energy gap between ground and excited state as

$$\Delta = \sqrt{\omega_q^2 + g^2} > \omega_q. \tag{7.55}$$

Thus, without entanglement the two levels repel in contradiction to our experimental findings of a decrease in the frequency readout.

7.7 Revival

1639

1640

1641

1643

1645

It is worth noting that thus far, the function of the tardigrade is interchangeable with a grain of sand; none of its biological features were necessary in the physical description of the system and only its chemical composition affects the electric field coupling with the transmon qubit. The key distinguishing point between an inanimate speck of dust is shown here, where the tardigrade is revived back into its active state.

After single- and two-qubit experiments, the tardigrade was gently brought back to room temperatures and pressures, and placed in water. The tardigrade was then observed to successfully revive back into its metabolic state. In total, the tardigrade spent 420 hours at sub 10 mK temperatures and pressures lower than 6×10^{-6} mbar. This is to date the longest and most extreme conditions (in terms of temperature and pressures) that tardigrades have been recorded to survive.

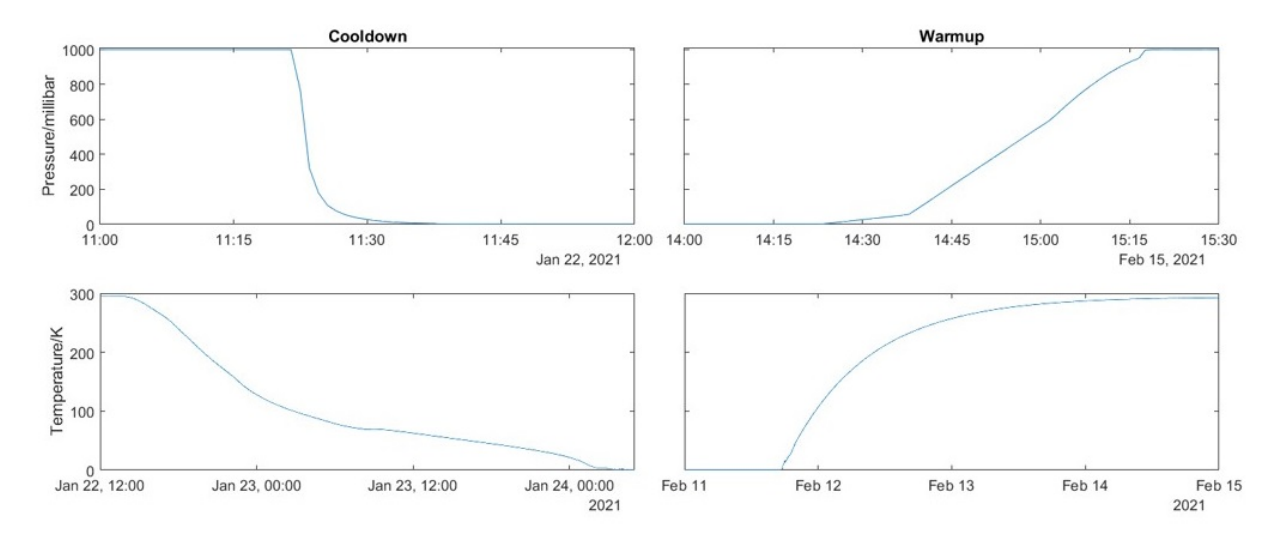


Fig. 7.9: Cooldown (left) and warmup (right) profiles in the experiment with a successful revival of the tardigrade.

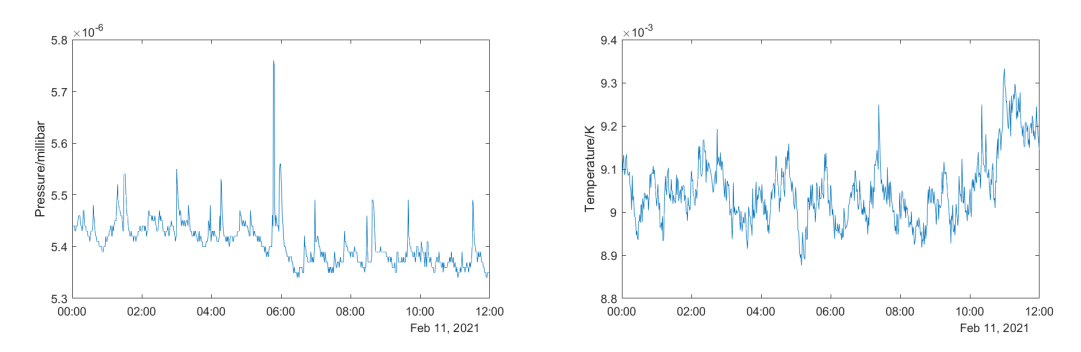


Fig. 7.10: Typical pressure (left) and temperature (right) fluctuations during the experiment (after stabilisation from the cooldown and before the warmup.

There were also two earlier experiment runs on different tardigrades that did not yield a successful revival. On the third trial, a gentler pressure gradient was implemented during the warmup by using a slower venting process that took about an hour to return to room pressures, as compared to 15 minutes in the earlier two runs. The temperature and pressure curves for the cooldown and warmup that yielded a successful revival of the tardigrade are shown in Fig. 7.9. The chamber housing the tardigrade required about 2 days to be cooled down to temperatures lower than 10 mK, while the pressure drop to around 6×10^{-3} took about half an hour. The typical fluctuations of the operating temperature and pressures are shown in Fig. 7.10. It should be mentioned that these pressure readings are a generous upper bound of the pressure due to the limitations of the sensors, which are not directly positioned in the chamber housing the tardigrades. The actual pressure at the tun location is estimated to be as low as 2.55×10^{-13} mbar from previous experiments using Rubidium atomic clouds [187]. For the warmup, the temperature rose gradually over 3 days to room temperature, while the slow venting brought pressures back to room levels over a time frame of an hour.

Other than being a significant milestone for tardigrade resilience, the extreme conditions also present a case for cryptobiosis being truly ametabolic. At such low temperatures, all the tardigrade constituent molecules would be cooled to their ground states, lacking the energetics for any chemical reactions, demonstrating a complete suspension of all metabolic activity. Due to the lack of metabolic activity, an inanimate object of similar composition would behave similarly to the tardigrade. However, emphasis should be made that the tardigrade ultimately retained its biological functionality post experiment, making it the closest realisation of the marrying of quantum and biological systems.

56 7.8 Summary

In this chapter, we described an experiment involving an interaction between a tardigrade in a tun state and two superconducting transmon qubits. The tardigrade system is modelled as a collection of harmonic oscillators, while the qubits are the two-level systems. The coupling between qubit B, on which the tardigrade is located, is taken to be the dipole-dipole interaction. Using this model, the frequency shift observed of the tardigrade-qubit system (compared to just the bare qubit B) can be explained in the dressed state picture, where the new eigenstates of this composite system are different. A maximally entangled Bell state between the composite tardigrade-qubit B system and another qubit A is then produced. From our model, we can show that for any finite strength of interactions, the system has genuine tripartite entanglement.

After 420 hours in the fridge, the tardigrade was brought back to room temperature and pressure, and then successfully revived in water. This is a new record for both the most extreme and longest exposure to low temperatures and pressures to date. At the same time, it also demonstrates that the cryptobiosis is truly ametabolic, as the sub 10 mK temperatures would exclude all chemical processes from occurring over the full duration.

${ m `` Chapter 8}$

1682

1684

1685

1686

1687

1688

1689

1690

1691

1692

1693

1695

1696

1697

1698

1699

1700

1701

1702

1703

1704

1706

1708

1709

1710

1712

Conclusions and Outlook

In this thesis, we have presented a series of experiments investigating quantum effects in biological systems. We began with studies searching for clear indications of PEMF effects in C. elegans and C2C12 mouse myoblast cells. These experiments did not demonstrate a measurable impact on mitochondrial activity, cell proliferation or calcium entry. This was followed by a behavioural experiment on American cockroaches which demonstrated magnetic sensitivity in the animal. Using the current understandings of the underlying physical models of magnetoreception, we determined that the magnetic sense in cockroaches is most likely based on the radical pair mechanism. Finally, we described an experiment capturing entanglement in a quantum-biological hybrid system. This involved two qubits, with only one qubit directly coupled to a tardigrade. Generating and subsequently measuring the Bell-state of this qubit-qubit-tardigrade system revealed genuine tripartite entanglement. Importantly, the tardigrade emerged still living after the entire experiment. In this final chapter, we summarise briefly the content of the thesis, chapter by chapter, and end with some outlook on future research directions.

8.1 I: Magnetic Field Effects in Cells

In the first part of the thesis, we documented our search for clear effects of Pulsed Electro-Magnetic Fields (PEMFs) on model organisms and cells. We started off with observing the mitochondrial activity in the nematode Caenorhabditis elegans after a ten minute exposure to PEMFs. The readouts did not show a clear consistent trend, showing the quality of C. elegans samples varied across experimental runs. This prompted us to look at a simpler system, at the cellular level. The effects of PEMFS on cell proliferation of C2C12 mouse myoblasts were investigated using a manual cell counting method as well as fluorescence spectroscopy. The two methods showed a higher number of cells / fluorescence from PEMF exposure in coil C as compared to coil A, even though the fields produced in both devices were the same. A follow-up investigation on the different lighting conditions did not show any significant effect. At the same time, fluorescence indicated a 20 % drop in cell number across all devices as compared to manual counting after exposures to PEMFs. This could be explained by an altered permeability of the cell membrane such that either less dye or more background suppressors reached the cell interior. Lastly, the rate of calcium entry into vesicles derived from C2C12 mouse myoblast and myotubes was measured. This was done by preloading the parent cells with a calcium binding dye and then generating the vesicles by agitating them with Cytochalasin B and mechanical sheer forces, before immersing the vesicles in the calcium rich medium flourobrite. Scanning electron microscopy images revealed that the vesicles generated by this method had a variation of sizes, indicating a mixture of different vesicle types. The fluorescence readout from exposures to PEMFs and sinusoidal fields of frequencies 3.3 kHz and 6.6 kHz revealed no change in the rate of calcium entry. Ultimately, these experiments were unable to show any measurable impact of PEMFs. However,

given how much of the experimental space still remains unexplored, the detailed methodology outlined in this chapter can help as a roadmap for future studies.

8.2 II: Magnetoreception

1717

1719

1720

1721

1723

1725

1727

1729

1731

1732

1733

1735

1737

1739

1740

1741

1742

1743

1744

1745

1746

1747

1749

1750

1751

1752

1753

1754

1755

1756

1757

In the second part of the thesis, we discussed the phenomenon of magnetoreception, which is the ability found in certain animals to detect and utilise the Earth's magnetic field. We introduced simplified models on the physical processes involved in animal magnetoreception. These are the ferromagnetic-based model and a radical pair model. In the former, iron rich deposits embedded in the animal act as tiny compasses that passively align to an external magnetic field. Depending on the complexity of the animal, taking magnetotactic bacteria as an example, this is sufficient to passively steer the organism in the processes known as magnetotaxis. Otherwise, an additional transduction pathway is required for the interpretation of the signal. For the radical pair model, suitable protein complexes can have covalent bonds cleaved, resulting in a coherent pair of intermediary radicals, each with an unpaired electron. Initially, the radical pair is formed in a singlet state but can evolve to a triplet state by interacting with an applied magnetic field. These radicals can then proceed with a forward reaction, or undergo a recombination, limited only to pairs in the singlet state, back to the original protein. This confers a magnetic field dependency on the product yield, which can in turn be used as a basis for magnetoreception. Equipped with the relevant models, we proceed in examining the magnetoreception characteristics in living specimens of *Periplaneta americana*, American cockroaches.

We described our experiment performed on American cockroaches to investigate their magnetic sensitivity and discussed the implications of our measured results. American cockroaches displayed an increase in activity time, a quantity capturing the total time the cockroach spends in motion over its 12 hour observation period, in the presence of a Rotating Earth Strength Field (RESF). However, this increase in activity time was diminished when the rotated field was raised to 5 G, about 12 times larger than the Earth's field. To explain the observations, the two models for magnetoreception (ferromagnetic and radical pair models) were expanded upon with realistic parameters relevant to the American cockroach. By simulating the alignment of both spherical and rod-shaped magnetite particles embedded in the highly viscous internal environment of the cockroach, it was shown that no appreciable alignment could be attained in the weak geomagnetic field. Additionally, the magnetite model is also unable to explain the diminishing effect in a larger field without introducing a frictional term that scales with magnetic field strength. On the other hand, the radical pair model, being a chemical reaction, operates at a timescale fast enough to respond to the RESF. Additionally, the lower singlet yield in a larger aligning magnetic field can account for the diminishing activity time observed in the larger 5 G test field. The incompatibility of cockroach magnetite and plausibility of a radical pair compass points to the importance of cockroach Cryptochrome-2 in magnetoreception, which is in agreement with the experiments by Vacha [23, 119–121].

8.3 III: Entanglement in Living Systems

In the third part of the thesis, we introduce some theoretical background on quantum harmonic oscillators and their generalisations before describing an experiment on entanglement in a qubit-qubit-tardigrade hybrid system. We presented the properties of the quantum harmonic oscillator and discussed several models of interactions between qubit and oscillators: the Rabi, Jaynes-Cummings, Dicke and Tavis-Cummings models. Notably, the Rabi and Jaynes-Cummings refer to a single oscillator coupled to a single two-level system, with the Rotating-Wave Approximation (RWA) taken in the latter that greatly simplifies the problem. Comparisons between the Dicke and Jaynes-Cummings solutions show that the Jaynes-Cummings model is a good approximation in the weak-coupling and near-resonant regime. The Dicke and Tavis-Cummings models are generalisations for multiple N oscillators. While general solutions for the Dicke model are not yet known, except for small N, the Tavis-Cummings solution is shown to be equivalent to the Jaynes-Cummings

except with a \sqrt{N} scaling of the coupling strength. In short, the Jaynes-Cummings model will sufficiently describe most atom-cavity experiments.

Finally, we move past boundaries between quantum and biological experiments by generating entanglement in a system consisting of a living animal (prior and post experiment; during the experiment depends on one's definition of life) and two superconducting transmon qubits. The animal utilised is the tardigrade Ramazzottius varieornatus Bertolani and Kinchin, 1993, that can enter a resilient "tun" state, allowing it to withstand harsh conditions, like low temperatures and pressures, normally hostile to most forms of life. These are exactly the optimal conditions for superconducting qubit experiments. We utilised transmon qubits, which are essentially two superconducting plates shunted by a large capacitor and connected through some non-linear inductor such as a Josephson junction. By assuming the tardigrade's degree of freedom as a collection of multiple harmonic oscillators, the joint system of a tardigrade placed in close proximity to a transmon qubit can be described in a similar fashion to the Tavis-Cummings model. This interaction is observed as a frequency shift of the qubit-tardigrade system, as compared to the bare qubit frequency. In the next step of the experiment, a Bell state is generated between this qubit-tardigrade system and a secondary qubit. The entanglement of this qubit-qubit-tardigrade system is inferred from quantum state tomography and shows the presence of genuine tripartite effects. Finally, the tardigrade is brought back to room temperature and pressure, and observed to return to an active form. To-date, these are the most extreme conditions a tardigrade has been recorded to survive. The experiment is possibly the closest realisation of observing quantum effect on a living system, and also demonstrates that the tardigrade can be a model organism in studying the interface between the quantum and biological scales.

1779 8.4 Outlook

Overall, understanding and identifying the role of quantum mechanics in biological processes will give us deeper insight into the question of quantum-to-classical transition. Many of the remarkable properties of quantum phenomena, like superposition or entanglement, are seemingly absent in day to day biological processes. This is perplexing given that our current understanding suggests that all physical systems comprise of atoms and molecules that fundamentally follow the rules of quantum mechanics. One of the many unanswered questions in quantum biology that is perhaps closest to being properly understood is the role of the radical pair mechanism. Many experiments from different groups have independently verified phenomena that fits well with a radical pair magnetoreception model, for example, birds become disoriented in the presence of oscillating magnetic fields [21,27,115,116], while cockroaches lose their magnetic sensitivity when Cryptochrom-2 was removed. It should be pointed out that the calculations in Chapter 4, for the radical pair model, utilised the hyperfine tensor values and transition rates of the closely related Cryptochrome-1 in A. thaliana and Photolyase in E. coli. It is thus interesting to repeat the calculations with relevant parameters for Cryptochrome-2 that may reveal more characteristics of the radical pair compass.

Many different research groups are currently engaged in identifying the efficacy and extent of magnetic fields as a means for treatment of medical issues. Unfortunately, these studies do not directly complement each other well due to most groups using their own variations of magnetic fields each with their own varying frequencies (or even static), intensity values and pulse shapes. This is compounded by the sometimes proprietary nature of the studies that conceal the type of devices utilised. As such, while many reviews point out the positive outcomes with minimal side effects [51, 188, 189], the underlying physical mechanisms for magnetic fields affecting such a wide range of biological processes still remains largely unknown. Collaborative works between the biomedical and biophysics communities on larger scales will be required to improve our understanding into the role of magnetic fields as a means of medical treatments.

Our experiment on entanglement in the qubit-qubit-tardigrade system shows that the bridge between quantum physics an complex biology can already be crossed. With a viable organism that can survive conditions commonplace to the modern quantum experiments, one can expect many more such hybrid systems to be investigated. As an example, the experiment presented could be further refined by narrowing down the

molecules on the tardigrade that are coupling with the qubit. Tardigrades could additionally be cultivated 1806 with higher metallic content to improve coupling strengths. Ultimately, the observation of entanglement of 1807 a biological system with qubits serves as an important proof of concept for further investigations into the 1808 scale that the laws of quantum mechanics extend to.

As an ending note, there is currently an increased interest in the field of quantum research, specifically in 1810 quantum computing, presenting an opportune moment for quantum biology. Directly, quantum computers 1811 will allow for complex quantum simulations of large protein complexes common in biology to be performed 1812 more efficiently. Indirectly, the influx of talent can also draw more eyes to the many unanswered questions 1813 into the role that quantum mechanics has in the field of biology. As such, one should remain optimistic and excited on where quantum biology will be heading towards in the near future. 1815

Appendix A

Individual cockroach activity time

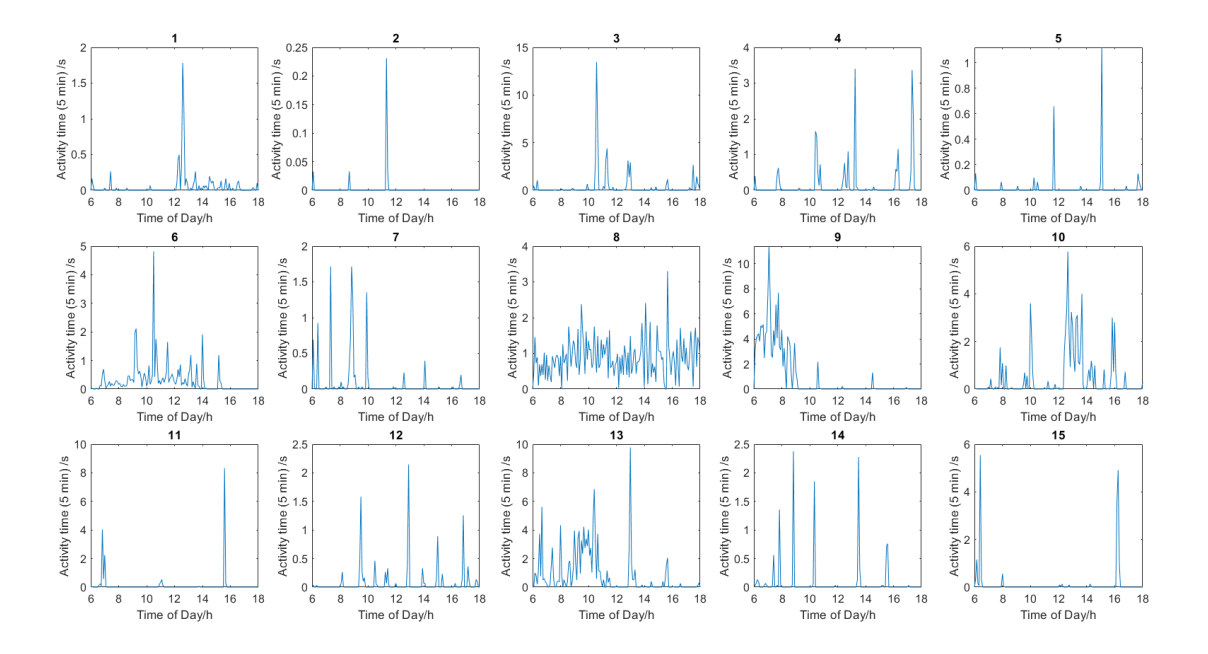


Fig. A.1: Individual (1-15) cockroach activity times (over 5 min intervals) under the control magnetic field.

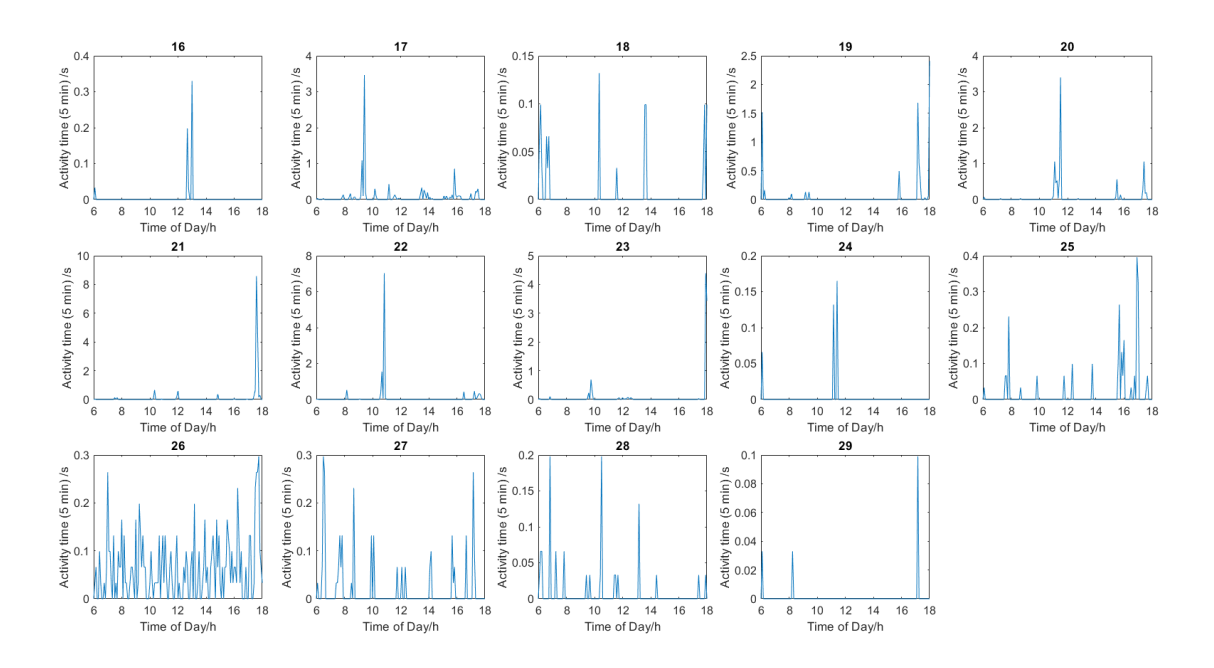


Fig. A.2: Individual (16-29) cockroach activity times (over 5 min intervals) under the control magnetic field.

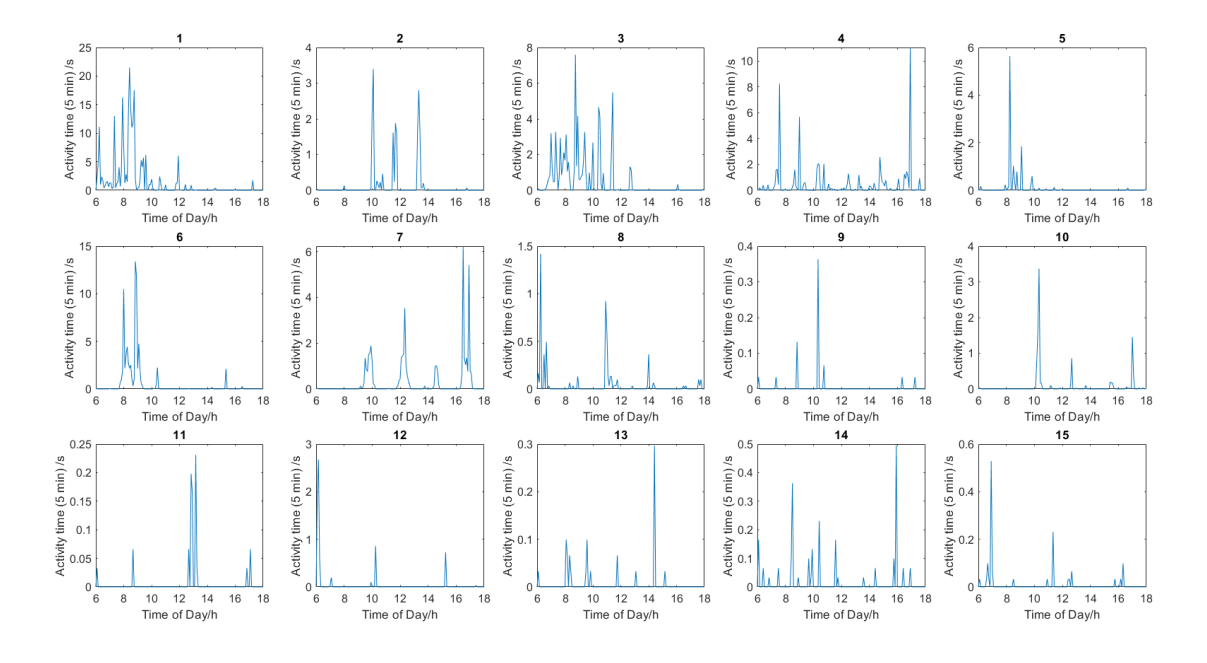


Fig. A.3: Individual (1-15) cockroach activity times (over 5 min intervals) under the RESF magnetic field.

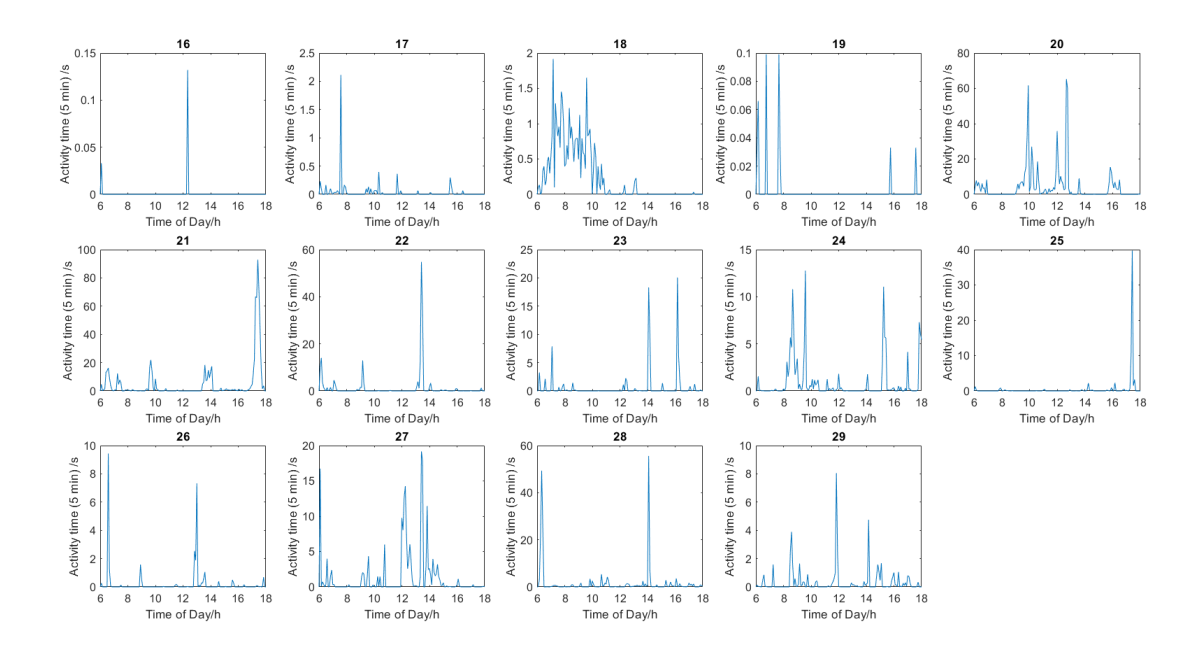


Fig. A.4: Individual (16-29) cockroach activity times (over 5 min intervals) under the control magnetic field.

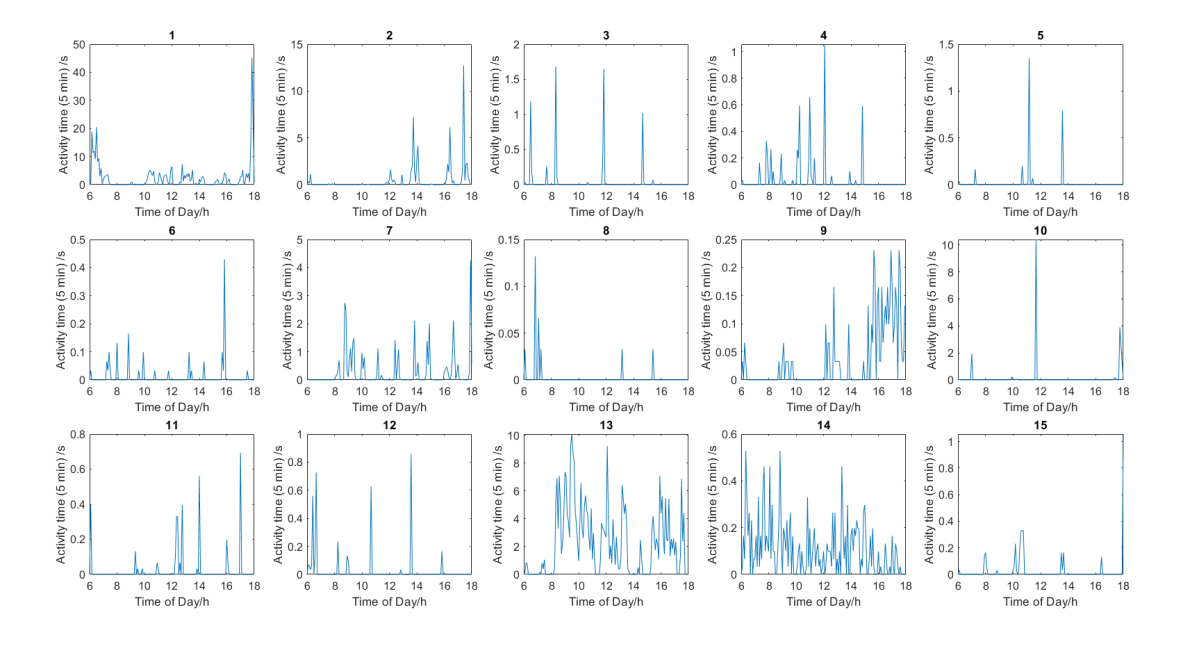


Fig. A.5: Individual (1-15) cockroach activity times (over 5 min intervals) under the 5 G test magnetic field.

References

- [1] Weiss, N. Dynamos in planets, stars and galaxies. Astronomy and Geophysics 43, 3.09–3.15 (2002).
- [2] Kadir, L. A., Stacey, M. & Barrett-Jolley, R. Emerging roles of the membrane potential: Action beyond the action potential. *Frontiers in Physiology* **9:1661** (2018).
- [3] Zablotskii, V., Polyakova, T., Lunov, O. & Dejneka, A. How a high-gradient magnetic field could affect cell life. *Scientific Reports* **6**, 37407 (2016).
- [4] Kalmijn, A. J. Electric and magnetic field detection in elasmobranch fishes. *Science* **218**, 916–918 (1982).
- [5] Schulten, K., Swenberg, C. E. & Weller, A. A biomagnetic sensory mechanism based on magnetic field modulated coherent electron spin motion. *Zeitschrift für Physikalische Chemie* 111, 1–5 (1978).
- [6] Engel, G. S. *et al.* Evidence for wavelike energy transfer through quantum coherence in photosynthetic systems. *Nature* **446**, 782–786 (2007).
- [7] Lee, H., Cheng, Y.-C. & Fleming, G. R. Coherence dynamics in photosynthesis: Protein protection of excitonic coherence. *Science* **316**, 1462–1465 (2007).
- [8] Panitchayangkoon, G. et al. Long-lived quantum coherence in photosynthetic complexes at physiological temperature. Proceedings of the National Academy of Sciences 107, 12766–12770 (2010).
- [9] Blakemore, R. Magnetotactic bacteria. Science 190, 377–379 (1975).
- [10] Pan, W. et al. Evidence for the presence of biogenic magnetic particles in the nocturnal migratory brown planthopper, Nilaparvata lugens. Scientific Reports 6 (2016).
- [11] Kirschvink, J. L. The horizontal magnetic dance of the honeybee is compatible with a single-domain ferromagnetic magnetoreceptor. *Biosystems* **14**, 193–203 (1981).
- [12] Kirschvink, J. L. & Kirschvink, A. K. Is geomagnetic sensitivity real? replication of the walker-bitterman magnetic conditioning experiment in honey bees. *American Zoologist* **31**, 169–186 (1991).
- [13] Kirschvink, J., Padmanabha, S., Boyce, C. & Oglesby, J. Measurement of the threshold sensitivity of honeybees to weak, extremely low-frequency magnetic fields. *Journal of Experimental Biology* 200, 1363–1368 (1997).
- [14] Walker, M. M., Kirschvink, J. L., Chang, S.-B. R. & Dizon, A. E. A candidate magnetic sense organ in the yellowfin tuna, *Thunnus albacares. Science* **224**, 751–753 (1984).
- [15] Mann, S., Sparks, N. H., Walker, M. M. & Kirschvink, J. L. Ultrastructure, morphology and organization of biogenic magnetite from sockeye salmon, oncorhynchus nerka: implications for magnetoreception. *Journal of Experimental Biology* 140, 35–49 (1988).
- [16] Holland, R. A., Kirschvink, J. L., Doak, T. G. & Wikelski, M. Bats use magnetite to detect the earth's magnetic field. *PLoS ONE* **3**, e1676 (2008).

- [17] Tian, L., Lin, W., Zhang, S. & Pan, Y. Bat head contains soft magnetic particles: Evidence from magnetism. *Bioelectromagnetics* **31**, 499–503 (2010).
- [18] Tian, L. et al. Testing for the presence of magnetite in the upper-beak skin of homing pigeons. BioMetals 20, 197–203 (2006).
- [19] Wiltschko, R. & Wiltschko, W. Magnetoreception. BioEssays 28, 157–168 (2006).
- [20] Winklhofer, M., Dylda, E., Thalau, P., Wiltschko, W. & Wiltschko, R. Avian magnetic compass can be tuned to anomalously low magnetic intensities. *Proceedings of the Royal Society B: Biological Sciences* **280**, 20130853 (2013).
- [21] Thalau, P., Ritz, T., Stapput, K., Wiltschko, R. & Wiltschko, W. Magnetic compass orientation of migratory birds in the presence of a 1.315 MHz oscillating field. *Naturwissenschaften* **92**, 86–90 (2004).
- [22] Pacini, S. et al. Effect of 0.2 t static magnetic field on human neurons: remodeling and inhibition of signal transduction without genome instability. *Neuroscience Letters* **267**, 185–188 (1999).
- [23] Vacha, M., Puzova, T. & Kvicalova, M. Radio frequency magnetic fields disrupt magnetoreception in american cockroach. *Journal of Experimental Biology* 212, 3473–3477 (2009).
- [24] Wiltschko, R., Nießner, C. & Wiltschko, W. The magnetic compass of birds: The role of cryptochrome. Frontiers in Physiology 12 (2021).
- [25] Walcott, C. & Green, R. P. Orientation of homing pigeons altered by a change in the direction of an applied magnetic field. *Science* **184**, 180–182 (1974).
- [26] Wiltschko, W. & Wiltschko, R. Magnetoreception in birds: two receptors for two different tasks. Journal of Ornithology 148, 61–76 (2007).
- [27] Wiltschko, R. & Wiltschko, W. Sensing magnetic directions in birds: Radical pair processes involving cryptochrome. *Biosensors* 4, 221–242 (2014).
- [28] Wiltschko, W., Stapput, K., Thalau, P. & Wiltschko, R. Avian magnetic compass: fast adjustment to intensities outside the normal functional window. *Naturwissenschaften* **93**, 300–304 (2006).
- [29] Wiltschko, R., Munro, U., Ford, H., Stapput, K. & Wiltschko, W. Light-dependent magnetoreception: orientation behaviour of migratory birds under dim red light. *Journal of Experimental Biology* 211, 3344–3350 (2008).
- [30] Muheim, R., Bäckman, J. & Åkesson, S. Magnetic compass orientation in European robins is dependent on both wavelength and intensity of light. *Journal of Experimental Biology* 205, 3845–3856 (2002).
- [31] Diego-Rasilla, F. J., Luengo, R. M. & Phillips, J. B. Light-dependent magnetic compass in iberian green frog tadpoles. *Naturwissenschaften* 97, 1077–1088 (2010).
- [32] Parate, D. et al. Enhancement of mesenchymal stem cell chondrogenesis with short-term low intensity pulsed electromagnetic fields. Scientific Reports 7 (2017).
- [33] Raylman, R. R., Clavo, A. C. & Wahl, R. L. Exposure to strong static magnetic field slows the growth of human cancer cells in vitro. *Bioelectromagnetics* 17, 358–363 (1996).
- [34] Miyakoshi, J. Effects of static magnetic fields at the cellular level. Progress in Biophysics and Molecular Biology 87, 213–223 (2005).
- [35] Dini, L. & Abbro, L. Bioeffects of moderate-intensity static magnetic fields on cell cultures. *Micron* **36**, 195–217 (2005).
- [36] Hu, H. et al. Promising application of pulsed electromagnetic fields (PEMFs) in musculoskeletal disorders. Biomedicine & Pharmacotherapy 131, 110767 (2020).

- [37] Pooam, M., Jourdan, N., Esawi, M. E., Sherrard, R. M. & Ahmad, M. HEK293 cell response to static magnetic fields via the radical pair mechanism may explain therapeutic effects of pulsed electromagnetic fields. *PLOS ONE* **15**, e0243038 (2020).
- [38] Yap, J. L. Y. et al. Ambient and supplemental magnetic fields promote myogenesis via a TRPC1mitochondrial axis: evidence of a magnetic mitohormetic mechanism. The FASEB Journal 33, 12853– 12872 (2019).
- [39] Yin, Y. et al. The effects of a pulsed electromagnetic field on the proliferation and osteogenic differentiation of human adipose-derived stem cells. *Medical Science Monitor* 24, 3274–3282 (2018).
- [40] Jazayeri, M. et al. Effects of electromagnetic stimulation on gene expression of mesenchymal stem cells and repair of bone lesions. Cell J (Yakhteh) 19 (2017).
- [41] Mayer-Wagner, S. et al. Effects of low frequency electromagnetic fields on the chondrogenic differentiation of human mesenchymal stem cells. *Bioelectromagnetics* **32**, 283–290 (2010).
- [42] Saino, E. et al. Effects of electromagnetic stimulation on osteogenic differentiation of human mesenchymal stromal cells seeded onto gelatin cryogel. *International Journal of Immunopathology and Pharmacology* 24, 1–6 (2011).
- [43] Potočar, U. et al. Adipose-derived stem cells respond to increased osmolarities. PLOS ONE 11, e0163870 (2016).
- [44] Parate, D. et al. Pulsed electromagnetic fields potentiate the paracrine function of mesenchymal stem cells for cartilage regeneration. Stem Cell Research & Therapy 11 (2020).
- [45] Bassett, C. A. L., Pawluk, R. J. & Pilla, A. A. Acceleration of fracture repair by electromagnetic fields. A surgically noninvasive method. Annals of the New York Academy of Sciences 238, 242–262 (1974).
- [46] Bassett, C., Pilla, A. & Pawluk, R. A non-operative salvage of surgically-resistant pseudarthroses and non-unions by pulsing electromagnetic fields. a preliminary report. *Clinical orthopaedics and related* research 128—143 (1977).
- [47] Andrew, C., Bassett, L., Pawluk, R. J. & Pilla, A. A. Augmentation of bone repair by inductively coupled electromagnetic fields. *Science* **184**, 575–577 (1974).
- [48] Cheing, G. L.-Y., Li, X., Huang, L., Kwan, R. L.-C. & Cheung, K.-K. Pulsed electromagnetic fields (PEMF) promote early wound healing and myofibroblast proliferation in diabetic rats. *Bioelectromagnetics* 35, 161–169 (2014).
- [49] Choi, H. M. C., Cheing, A. K. K., Ng, G. Y. F. & Cheing, G. L. Y. Effects of pulsed electromagnetic field (PEMF) on the tensile biomechanical properties of diabetic wounds at different phases of healing. *PLOS ONE* 13, e0191074 (2018).
- [50] Thomas, A. W. et al. A randomized, double-blind, placebo-controlled clinical trial using a low-frequency magnetic field in the treatment of musculoskeletal chronic pain. Pain Research and Management 12, 249–258 (2007).
- [51] Andrade, R. et al. Pulsed electromagnetic field therapy effectiveness in low back pain: A systematic review of randomized controlled trials. Porto Biomedical Journal 1, 156–163 (2016).
- [52] Working Group on the Evaluation of the Carcinogenic Risk of Chemicals to Humans, I. Non-Ionizing Radiation, Part 1: Static and Extremely Low-Frequency (ELF) Electric and Magnetic Fields. IARC Monographs on the Evaluation of Carcinogenic Risk to Humans, Vol. 80, vol. 80 (2002).
- [53] Tai, Y. K. et al. Magnetic fields modulate metabolism and gut microbiome in correlation with Pgc-1α expression: Follow-up to an in vitro magnetic mitohormetic study. The FASEB Journal 34, 11143–11167 (2020).

- [54] Markov, M. S. Expanding use of pulsed electromagnetic field therapies. *Electromagnetic Biology and Medicine* **26**, 257–274 (2007).
- [55] Crocetti, S. et al. Low intensity and frequency pulsed electromagnetic fields selectively impair breast cancer cell viability. PLoS ONE 8, e72944 (2013).
- [56] Lai, C.-H., Chou, C.-Y., Ch'ang, L.-Y., Liu, C.-S. & chang Lin, W. Identification of novel human genes evolutionarily conserved in caenorhabditis elegans by comparative proteomics. Genome Research 10, 703–713 (2000).
- [57] Brenner, S. The genetics of caenorhabditis elegans. Genetics 77, 71–94 (1974).
- [58] Consortium, T. C. S. Genome sequence of the nematode c. elegans: A platform for investigating biology. *Science* **282**, 2012–2018 (1998).
- [59] White, J. G., Southgate, E., Thomson, J. N. & Brenner, S. The structure of the nervous system of the nematode caenorhabditis elegans. *Philosophical Transactions of the Royal Society B: Biological Sciences* **314**, 1–340 (1986).
- [60] Kaletta, T. & Hengartner, M. O. Finding function in novel targets: C. elegans as a model organism. Nature Reviews Drug Discovery 5, 387–399 (2006).
- [61] Cranfield, C. G. et al. Biogenic magnetite in the nematode caenorhabditis elegans. Proceedings of the Royal Society of London. Series B: Biological Sciences 271 (2004).
- [62] Vidal-Gadea, A. et al. Magnetosensitive neurons mediate geomagnetic orientation in caenorhabditis elegans. eLife 4 (2015).
- [63] Landler, L. et al. Comment on "magnetosensitive neurons mediate geomagnetic orientation in caenorhabditis elegans". eLife 7 (2018).
- [64] Turrens, J. F. Mitochondrial formation of reactive oxygen species. The Journal of Physiology 552, 335–344 (2003).
- [65] Wang, H. & Zhang, X. Magnetic fields and reactive oxygen species. International Journal of Molecular Sciences 18, 2175 (2017).
- [66] Staniek, K., Gille, L., Kozlov, A. V. & Nohl, H. Mitochondrial superoxide radical formation is controlled by electron bifurcation to the high and low potential pathways. Free Radical Research 36, 381–387 (2002).
- [67] Bagkos, G., Koufopoulos, K. & Piperi, C. Mitochondrial emitted electromagnetic signals mediate retrograde signaling. Medical Hypotheses 85, 810–818 (2015).
- [68] Richter, C. et al. Oxidants in mitochondria: from physiology to diseases. Biochimica et Biophysica Acta (BBA) Molecular Basis of Disease 1271, 67–74 (1995).
- [69] Pho, K. B. & MacNeil, L. T. Biology is the root of variability: cautionary tales in *Caenorhabditis elegans* biology. *Biochemical Society Transactions* 47, 887–896 (2019).
- [70] Yang, N., Ray, S. & Krafts, K. Cell proliferation. In Encyclopedia of Toxicology, 761–765 (Elsevier, 2014).
- [71] Li, Y., Barbash, O. & Diehl, J. A. Regulation of the cell cycle. In The Molecular Basis of Cancer, 165–178.e2 (Elsevier, 2015).
- [72] Boer, L. D. et al. Cyclin a/cdk2 coordinates centrosomal and nuclear mitotic events. Oncogene 27, 4261–4268 (2008).
- [73] Yaffe, D. & Saxel, O. Serial passaging and differentiation of myogenic cells isolated from dystrophic mouse muscle. *Nature* 270, 725–727 (1977).

- [74] Mierzejewski, B. et al. Human and mouse skeletal muscle stem and progenitor cells in health and disease. Seminars in Cell & Developmental Biology 104, 93–104 (2020).
- [75] Kislinger, T. et al. Proteome dynamics during c2c12 myoblast differentiation. Molecular & Cellular Proteomics 4, 887–901 (2005).
- [76] Sher, R. B., Cox, G. A. & Ackert-Bicknell, C. Development and disease of mouse muscular and skeletal systems. In *The Laboratory Mouse*, 209–239 (Elsevier, 2012).
- [77] Xu, S.-Z. & Beech, D. J. TrpC1 is a membrane-spanning subunit of store-operated Ca²⁺ channels in native vascular smooth muscle cells. *Circulation Research* 88, 84–87 (2001).
- [78] Golovina, V. A. Cell proliferation is associated with enhanced capacitative Ca²⁺ entry in human arterial myocytes. *American Journal of Physiology-Cell Physiology* **277**, C343–C349 (1999).
- [79] Camussi, G., Deregibus, M. C., Bruno, S., Cantaluppi, V. & Biancone, L. Exosomes/microvesicles as a mechanism of cell-to-cell communication. *Kidney International* **78**, 838–848 (2010).
- [80] Fuhrmann, G., Herrmann, I. K. & Stevens, M. M. Cell-derived vesicles for drug therapy and diagnostics: Opportunities and challenges. *Nano Today* **10**, 397–409 (2015).
- [81] Kurth, F. et al. Cell-derived vesicles as TRPC1 channel delivery systems for the recovery of cellular respiratory and proliferative capacities. Advanced Biosystems 4, 2000146 (2020).
- [82] Pick, H. et al. Investigating cellular signaling reactions in single attoliter vesicles. Journal of the American Chemical Society 127, 2908–2912 (2005).
- [83] Chuo, S. T.-Y., Chien, J. C.-Y. & Lai, C. P.-K. Imaging extracellular vesicles: current and emerging methods. *Journal of Biomedical Science* 25 (2018).
- [84] Hore, P. J. & Mouritsen, H. The radical-pair mechanism of magnetoreception. Annual Review of Biophysics 45, 299–344 (2016).
- [85] Kirschvink, J. L. & Gould, J. L. Biogenic magnetite as a basis for magnetic field detection in animals. Biosystems 13, 181–201 (1981).
- [86] Johnsen, S. & Lohmann, K. J. The physics and neurobiology of magnetoreception. Nature Reviews Neuroscience 6, 703-712 (2005).
- [87] Lohmann, K. et al. Magnetic orientation of spiny lobsters in the ocean: Experiments with undersea coil systems. The Journal of experimental biology 198, 2041–8 (1995).
- [88] Marhold, S., Wiltschko, W. & Burda, H. A magnetic polarity compass for direction finding in a subterranean mammal. *Naturwissenschaften* 84, 421–423 (1997).
- [89] Light, P., Salmon, M. & Lohmann, K. J. Geomagnetic orientation of loggerhead sea turtles: Evidence for an inclination compass. *Journal of Experimental Biology* 182, 1–10 (1993).
- [90] Ritz, T., Adem, S. & Schulten, K. A model for photoreceptor-based magnetoreception in birds. Biophysical Journal 78, 707–718 (2000).
- [91] Krichen, S., Liu, L. & Sharma, P. Biological cell as a soft magnetoelectric material: Elucidating the physical mechanisms underpinning the detection of magnetic fields by animals. *Phys. Rev. E* **96**, 042404 (2017).
- [92] Frankel, R. B., Blakemore, R. P. & Wolfe, R. S. Magnetite in freshwater magnetotactic bacteria. Science 203, 1355–1356 (1979).
- [93] Heywood, B. R., Bazylinski, D. A., Garratt-Reed, A., Mann, S. & Frankel, R. B. Controlled biosynthesis of greigite (Fe₃S₄) in magnetotactic bacteria. *Naturwissenschaften* **77**, 536–538 (1990).

- [94] Kirschvink, J. L., Kobayashi-Kirschvink, A. & Woodford, B. J. Magnetite biomineralization in the human brain. *Proceedings of the National Academy of Sciences* 89, 7683–7687 (1992).
- [95] Kittel, C. Introduction to Solid State Physics (Wiley, 2004), 8 edn.
- [96] Kirschvink, J. L. & Walker, M. M. Particle-size considerations for magnetite-based magnetoreceptors. In *Topics in Geobiology*, 243–254 (Springer US, 1985).
- [97] Brown, W. F. Domains, micromagnetics, and beyond: Reminiscences and assessments. *Journal of Applied Physics* 49, 1937–1942 (1978).
- [98] Muxworthy, A. R. & Williams, W. Critical single-domain grain sizes in elongated iron particles: implications for meteoritic and lunar magnetism. *Geophysical Journal International* **202**, 578–583 (2015).
- [99] Aharoni, A. Brown's "fundamental theorem" revisited. *Journal of Applied Physics* **90**, 4645–4650 (2001).
- [100] Witt, A., Fabian, K. & Bleil, U. Three-dimensional micromagnetic calculations for naturally shaped magnetite: Octahedra and magnetosomes. *Earth and Planetary Science Letters* **233**, 311–324 (2005).
- [101] Muxworthy, A. R. & Williams, W. Critical single-domain/multidomain grain sizes in noninteracting and interacting elongated magnetite particles: Implications for magnetosomes. *Journal of Geophysical Research: Solid Earth* 111, n/a-n/a (2006).
- [102] Muxworthy, A. R. et al. Critical single domain grain sizes in chains of interacting greigite particles: Implications for magnetosome crystals. Geochemistry, Geophysics, Geosystems 14, 5430–5441 (2013).
- [103] Closs, G. L. Mechanism explaining nuclear spin polarizations in radical combination reactions. *Journal of the American Chemical Society* **91**, 4552–4554 (1969).
- [104] Kaptein, R. & Oosterhoff, J. Chemically induced dynamic nuclear polarization II. *Chemical Physics Letters* 4, 195–197 (1969).
- [105] Buchachenko, A. L. Magnetic isotope effect: nuclear spin control of chemical reactions. *The Journal of Physical Chemistry A* **105**, 9995–10011 (2001).
- [106] Goez, M. Elucidating organic reaction mechanisms using photo-CIDNP spectroscopy. In *Hyperpolarization Methods in NMR Spectroscopy*, 1–32 (Springer Berlin Heidelberg, 2012).
- [107] Fay, T. P., Lindoy, L. P., Manolopoulos, D. E. & Hore, P. J. How quantum is radical pair magnetore-ception? *Faraday Discussions* **221**, 77–91 (2020).
- [108] Cai, J., Guerreschi, G. G. & Briegel, H. J. Quantum control and entanglement in a chemical compass. Physical Review Letters 104 (2010).
- [109] Gauger, E. M., Rieper, E., Morton, J. J. L., Benjamin, S. C. & Vedral, V. Sustained quantum coherence and entanglement in the avian compass. *Physical Review Letters* **106** (2011).
- [110] Efimova, O. & Hore, P. Evaluation of nuclear quadrupole interactions as a source of magnetic anisotropy in the radical pair model of the avian magnetic compass. *Molecular Physics* **107**, 665–671 (2009).
- [111] Maeda, K. et al. Magnetically sensitive light-induced reactions in cryptochrome are consistent with its proposed role as a magnetoreceptor. Proceedings of the National Academy of Sciences 109, 4774–4779 (2012).
- [112] Weber, S. et al. Origin of light-induced spin-correlated radical pairs in cryptochrome. The Journal of Physical Chemistry B 114, 14745–14754 (2010).
- [113] Biskup, T. et al. Unexpected electron transfer in cryptochrome identified by time-resolved EPR spectroscopy. Angewandte Chemie International Edition 50, 12647–12651 (2011).

- [114] Pakhomov, A. et al. Very weak oscillating magnetic field disrupts the magnetic compass of songbird migrants. Journal of The Royal Society Interface 14, 20170364 (2017).
- [115] Ritz, T., Thalau, P., Phillips, J. B., Wiltschko, R. & Wiltschko, W. Resonance effects indicate a radical-pair mechanism for avian magnetic compass. *Nature* 429, 177–180 (2004).
- [116] Ritz, T. et al. Magnetic compass of birds is based on a molecule with optimal directional sensitivity. Biophysical Journal 96, 3451–3457 (2009).
- [117] Kirschvink, J. Magnetite-based magnetoreception. Current Opinion in Neurobiology 11, 462–467 (2001).
- [118] Block, S. M. Biophysical principles of sensory transduction. Sensory transduction 1, 91–117 (1992).
- [119] Vacha, M. Laboratory behavioural assay of insect magnetoreception: magnetosensitivity of periplaneta americana. *Journal of Experimental Biology* **209**, 3882–3886 (2006).
- [120] Vacha, M., Kvicalova, M. & Puzova, T. American cockroaches prefer four cardinal geomagnetic positions at rest. Behaviour 147, 425–440 (2010).
- [121] Bazalova, O. et al. Cryptochrome 2 mediates directional magnetoreception in cockroaches. Proceedings of the National Academy of Sciences 113, 1660–1665 (2016).
- [122] Lee, K. S., Dumke, R. & Paterek, T. Numerical tests of magnetoreception models assisted with behavioral experiments on american cockroaches. *Scientific Reports* 11 (2021).
- [123] Bell, W. The American cockroach (Chapman and Hall, London New York, 1982).
- [124] Kong, L. J. et al. In-vivo biomagnetic characterisation of the american cockroach. Scientific Reports 8, 5140 (2018).
- [125] Li, S. et al. The genomic and functional landscapes of developmental plasticity in the american cockroach. Nature Communications 9 (2018).
- [126] Merritt, R., Purcell, C. & Stroink, G. Uniform magnetic field produced by three, four, and five square coils. *Review of Scientific Instruments* **54**, 879–882 (1983).
- [127] Wajnberg, E. et al. Electron paramagnetic resonance study of the migratory ant pachycondyla marginata abdomens. Biophysical Journal 78, 1018–1023 (2000).
- [128] Maher, B. Magnetite biomineralization in termites. *Proceedings of the Royal Society of London. Series B: Biological Sciences* **265**, 733–737 (1998).
- [129] Inward, D., Beccaloni, G. & Eggleton, P. Death of an order: a comprehensive molecular phylogenetic study confirms that termites are eusocial cockroaches. *Biology Letters* 3, 331–335 (2007).
- [130] Yorke, E. D. A possible magnetic transducer in birds. *Journal of Theoretical Biology* **77**, 101–105 (1979).
- [131] Solov'yov, I. A., Chandler, D. E. & Schulten, K. Magnetic field effects in arabidopsis thaliana cryptochrome-1. *Biophysical Journal* **92**, 2711–2726 (2007).
- [132] Nießner, C. et al. Avian ultraviolet/violet cones identified as probable magnetoreceptors. PLoS ONE 6, e20091 (2011).
- [133] Bolte, P. et al. Cryptochrome 1a localisation in light- and dark-adapted retinae of several migratory and non-migratory bird species: no signs of light-dependent activation. Ethology Ecology & Evolution 33, 248–272 (2021).
- [134] Cintolesi, F., Ritz, T., Kay, C., Timmel, C. & Hore, P. Anisotropic recombination of an immobilized photoinduced radical pair in a 50- μ t magnetic field: a model avian photomagnetoreceptor. *Chemical Physics* **294**, 385–399 (2003).

- [135] Byrdin, M. et al. Intraprotein electron transfer and proton dynamics during photoactivation of DNA photolyase from e. coli: review and new insights from an "inverse" deuterium isotope effect. Biochimica et Biophysica Acta (BBA) Bioenergetics 1655, 64–70 (2004).
- [136] Aubert, C., Vos, M. H., Mathis, P., Eker, P. M. & Brettel, K. Intraprotein radical transfer during photoactivation of DNA photolyase. *Nature* **405**, 586–590 (2000).
- [137] Mei, Q. & Dvornyk, V. Evolutionary history of the photolyase/cryptochrome superfamily in eukaryotes. PLOS ONE 10, e0135940 (2015).
- [138] Lin, C. et al. Association of flavin adenine dinucleotide with the Arabidopsis Blue Light Receptor CRY1. Science 269, 968–970 (1995).
- [139] Giovani, B., Byrdin, M., Ahmad, M. & Brettel, K. Light-induced electron transfer in a cryptochrome blue-light photoreceptor. *Nature Structural & Molecular Biology* **10**, 489–490 (2003).
- [140] Kottke, T., Batschauer, A., Ahmad, M. & Heberle, J. Blue-light-induced changes in arabidopsis cryptochrome 1 probed by FTIR difference spectroscopy. *Biochemistry* **45**, 2472–2479 (2006).
- [141] Park, H.-W., Kim, S.-T., Sancar, A. & Deisenhofer, J. Crystal structure of DNA photolyase from *Escherichia coli. Science* **268**, 1866–1872 (1995).
- [142] Kay, . W. M. et al. EPR, ENDOR, and TRIPLE resonance spectroscopy on the neutral flavin radical in Escherichia coli DNA photolyase†. Biochemistry 38, 16740–16748 (1999).
- [143] Weber, S., Möbius, K., Richter, G. & Kay, C. W. M. The electronic structure of the flavin cofactor in DNA photolyase. *Journal of the American Chemical Society* **123**, 3790–3798 (2001).
- [144] Park, H., Kim, S., Sancar, A. & Deisenhofer, J. Crystal structure of DNA photolyase from escherichia coli. *Science* **268**, 1866–1872 (1995).
- [145] Esquivel, D. M. S. et al. Do geomagnetic storms change the behaviour of the stingless bee guiruçu (Schwarziana quadripunctata)? Naturwissenschaften 94, 139–142 (2006).
- [146] Uhlenbeck, G. E. & Goudsmit, S. Spinning electrons and the structure of spectra. *Nature* **117**, 264–265 (1926).
- [147] Dirac, P. A. M. The quantum theory of the electron. Proceedings of the Royal Society of London. Series A, Containing Papers of a Mathematical and Physical Character 117, 610–624 (1928).
- [148] Dirac, P. A. M. The principles of quantum mechanics (Clarendon Press, Oxford England, 1981).
- [149] Berestetskii, V. B., Lifshitz, E. M. & Pitaevskii, L. P. Quantum Electrodynamics: Volume 4, vol. 4 (Butterworth-Heinemann, 1982).
- [150] Rabi, I. I. On the process of space quantization. Physical Review 49, 324–328 (1936).
- [151] Rabi, I. I. Space quantization in a gyrating magnetic field. Physical Review 51, 652–654 (1937).
- [152] Jaynes, E. & Cummings, F. Comparison of quantum and semiclassical radiation theories with application to the beam maser. *Proceedings of the IEEE* **51**, 89–109 (1963).
- [153] Dicke, R. H. Coherence in spontaneous radiation processes. *Physical Review* 93, 99–110 (1954).
- [154] Tavis, M. & Cummings, F. W. Exact solution for an *n*-molecule—radiation-field hamiltonian. *Physical Review* **170**, 379–384 (1968).
- [155] Scully, M. O. & Zubairy, M. S. Quantum Optics (Cambridge University Press, 1997).
- [156] Holstein, T. Studies of polaron motion. Annals of Physics 8, 325–342 (1959).
- [157] Braak, D. Integrability of the rabi model. Phys. Rev. Lett. 107, 100401 (2011).

- [158] Braak, D. Symmetries in the quantum rabi model. Symmetry 11, 1259 (2019).
- [159] Chen, Q.-H., Wang, C., He, S., Liu, T. & Wang, K.-L. Exact solvability of the quantum rabi model using bogoliubov operators. *Physical Review A* 86, 023822 (2012).
- [160] Ronveaux, A. Heun's differential equations (Oxford University Press, Oxford New York, 1995).
- [161] Fujii, K. Introduction to the rotating wave approximation (RWA): Two coherent oscillations. *Journal of Modern Physics* **08**, 2042–2058 (2017).
- [162] Amico, L., Frahm, H., Osterloh, A. & Ribeiro, G. Integrable spin-boson models descending from rational six-vertex models. *Nuclear Physics B* **787**, 283–300 (2007).
- [163] Braak, D. Analytical solution of the rabi and dicke models. In *Latin America Optics and Photonics Conference*, LTu3B.5 (Optica Publishing Group, 2014).
- [164] Braak, D. Solution of the dicke model for n= 3. Journal of Physics B: Atomic, Molecular and Optical Physics 46, 224007 (2013).
- [165] Chen, Q.-H., Zhang, Y.-Y., Liu, T. & Wang, K.-L. Numerically exact solution to the finite-size dicke model. *Physical Review A* 78 (2008).
- [166] Bastarrachea-Magnani, M. A. & Hirsch, J. G. Numerical solutions of the dicke hamiltonian (2011). 1108.0703.
- [167] Holstein, T. & Primakoff, H. Field dependence of the intrinsic domain magnetization of a ferromagnet. *Physical Review* **58**, 1098–1113 (1940).
- [168] Bullough, R. K. Photon, quantum and collective, effects from rydberg atoms in cavities. *Hyperfine Interactions* 37, 71–108 (1987).
- [169] Marletto, C., Coles, D. M., Farrow, T. & Vedral, V. Entanglement between living bacteria and quantized light witnessed by rabi splitting. *Journal of Physics Communications* 2, 101001 (2018).
- [170] Bohr, N. Light and life. Nature 131, 457–459 (1933).
- [171] Lee, K. S. et al. Entanglement between superconducting qubits and a tardigrade (2021).
- [172] Krantz, P. et al. A quantum engineer's guide to superconducting qubits. Applied Physics Reviews 6, 021318 (2019).
- [173] Møbjerg, N., Jørgensen, A., Kristensen, R. & Cardoso Neves, R. Morphology and Functional Anatomy, 57–94. Zoological Monographs (Springer, Switzerland, 2018).
- [174] Møbjerg, N. et al. Survival in extreme environments on the current knowledge of adaptations in tardigrades. Acta Physiologica 202, 409–420 (2011).
- [175] Becquerel, P. La suspension de la vie au dessous de 1/20 k absolu par demagnetization adiabatique de l'alun de fer dans le vide les plus eléve" [the suspension of life below 1/20 k absolute by adiabatic demagnetization of iron alum in the highest vacuum]. Comptes Rendus des Séances de l'Académie des Sciences (in French). 231, 261–63 (1950).
- [176] Jönsson, K. I., Rabbow, E., Schill, R. O., Harms-Ringdahl, M. & Rettberg, P. Tardigrades survive exposure to space in low earth orbit. *Current Biology* 18, R729–R731 (2008).
- [177] Møbjerg, N. & Neves, R. C. New insights into survival strategies of tardigrades. Comp Biochem Physiol A Mol Integr Physiol. 254, 110890 (2021).
- [178] Neves, R. C., Hvidepil, L. K. B., Sørensen-Hygum, T. L., Stuart, R. M. & Møbjerg, N. Thermotolerance experiments on active and desiccated states of ramazzottius varieornatus emphasize that tardigrades are sensitive to high temperatures. *Scientific Reports* 10 (2020).

- [179] Li, L., Li, C., Zhang, Z. & Alexov, E. On the dielectric "constant" of proteins: Smooth dielectric function for macromolecular modeling and its implementation in DelPhi. *Journal of Chemical Theory* and Computation 9, 2126–2136 (2013).
- [180] Economou, S. E. & Barnes, E. Analytical approach to swift nonleaky entangling gates in superconducting qubits. *Phys. Rev. B* **91**, 161405 (2015).
- [181] Premaratne, S. P., Yeh, J.-H., Wellstood, F. C. & Palmer, B. S. Implementation of a generalized controlled-not gate between fixed-frequency transmons. *Phys. Rev. A* **99**, 012317 (2019).
- [182] Filipp, S. et al. Two-qubit state tomography using a joint dispersive readout. Phys. Rev. Lett. 102, 200402 (2009).
- [183] James, D. F. V., Kwiat, P. G., Munro, W. J. & White, A. G. Measurement of qubits. *Physical Review A* 64, 052312 (2001).
- [184] Jozsa, R. Fidelity for mixed quantum states. Journal of Modern Optics 41, 2315–2323 (1994).
- [185] Zhang, H.-P. & Qiang, W.-C. π -tangle of a jaynes-cummings system and an isolated atom. *International Journal of Theoretical Physics* **57**, 1141–1147 (2017).
- [186] Vidal, G. & Werner, R. F. Computable measure of entanglement. *Physical Review A* **65**, 032314 (2002).
- [187] Landra, A. et al. Design of an experimental platform for hybridization of atomic and superconducting quantum systems. *Physical Review A* **99** (2019).
- [188] Paolucci, T. et al. Electromagnetic field therapy: A rehabilitative perspective in the management of musculoskeletal pain a systematic review. Journal of Pain Research Volume 13, 1385–1400 (2020).
- [189] Yang, X., He, H., Ye, W., Perry, T. A. & He, C. Effects of pulsed electromagnetic field therapy on pain, stiffness, physical function, and quality of life in patients with osteoarthritis: A systematic review and meta-analysis of randomized placebo-controlled trials. *Physical Therapy* **100**, 1118–1131 (2020).